A FRAMEWORK FOR DAMAGE MODELING IN MULTI-CONSTITUENT LAMINATED MATERIALS

BY

IAN TYLER TUTTLE

THESIS

Submitted in partial fulfillment of the requirements
for the degree of Master of Science in Civil Engineering
in the Graduate College of the
University of Illinois at Urbana-Champaign, 2018

Urbana, Illinois

Adviser:

Professor Arif Masud

ABSTRACT

This work contains analysis of directionally oriented material with heterogeneity across the spacial domain, between materials, and over time. Composite material containing directionally oriented material have become a necessity in the world of structural, mechanical, aerospace, and material engineering design. To account for the thermomechanical curing processes that these materials undergo when dealing with highly heterogeneous materials can cause deformation and eventually damage to the overall structure of the material. There are two methods discussed throughout the document: mixture theory to discuss the evolving curing and thermal effects on the structural behavior of a fiber reinforced laminate structure and a Discontinuous Galerkin method with return mapping algorithms to allow for damage when undergoing large deformation to be analyzed along the interface of heterogeneous materials. These two methods are collectively used to find weaknesses and faults in newly discovered fibrous and directionally oriented materials.

TABLE OF CONTENTS

CHAPTER 1: INTRODUCTION

Fabrication of fiber-reinforced polymer matrix composites involves a number of complex interdependent processes. First, the mixing of thermoset polymer ingredients, resin and hardener, is achieved via a stochastic but finite sequence of folding, stretching, and cutting events [9]. Secondly, selective chemical affinity of the embedded material towards these constituents can enhance their separation. Thirdly, the cross-linking reactions are exothermic, and consequently self-catalyzing. Even autoclave treatment does not prevent the development of temperature gradients due to the difference between the thermal conductivities of polymer matrix and the embedded material [18]. This in turn results in differential chemical reactions along the interface and development of a composite with spatially inhomogeneous physical properties. Finally, upon extraction from autoclave, due to material mismatch, differential residual stresses are developed that can cause local debonding and crack propagation along these interfaces [19]. The properties of the interphase region are especially difficult to predict, unless their detailed constitutional history is known.

In this thesis we have investigated two aspects of processing and performance of composites. The first aspect that deals with processing of composites and involves chemo-mechanical stress fields employs a mixture theory based model. This model employs homogenization ideas, and while discrete representation of fibers and matrix is suppressed, the individual constituents are represented via independent momentum, energy, and mass balance equations to represent the evolution of the individual constituents. The constituents interact amongst themselves via interactive force fields that augment the momentum balance equations. The mixture model is locally homogeneous, but globally heterogeneous, and the properties of the constituents evolve as a function of chemical reactions locally at that point.

The performance modeling aspect of laminated and fibrous composites investigates the inter-material debonding and delamination. The interfacial interaction at the common interface is treated via a discrete modeling approach that is based on precise description of the two material subdomains via boundary fitted meshes. At the common interfacial boundary between the materials, interfacial coupling terms are introduced, that are derived by embedding DG ideas in the CG framework via the variational multiscale method.

1.1 MATRIX CHEMICAL CURING

A literature review reveals that several theoretical models and associated numerical schemes have been developed for structure-functional modeling and analysis of components made of composite materials [26,27,38,43]. The complexity of the process involved in the manufacturing of these engineered materials has been a challenge for the development of adequate numerical methods for process modelling. For example, in composite manufacturing, the fiber-resin mixture is subjected to a cure cycle under high temperature, initiating cross-linking polymerization in resin to produce a structurally hard composite [9]. The properties of the final product as well as its performance characteristics depend on the properties of constituents, processing parameters such as cure time, cure temperature, cure pressure and the chemical reaction in the resin. Due to the preferential adsorption of fibers, the chemical composition of resin near the fiber surface is different in comparison to the bulk resin. During curing, due to this change in constituent composition an interphase material is formed near the fiber surface. Of special significance is the network based curing model for polymers and their composites by Waas et. al. [9,18,19]. These works also show that a micromechanics model, with several renditions of packing geometries can accurately present the interaction between fiber and matrix and thus can be used to evaluate the interfacial tractions in the "interphase region", or in a regions of a coating, e.g., as in ceramic matrix composites.

Although numerical methods that involve explicit modeling of constituents and individual tracking of fiber/matrix/interphase result in a precise description of the composite, they result in a high cost of computation when applied at the structural or component level [43]. Mixture theory on the other hand provides reduced order models that are computationally economical at the mesoscopic level. From amongst the various mixture theories, the ones that yield locally homogeneous but globally heterogeneous models for multi-constituent materials, thereby allowing co-occupancy while still keeping track of kinematics and kinetics of individual phases (constituents) emerge as the most attractive alternative. In such mixture models each spatial point is occupied by all the constituents simultaneously. This assumption avoids the need to track/follow individual spatial points corresponding to individual constituents by capturing the mixture response macroscopically through constitutive models. These locally homogeneous but globally heterogeneous models reduce the cost of computation when compared to discrete modeling of individual components.

Bowen et al. [5] presented a thermomechanical theory for diffusion in mixtures of elastic materials. Bedford et al. [4] proposed a multi-continuum theory for composite materials, where the material particles of different constituents are grouped together at reference configuration to define a composite particle. Though these constituent particles occupy different spatial points as the material deforms, the interactions between constituents are evaluated in the reference configuration using the composite particle. This concept is employed in the present work to model the interactive force fields [12,16].

1.2 INTERFACIAL DEBONDING AND DAMAGE

In recently years, composites have been widely used in many engineering structures. As the material is inhomogeneous and anisotropic, actual modeling of the composite structures under different loading conditions are crucial [6]. For laminated composite material, in order to determine the in-plane elastic response, the lamination theory (LT) gives rise to the analytical technique. [44]. Later on, Pipes and Pagano [42] have proposed a finite –difference solution technique to obtain the stress and displacement distribution for layers with different orientations. Masud and Panahandeh [34] present a finite –element formulation of shells for the analysis of composite laminates.

For laminated composites especially, debonding between each layer is of interest [24]. An accurate modeling of the debonding phenomena across the inter-laminar surfaces is required. For modeling of debonding and damage, a classical approach is cohesive zone method [1,3,17,25,48]. For intrinsic cohesive zone method, it is shown in the literature that additional elastic stiffness is introduced which upsets the consistency and results in an inaccurate representation of the interface and the numerical simulation.

The basis of the methods developed in Masud's group is the theory of stabilized methods that is now a well-established framework for developing finite element formulations with enhanced stability and accuracy and applied to a wide range of problems in engineering and sciences [11,28-32,35,36,40]. With the objective of developing a general framework for local failure at material interfaces, Masud and coworkers developed a Lagrange multiplier method, in the context of small strains, for continuity of fields across embedded interfaces [50,53]. Variational multiscale method (VMS) [20,35] is adopted to eliminate the Lagrange multipliers which have the connotation of the interfacial traction field. In an allied effort a finite strain interface formulation for multi-material interfaces in the finite strain regime was developed in [25].

In this thesis we have employed the methods developed in [49] where a stabilized formulation for finite strain interface without damage is presented. The notion of inelastic residual gap was introduced in [49]. This method and code has been used to show the numerical simulations in this thesis. Problems with laminated composite materials are simulated. Both homogenous material and anisotropic material are used in this thesis. The stabilized formulation [7] is also applied for problems to track the debonding of the interfaces for single and multiple particle inclusions problems.

CHAPTER 2: MIXTURE THEORY MODEL FOR INTERPHASE EVOLUTION AND CURING

This chapter is based on the theory developed and presented in Gajendran et el [13]. We employ the computer program developed in that effort to carry out some interesting numerical simulations that highlight the underpinnings of the method developed in [12,13]. The code has been implemented in a parallel computing environment, using the supercomputing facilities available at the University of Illinois, and employing openMP environment [21]. In addition, we have adapted a thermal model for evolution of spatially variable mechanical properties of the manufactured material. With the help of numerical simulations, we highlight the time evolving anisotropy in the evolving material.

Before we present the numerical results, we first present a synopsis of Hari et al [13].

2.1 FLUID-SOLID CURING MIXTURE MODEL

Hall and Rajagopal [15] have proposed a mixture theory model for diffusion of a chemically reacting fluid through an anisotropic solid. The model is based on the maximization of the rate of entropy production constraint, considering anisotropic effective reaction rates and the limits of diffusion-dominated (diffusion of the reactants is far more rapid than the reaction) and reaction-dominated processes (the reaction is far more rapid than the diffusion of the reactants). Earlier, Kannan and Rajagopal [22] had developed a constrained mixture model (no relative motion between constituents) for chemically reacting components that included stoichiometric equations, to study the complicated problem of vulcanization of rubber. Modifications to the Hall and Rajagopal model [15], as complemented by Hall [14], were employed in Gajendran et al [13] for the formation and evolution of an interphase material contribution to an initially two-constituent material where all constituents are in the solid phase. In this model, the properties of the matrix constituent neighboring the fiber-matrix interface evolve during a cure cycle, and the reaction process model is associated with an anisotropic tensor that provides coupling of chemical reaction and mechanical stresses.

As there is no interconversion of mass between matrix and fiber material, conservation of mass for the matrix and fiber/reinforcement can be given as,

$$\rho^m J^m = \rho_R^m \tag{2.1}$$

$$\rho^r J^r = \rho_R^r \tag{2.2}$$

where the superscripts *m*, *r* refer to matrix and fiber/reinforcement, respectively. ρ_R^m, ρ_R^r are the apparent reference densities of matrix and fiber with respect to the reference mixture volume, respectively. Conservation of linear momentum for the two constituent is written as,

$$\text{DIV}\, \boldsymbol{T}^m + \rho^m \boldsymbol{b}^m + \boldsymbol{I}^m = \rho^m \frac{D\boldsymbol{v}^m}{Dt} \tag{2.3}$$

$$\text{DIV}\, \boldsymbol{T}^r + \rho^r \boldsymbol{b}^r + \boldsymbol{I}^r = \rho^r \frac{D\boldsymbol{v}^r}{Dt} \tag{2.4}$$

To keep the presentation concise, the superscript $\alpha \in \{m, r\}$ is used to represent both matrix *m* and reinforcement *r*. In (2.3) and (2.4) $\boldsymbol{T}^\alpha$ is the Cauchy stress, $\boldsymbol{b}^\alpha$ is the body force and $\boldsymbol{I}^\alpha$ is the interactive force acting on the α^{th} component in the mixture. According to Newton's third law, the interactive force acting between the matrix and fiber follows the relation,

$$\boldsymbol{I}^r = -\boldsymbol{I}^m \tag{2.5}$$

2.1.1 Constitutive relations based on maximization of rate of dissipation

The thermodynamic system of the mixture [14,15] comprised of two solid constituents was assumed to be defined by the following set of state variables.

$$s\left[t\right] = s\left\{\boldsymbol{F}^m, \boldsymbol{F}^r, \rho^m, \rho^r, \theta, \Gamma\right\}\left[t\right] \tag{2.6}$$

where $\boldsymbol{F}^\alpha$ is the deformation gradient of the α^{th} component, Γ is the extent of chemical reaction in current configuration and θ is the temperature of the mixture. In application of eqn. (2.6), it is implied, as is normally true in composites, that the densities are negligibly weak functions of deformation; thus a limited range of volumetric deformations is implied. The actual densities of the converted and unconverted matrix regions are assumed to be quite similar, while the associated material properties of the two regions need not be.

The Helmholtz free energy function of the mixture [14,15] is defined as:

$$\psi = \psi\left[s\left(t\right)\right] = \psi\left\{\boldsymbol{F}^m, \boldsymbol{F}^r, \rho^m, \rho^r, \theta, \Gamma\right\} \tag{2.7}$$

In the component form, the mixture Helmholtz free energy function is given as,

$$\begin{aligned} \rho\psi &= \rho^m\psi^m + \rho^r\psi^r \\ \rho &= \rho^m + \rho^r \end{aligned} \tag{2.8}$$

where ψ^α is the Helmholtz free energy function of the α^{th} component and ρ is the mixture density.

From a set of admissible class of constitutive relations, the following relations are obtained [14,15] by enforcing the maximum rate of dissipation constraint. These relations also correspond to the case [15] where the volume additivity constraint is not required.

$$\boldsymbol{T}^m = \rho \boldsymbol{F}^m \left(\frac{\partial \psi}{\partial \boldsymbol{F}^m} \right)^T - \rho^m \left(g^m + \frac{\rho^r}{\rho} \left(\psi^r - \psi^m \right) \right) \mathbf{1} \tag{2.9}$$

$$\boldsymbol{T}^r = \rho \boldsymbol{F}^r \left(\frac{\partial \psi}{\partial \boldsymbol{F}^r} \right)^T - \rho^r \left(g^r + \frac{\rho^m}{\rho} \left(\psi^m - \psi^r \right) \right) \mathbf{1} \tag{2.10}$$

$$\begin{aligned} \boldsymbol{I}^m = {} & g^m \frac{\rho^r}{\rho} \nabla \rho^m - g^r \frac{\rho^m}{\rho} \nabla \rho^r + \rho^r \frac{\partial \psi}{\partial \boldsymbol{F}^m} : \nabla \boldsymbol{F}^m - \rho^m \frac{\partial \psi}{\partial \boldsymbol{F}^r} : \nabla \boldsymbol{F}^r \\ & - (\nabla \theta) \frac{\rho^m \rho^r}{\rho} (\eta^m - \eta^r) \end{aligned} \tag{2.11}$$

where η^α and g^α are the entropy and chemical potential of the α^{th} component of the mixture. The chemical potential of the α^{th} constituent in (2.9) is given as

$$g^\alpha = \rho \frac{\partial \psi}{\partial \rho^\alpha} \tag{2.12}$$

2.1.2 Constitutive Model for the Mixture

Gajendran et al [13] consider a constitutive model wherein the thermal field has pronounced effect on the evolving mechanical field, while the reverse coupling of the mechanical field with the thermal field is considered weak. The constitutive relations (2.9)-(2.11) are modified based on the specified constitutive equations and the interphase model. The reduced form of Helmholtz functionals for the matrix and fiber are:

$$\psi^m[\boldsymbol{E}^m,\theta,t]=\frac{1}{\rho_T^m}\left\{\frac{1}{2}\lambda^m\left(tr\left[\boldsymbol{E}^m-a^{m0}\boldsymbol{I}(\theta-\theta_{\boldsymbol{R}})\right]\right)^2+\mu^m tr\left[\left(\boldsymbol{E}^m-a^{m0}\boldsymbol{I}(\theta-\theta_{\boldsymbol{R}})\right)^2\right]\right\}+\Lambda^m \tag{2.13}$$

Using (2.12)-(2.13) and (2.7)-(2.8) in (2.9), the matrix stress can be rewritten as,

$$\boldsymbol{T}^m=\boldsymbol{F}^m\left(\frac{\partial(\rho\psi)}{\partial\boldsymbol{E}^m}\right)^T\left(\boldsymbol{F}^m\right)^T-\left(\rho^m\right)^2\frac{\partial\psi^m}{\partial\rho^m}\boldsymbol{I} \tag{2.14}$$

and additionally, assuming an additive decomposition of ψ^m into thermoelastic and inelastic parts yields:

$$\begin{aligned}\frac{\partial\left(\rho\psi\right)}{\partial\boldsymbol{E}^m}&=\rho^m\frac{\partial\psi^m}{\partial\boldsymbol{E}^m}\\&=\frac{\rho^m}{\rho_T^m}\left\{\lambda^m tr\left[\boldsymbol{E}^m-a^{m0}\boldsymbol{I}\left(\theta-\theta_R\right)\right]\boldsymbol{I}+2\mu^m\left[\boldsymbol{E}^m-a^{m0}\boldsymbol{I}\left(\theta-\theta_R\right)\right]\right\}+\rho^m\frac{\partial\Lambda^m}{\partial\boldsymbol{E}^m}\end{aligned} \tag{2.15}$$

where Λ^m is the coupling term between the matrix strain and the extent of chemical reaction. θ_R is the reference temperature, ρ_T^m is the matrix true density and a^{m0},λ^m,μ^m are matrix material constants. The last term in (2.15) is taken in a hereditary form:

$$\rho^m\frac{\partial\Lambda^m}{\partial E_{IJ}^m}=-\frac{1}{\rho_T^m}\left\{E_{OP}^m\int k\left[\rho^c,\Gamma^0\right]\tilde{K}_{IJOP}\left[\Gamma^0\right]d\Gamma^0+\int\int m^c\left[\rho^c,\Gamma^0\right]\tilde{\alpha}_{IJ}^c\left[\theta\right]d\theta d\Gamma^0\right\} \tag{2.16}$$

In (2.16), $k\left[\rho^c,\Gamma^0\right]$ is the bulk modulus of the composite which is a function of the converted matrix (interphase) density and the extent of reaction and is defined as $k\left[\rho^c,\Gamma^0\right]=c_1\,\rho^c$ and c_1 is a constant of proportionality, $\tilde{K}_{OPQR}\left[\Gamma^0\right]$ (with major and minor symmetries) is the stiffness of the interphase material, $m^c\left[\rho^c,\Gamma^0\right]$ is a function of the converted matrix density as well as the extent of reaction, and $\tilde{\alpha}_{OP}^{c}\left[\theta\right]$ is the interphase coefficient of thermal expansion. In the current implementation of the model, thermal expansion is ignored and therefore the second term in (2.16) is neglected.

Likewise, the Helmholtz free energy function of the reinforcement in reference coordinates accounts for the effect of thermal field on the mechanical properties of the fibrous constituent, while ignoring thermal expansion effects. Using (2.12) and (2.7) in (2.10), the reinforcement stress can be rewritten as:

$$\boldsymbol{T}^{r} = \boldsymbol{F}^{r}\left(\frac{\partial\left(\rho\psi\right)}{\partial \boldsymbol{E}^{r}}\right)^{T}\left(\boldsymbol{F}^{r}\right)^{T} \tag{2.17}$$

In the absence of drag force between solid constituents under isothermal conditions, and neglecting the contribution to the interactive force due to matrix and fiber chemical potentials, the interactive force acting on the matrix (2.11) can be further simplified as in Hall [14]:

$$\boldsymbol{I}^{m} = \frac{\rho^{r}\rho^{m}}{\rho}\left(\frac{\partial\psi^{m}}{\partial\boldsymbol{F}^{m}}:\nabla\boldsymbol{F}^{m} - \frac{\partial\psi^{r}}{\partial\boldsymbol{F}^{r}}:\nabla\boldsymbol{F}^{r}\right) \tag{2.18}$$

2.2 WEAK FORM AND LINEARIZATION OF GOVERNING EQUATIONS

The spaces of trial solutions for the matrix and reinforcement are:

$$\mathcal{S}_{t}^{m} = \left\{\boldsymbol{\varphi}_{t}^{m}:\Omega\rightarrow\mathbb{R}^{nsd} \mid \boldsymbol{\varphi}_{t}^{m}\in H^{1}\left(\Omega\right),\ \boldsymbol{\varphi}_{t}^{m}=\bar{\boldsymbol{\varphi}}_{t}^{m}\ \text{ on }\ \partial\Omega_{u}\right\} \tag{2.19}$$

$$\mathcal{S}_{t}^{r} = \left\{\boldsymbol{\varphi}_{t}^{r}:\Omega\rightarrow\mathbb{R}^{nsd} \mid \boldsymbol{\varphi}_{t}^{r}\in H^{1}\left(\Omega\right),\ \boldsymbol{\varphi}_{t}^{r}=\bar{\boldsymbol{\varphi}}_{t}^{r}\ \text{ on }\ \partial\Omega_{u}\right\} \tag{2.20}$$

The spaces of weighting functions for the matrix $\mathcal{V}^m$ and reinforcement $\mathcal{V}^r$ are the homogeneous and time independent counterparts of the corresponding spaces of trial solutions $\mathcal{S}_t^m$ and $\mathcal{S}_t^r$, respectively.

Taking the inner product of (2.3) and (2.4) with the corresponding weighting functions and integrating over the domain leads to the weighted residual form:

$$\int_\Omega w_i^\alpha \left(T_{ij,j}^\alpha + \rho^\alpha b_i^\alpha + I_i^\alpha \right) d\Omega = 0 \tag{2.21}$$

where α represents both matrix and fiber. Integrating (2.21) by parts and using divergence theorem yields the weak form for the mixture model which is stated as: Given the boundary conditions $\bar{\boldsymbol{\varphi}}^m = \bar{\boldsymbol{\varphi}}^r$ on $\boldsymbol{\varphi}^\alpha \left(\partial\Omega_u \right)$ and the initial conditions, find $\boldsymbol{\varphi}^m \in \mathcal{S}_t^m$ and $\boldsymbol{\varphi}^r \in \mathcal{S}_t^r$, such that

$$\int_\Omega w_{i,j}^\alpha T_{ij}^\alpha d\Omega - \int_\Omega w_i^\alpha \rho^\alpha b_i^\alpha d\Omega - \int_\Omega w_i^\alpha I_i^\alpha d\Omega = 0, \qquad \alpha \in \{m, r\} \tag{2.22}$$

An important issue in mixture theory based models is the Neumann boundary conditions where the constituents need to be tied in a self-consistent fashion to simulate the response of a material where constituents are fully bonded. The methods employed in the numerical simulations shown in this thesis have employed a finite strain finite element method for consistent tying of the constituents at the boundaries via a variational formulation that finds roots in the VMS method [12].

A good overview of the class of stabilized methods is provided in [28] and first applications of these methods in the domain of solid and structural mechanics is presented in [11]. A literature review reveals the classes of stabilized finite element methods that have been developed for mixed field elasticity problems [37,51]. A new class of stabilized methods finds roots in the Variational

Multiscale framework [29,30,33,35,36] wherein it is shown in [36] that stabilized displacement formulations have an equivalence with the classical ***F***-bar method [49]. We have employed interior stabilized method in this work.

2.3 THE CURING MODEL

2.3.1 The Matrix Curing model

In fiber reinforced polymeric composites, fiber materials are often oriented to provide the designed structural properties in the desired direction. These fiber materials are interlocked with a weaker material (a thermoset resin) and allowed to cure through a polymerization process. The matrix material is comprised of resin and hardener and catalysts are usually present in the hardener to accelerate cure. Because of chemical reactions, the viscosity of the thermoset increases and ultimately cross linking occurs due to growth and branching of chains, leading to an increase in the molecular mass. A model for resin kinetics and evolution of composite properties during curing for glass-polyester composites is presented in Ruiz and Trochu [45,46].

$$E_r\left(T,\Gamma\right)=E_{agp}\left(T\right)+\left[E_c\left(T\right)-E_{agp}\left(T\right)\right]F_r\left(\Gamma\right)W_r\left(T_g\right) \tag{2.23}$$

where

$$\begin{aligned}
&E_c\left(T\right)=\frac{\hat{E}_c}{\cosh\left(a_1T\right)^{b_1}}, \quad E_{agp}\left(T\right)=\frac{\hat{E}_{agp}}{\cosh\left(a_2T\right)^{b_2}}\\
&F_r\left(\Gamma\right)=c\exp\left(d\hat{\beta}\right)+e\,\hat{\beta}\\
&W_r\left(T_g\right)=h\exp\left(\hat{T}\right), \quad T_g\left(\Gamma\right)=a_g\exp\left(\frac{b_g}{1-\hat{\beta}}\right)
\end{aligned} \tag{2.24}$$

In (2.23) $E_r\left(T,\Gamma\right)$ is the resin elastic modulus which is a function of the temperature field, β is the degree of cure, and T is the glass transition temperature. $a_1, a_2, c, d, b_g, \hat{\beta}, \hat{E}_c, \hat{E}_{agp}$ are constitutive parameters. We embed this model within the mixture theory framework in the context of finite strain finite element method. The parametric values employed for the numerical implementation of the model are obtained from [45,46].

For the mixture theory described in Section 2.1.2, the evolution of matrix properties is given by the interphase evolution function $\tilde{K}\left(\Gamma^0\right)$. In the mixture model, this function is defined as the derivative of the Ruiz model for evolution of Young's modulus with respect to the cure parameter. Accordingly, by taking the functional form of $\tilde{K}\left(\Gamma^0\right)$ to be the first derivative of $E_r\left(T,\Gamma\right)$ given in (2.23), we embed the Ruiz and Trochu [45,46] model in equation (2.16) of the mixture theory presented in Section 2.1.2

$$\tilde{K}\left(\Gamma^0\right)=\frac{\partial E_r}{\partial \Gamma}=\left(E_c\left(T\right)-E_{agp}\left(T\right)\right)\left(\frac{\partial F_r}{\partial \Gamma}W+\frac{\partial W_r}{\partial \Gamma}F_r\right) \tag{2.25}$$

In the present thesis we have employed the Kamal-Sourour kinetic model [43] for use in the evolution of matrix stress via equation (2.14).

$$\dot{\Gamma}^0=\left(K_1+K_2\Gamma^0\right)\left(1-\Gamma^0\right)^2 \tag{2.26}$$

where K_1 and K_2 are the rate constants. Further details can be reached in Gajendran et al [12].

2.3.2 Adapting a Temperature Dependent Matrix Curing Model from Experimental Composites

An experimental process called Brillouin Light Scattering (BLS)[23] allows numerical analysis to be performed on a new class of composite materials similar to that analyzed in Heinrich et al. [18]. This material experienced high temperature chemical reaction to cure the system. Using a Levenberg-Marquardt nonlinear curve fit over the first 220 minutes of data at 316°C, the time dependent model for longitudinal modulus has been proposed in the following format:

$$M = a\left(1 - e^{-t/\tau}\right) + b + ct \tag{2.27}$$

From (2.28), the constants are defined as: a = 1.695GPa, b = 3.816GPa, τ = 10min, and

c = -0.0028min^{-1}. Likewise, the degree of cure includes a first order time dependent reaction such that

$$\phi = A\left(1 - e^{-t/\tau}\right) \tag{2.28}$$

In eqn. (2.29), the constant A=0.85 as derived from atomistic simulations [18] and represents the maximum degree of cure achieved by the material. Using equations (2.27) and (2.28) as the reference experimental data, all future calculations will be calibrated to the two time dependent equations.

With the initial model prepared through the experimental data on the new material, the cure expresses singular dependence on time, so an additional model implementation is necessary to introduce an additional dependency on temperature. For this reason, the Kamal-Sourour format of the Arrhenius equations[18, 43] are adapted in a way similar to equation (2.27). The curing process has a kinetic process of the form

$$\dot{\Gamma}^0 = f\left(T, \Gamma^0\right) \tag{2.29}$$

Here, T is defined as the temperature which makes the function representing the evolution of cure non-negative. The temperature-dependent function, $f\left(T, \Gamma^0\right)$, has been proposed to have the following form:

$$f\left(T, \Gamma^0\right) = \left(K_1(T) + K_2(T)\left[\Gamma^0\right]^m\right)\left(1 - \Gamma^0\right)^n \tag{2.30}$$

$$K_1(T) = A_1 \exp\left(-\frac{\Delta E_1}{TR}\right) \tag{2.31}$$

$$K_2(\mathrm{T}) = \mathrm{A}_2 \exp\left(-\frac{\Delta E_2}{TR}\right) \tag{2.32}$$

Where m and n are power constants, R is the gas constant, A_1 and A_2 are frequency like constants, and ΔE_1 and ΔE_2 are the activation energies [18].

For the reactionary case for the current material, the equation (2.30) can be simplified to depend on a single reaction coefficient by setting $K_2(T)$ to zero. The adjustment is justified since $K_2(T)$ contributes weakly to the behavior of the overall model [10]. Also, a first order reaction is used since there is no experienced delay of the curing in the reaction of the material. Therefore, the power constant, n, is set equal to one to create a simplified Temperature dependency from the time dependent curing model as found in equation (2.28) [10]. This is shown in the following form:

$$\dot{\Gamma}^0 = K_1(T)\left(1 - \Gamma^0\right) \tag{2.33}$$

$$K_1 = A_1 \exp\left(-\frac{\Delta E_1}{TR}\right) \tag{2.34}$$

Similarly, Γ^0 is the degree of cure, T is the temperature (in Kelvin), R is the gas constant, A_1 is used to represent a frequency constant, and ΔE_1 shows the activation energy for the system. By taking the derivative of equation (2.28) and introducing the time dependent curing models into equation (2.33), the following equivalence is shown:

$$\frac{A}{\tau}\exp\left(-\frac{t}{\tau}\right) = K_1(T)\left[1-\left(A - A\exp\left[-\frac{t}{\tau}\right]\right)\right] \tag{2.35}$$

Equation (2.35) has a simple solution when the curing constant, A=1 even though the experimental analysis of the material has a curing constant at A=0.85. For the sake of numerical analysis, the current calculations will be presented using the simplified A=1 solution. The maximum degree of cure is then set at 1.0 instead of 0.85. Solving equation (2.35) yields:

$$K_1(\mathrm{T}) = \frac{1}{\tau} \tag{2.36}$$

Plugging in equation (2.34) into equation (2.36) allows a solution set to be shown for calculating ΔE_1 and A_1.

$$A_1 \exp\left(-\frac{\Delta E_1}{TR}\right) = \frac{1}{\tau} \tag{2.37}$$

$$\Delta E_1 = TR\ln(A_1\tau) \tag{2.38}$$

Therefore, for the simplified model, any combination of ΔE_1 and A_1 that satisfies equation (2.38) will have a solution for the curing evolution equation. The presented values obtained for ΔE_1 and A_1, for this case, are $7.3\text{x}10^4$ J/mol and $2.9\text{x}10^5$ min^{-1} respectively.

Within a time dependent loop, using the constants found in equation (2.38), the degree of cure is updated through the use of the updating implementation of Backward Euler expressed as:

$$\Gamma^0{}_{n+1} = \Gamma^0{}_n + \dot{\Gamma}^0(dt) \tag{2.39}$$

In going from loading step n to n+1, $\dot{\Gamma}^0$ is the change in the degree of cure with respect to time as calculated in equation (2.33) and dt is the change in time step from $\Gamma^0{}_n$ to $\Gamma^0{}_{n+1}$. By combining equations (2.27) and (2.28), an equation for the Longitudinal modulus can be created that has a dependency on degree of cure instead of time. The importance for this change allows for the temperature dependency modeled in the cure to adopt a temperature dependency in the Longitudinal modulus through the resulting equation.

$$M(\Gamma^0) = \frac{a}{A}\Gamma^0 + b - c\tau \ln\left(1 - \frac{\Gamma^0}{A}\right) \tag{2.40}$$

Note that the curing constant from eqn. (2.29) is shown by A=1, while the modulus constants, τ, a, b, and c are adapted from the same values used in eqn. (2.28) to reflect the results from the temperature dependent model. After calculating the longitudinal modulus, the scaling factor, A*=0.85, is introduced. Since the calculations of the Longitudinal modulus are correct based on the curing constant A=1, the scaling factor is only used on the degree of cure to scale the model to match the experimental results such that

$$\Gamma^{0*}{}_{n+1} = A^*\Gamma^0{}_{n+1} \tag{2.41}$$

Note that Γ^{0*}_{n+1} will have a maximum degree of cure at the scaling factor A*. The resulting degree of cure and longitudinal modulus is shown in Fig. 2-1.

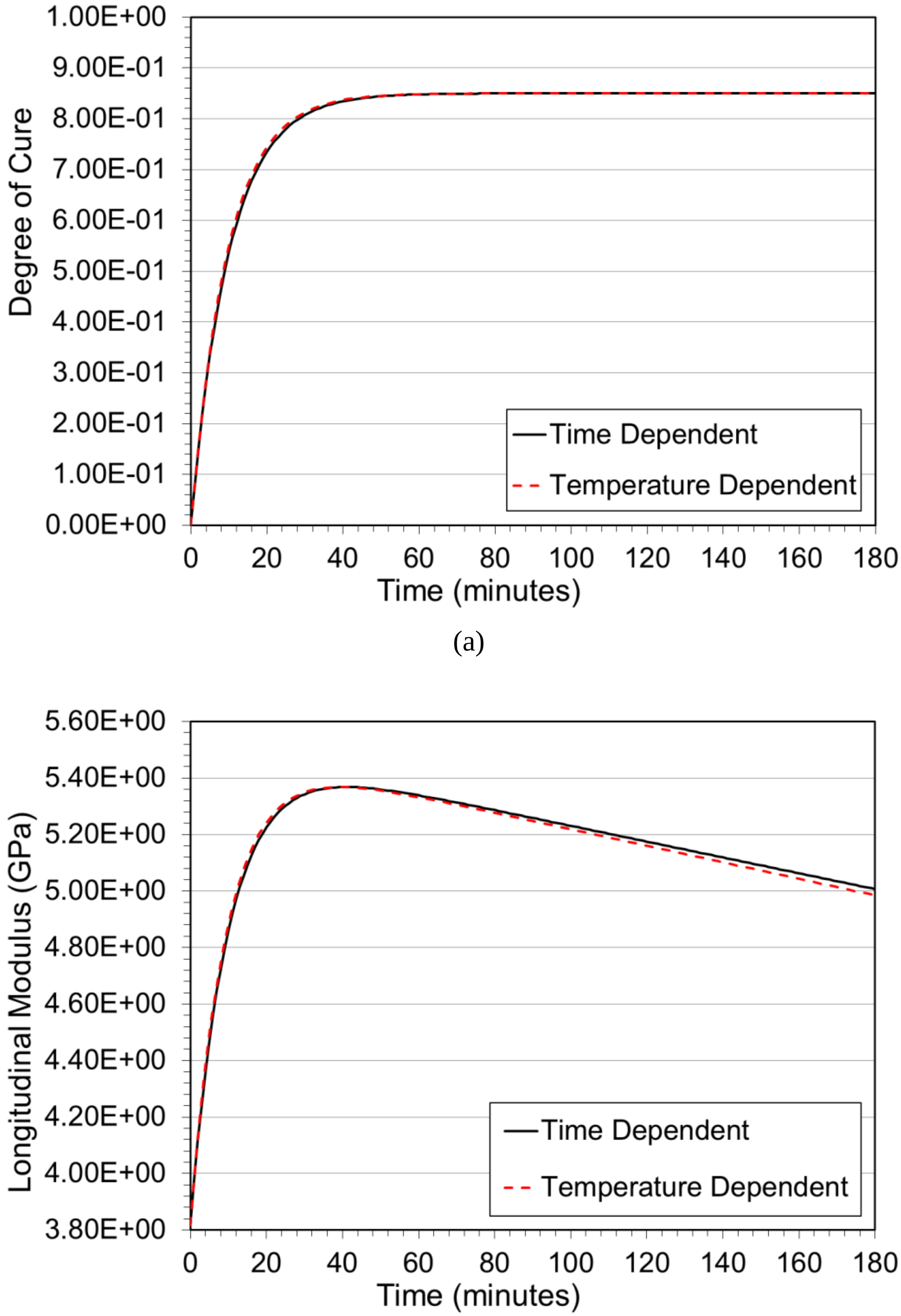

(a)

(b)

Fig. 2-1: The degree of cure (a) and longitudinal modulus (b) for the first 180 minutes of curing at 316°C. The solid line is the curve fitted data with time dependency while the dotted line is the adapted Kamal-Sourour Model to include Temperature dependency to the curing model.

From the derivation for the longitudinal modulus, the generalized Cauchy relationship between the longitudinal and shear moduli is presented in the proceeding relation [23]:

$$G = \frac{M - B}{3} \tag{2.42}$$

In Equation (2.42), the constant B is set to approximately 3 for epoxy. The calculation of longitudinal and shear allows us to calculate the Young's modulus and Poisson's ratio which is shown in the following form [23]:

$$E = \frac{G(3M - 4G)}{M - G} \tag{2.43}$$

$$\nu = \frac{M - 2G}{2(M - G)} \tag{2.44}$$

Using equations (2.43) and (2.44), the Elastic Modulus and Poisson's ratio are used to calculate the Cauchy stress, the strain displacement matrix, and the Matrix of Material Moduli.

Remark: In this work temperature is treated as a given field. For the case of a coupled chemo-mechano-thermal model where temperature evolution takes place, a stabilized form for the thermal field as presented in [2] can be adopted.

2.4 NUMERICAL RESULTS AND MODEL VALIDATION

2.4.1 Temperature Dependency on Adapting a New Curing Mixture Model

Since the addition of the Temperature dependence has proven to show equivalence to the original proposed data from eqns. (2.28) and (2.29), the expected material properties should hold if temperature changes across the spacial domain in the newly implemented model. In Fig. 2-2, the degree of cure and Longitudinal modulus is shown over the first 180 minutes. As expected, the speed of curing increased as the composite material undergoes higher temperatures and decreases as the material experiences lower temperatures. Adjusting from the original experimental data, the maximum degree of cure has been redefined to be a value of 1.0, and the new model exhibits a similar horizontal asymptote for maximum curing across all applied temperature levels. For the longitudinal modulus distribution shown in Fig. 2-2b, as temperature increases, the magnitude of the gradient also increases with respect to time. The increase in the gradient shows that the longitudinal modulus grows and decays at a faster rate to reflect the increased rate of curing.

Remark: The adjustment to the maximum cure to 1.0 instead of 0.85 has been made for several reasons:

1. The Temperature dependent model already shows consistency to that of the experimental data.
2. Since the degree of cure in the experimental data does not exceed 0.85, it makes more sense to have the maximum degree of cure at 1.0.
3. The longitudinal modulus is modeled after the degree of cure having a maximum value of 1.0 which allows the A* factor to be removed from all future implementation of the coded model.

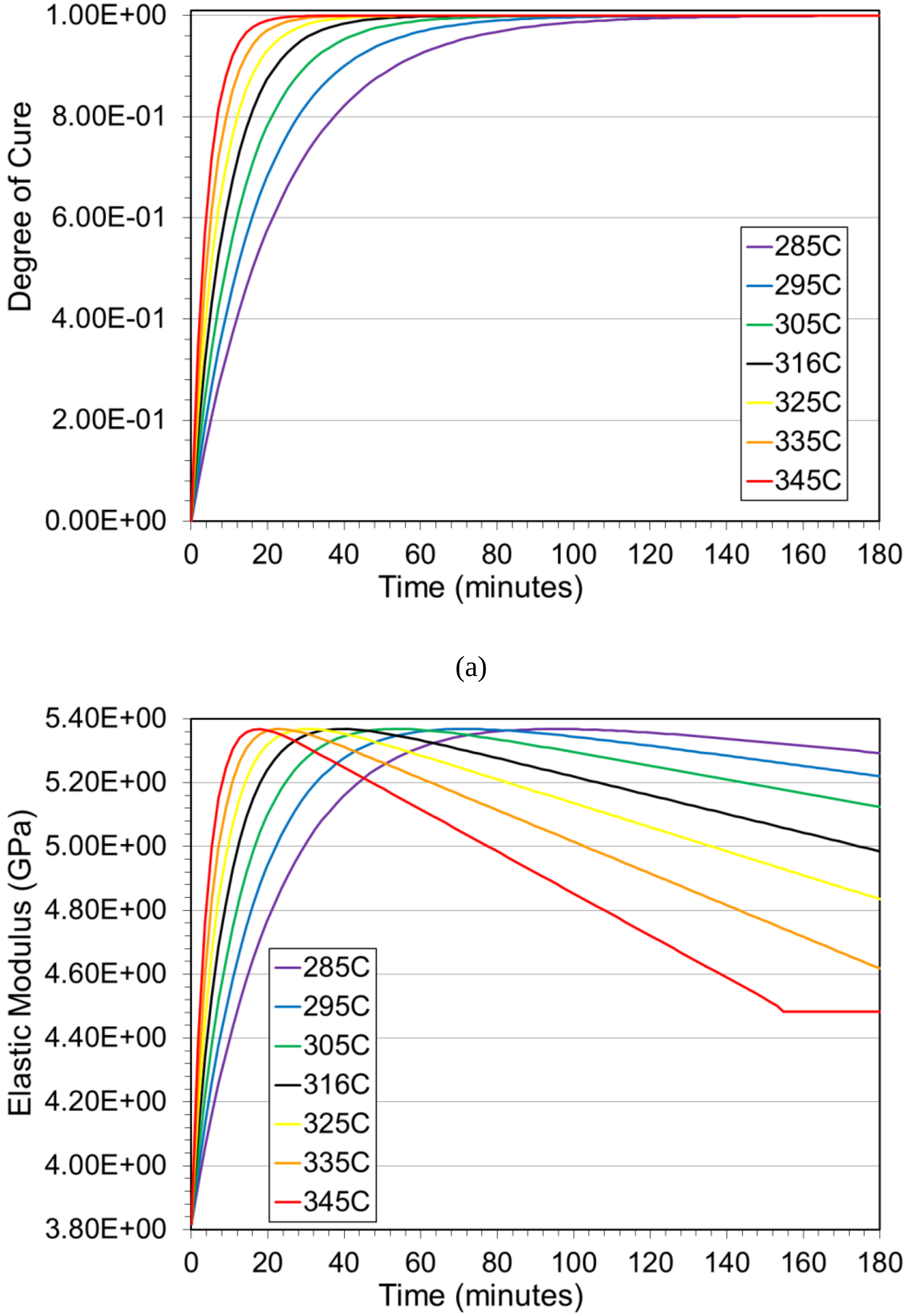

(a)

(b)

Fig. 2-2: The degree of cure (a) and longitudinal modulus (b) for the first 180 minutes of curing. The black line shows the experimental temperature used to create the time dependent model with 3 temperature variations above and below the original fitted model.

According to Fig. 2-3, the temperature variations do not cause any deviation in the plotted correlation between longitudinal modulus versus cure in addition to shear modulus versus cure. After 180 minutes, the only major difference is shown at the end where the modulus has evolved more at higher temperatures since it has cured at a faster rate. Since the generalized Cauchy relationship was used between the Longitudinal modulus and the Shear modulus for the same degree of cure as shown in equation (2.42), the evolution trend of the two curves have a similar shape. Also, the large drop in elastic modulus as the degree of cure approaches 1.0 represents how this class of materials [18] has an inverse reaction when the material nears full curing as opposed to the initial, practically linear, trend.

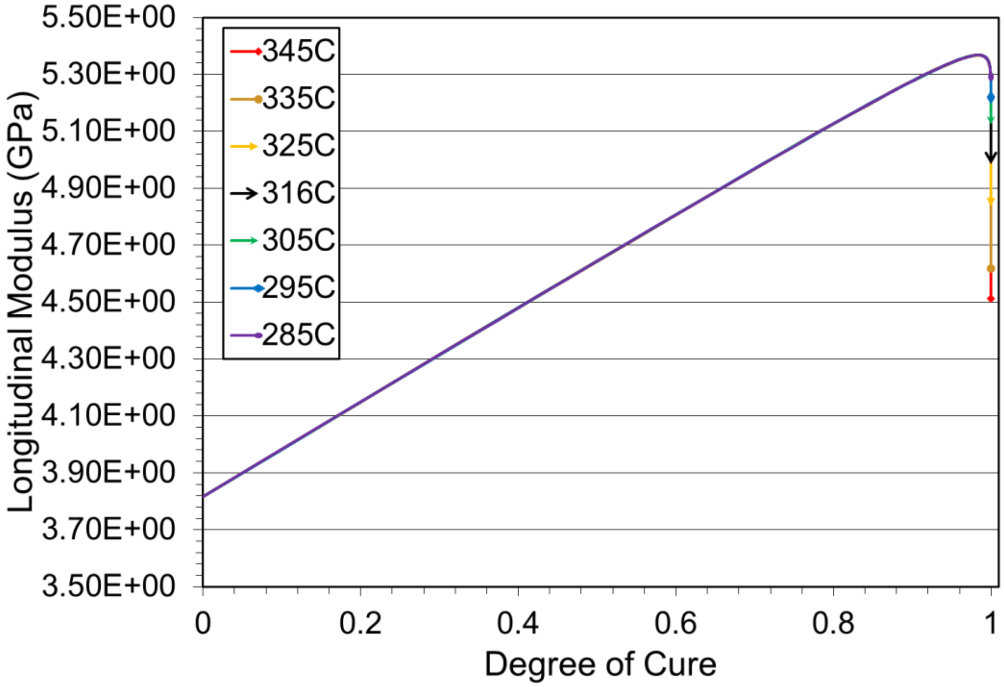

(a)

Fig. 2-3: The longitudinal (a) and shear (b) modulus as a function of degree of cure for the first 180 minutes. The black line shows the Temperature used in the time dependent model with 3 temperature variations above and below the original fitted model.

Fig. 2-3: (cont.)

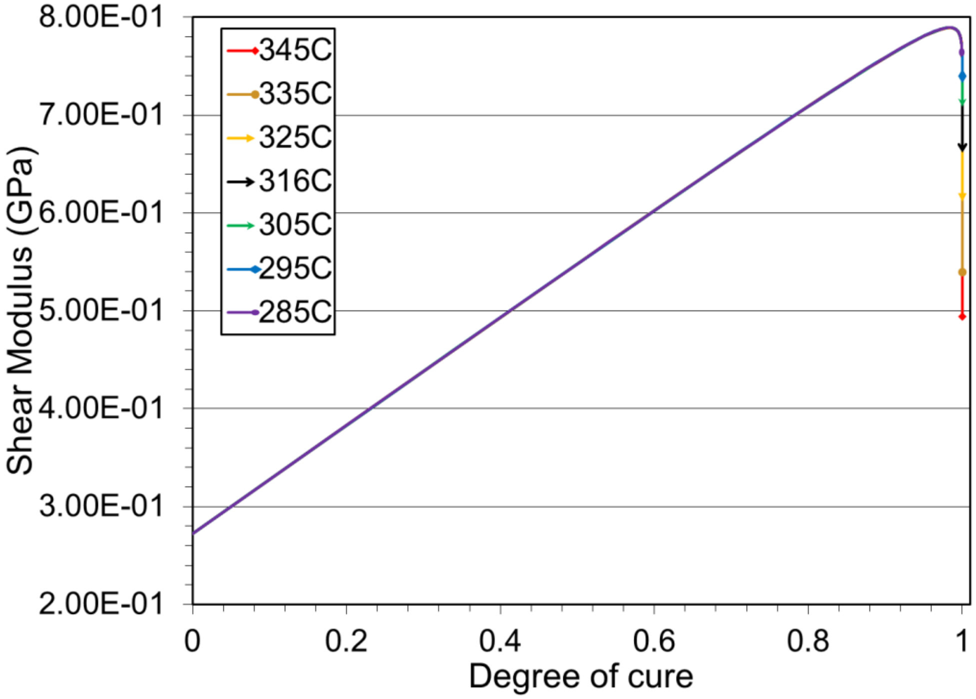

(b)

As the temperature increased to 345°C, the degree of cure reached its maximum value within machine precision at approximately 150 minutes. Because the new temperature dependent model has the longitudinal modulus depend entirely on the degree of cure, the longitudinal modulus also experiences no change after the 150 minute mark. However, the longitudinal modulus proposed by equation (2.27), should continue to change in time even as the degree of cure reaches a horizontal asymptote at the full cure of 1.0. To validate the inferred discrepancy, the model was ran for the first 500 minutes in hopes to compare the original time dependent and the newly developed temperature dependent models at 316°C as shown in Fig. 2-4.

Based on Fig. 2-4a, the temperature dependent model fits well to the degree of cure over time with minimal difference between the two models for the first 500 minutes. As expected in the comparison of the longitudinal moduli between the two models from Fig. 2-4b, the time dependent model continues on the original trajectory after 325 minutes while the temperature dependent model no longer changes since the cure no longer changes, as shown in equation (2.40).

Remark: Despite the difference between the two models, the temperature dependent model still correlates to the experimental data and is physically sound based on the following reasons:

1. The experimental data used the first 220 minutes to capture the time dependent model. Any part of the new model does not show obvious changes from eqn. (2.27) until after the analyzed time period.
2. When the material reaches the maximum degree of cure, the longitudinal modulus should no longer change with respect to time.
3. If the curve fitted data continued to cure for an extended period of time, based on the current trajectory, the model would eventually reach a negative elastic modulus. At this point the model would be physically impossible.

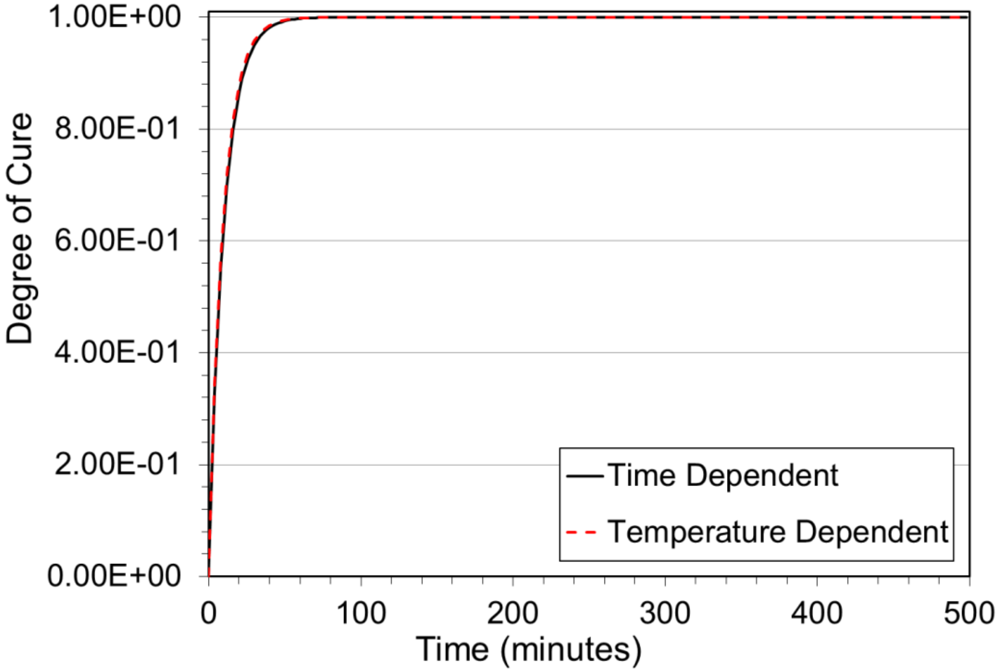

(a)

Fig. 2-4: The degree of cure (a) and longitudinal modulus (b) as a function of time over the first 500 minutes. The solid line is the time dependent curing model with time dependency while the dotted line is the adapted Kamal-Sourour Model to include Temperature dependency to the curing model. Note that the maximum degree of cure of 0.85 is used to compare the two models.

Fig. 2-4: (cont.)

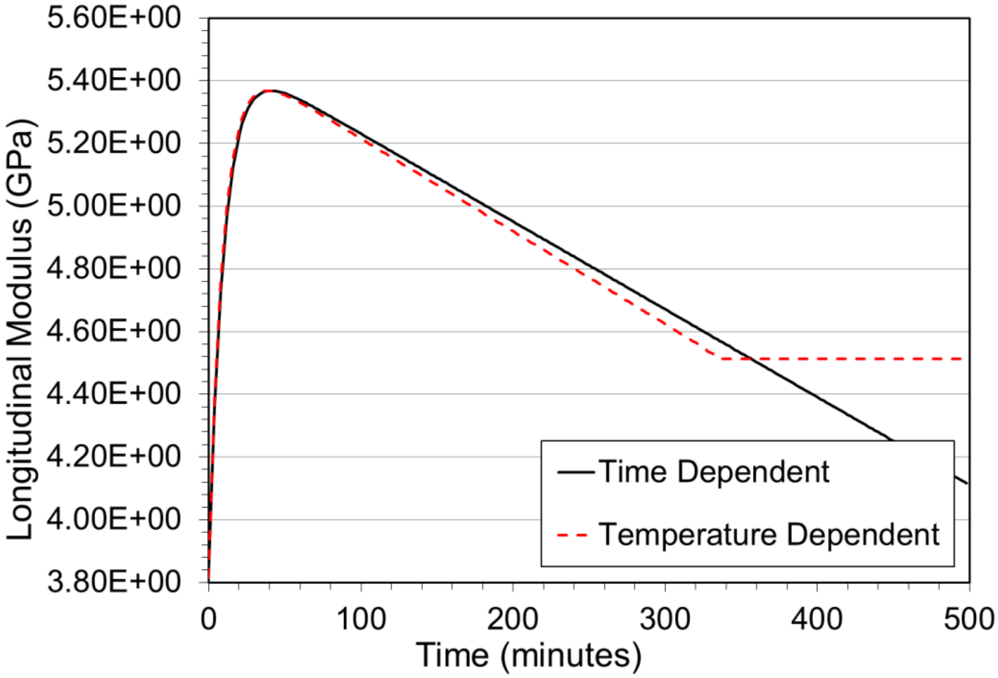

(b)

Since the prior data gathered in Fig. 2-2b and 2-4b shows a point where the longitudinal modulus no longer changes with respect to time for two different temperature fields, the various temperature fields were plotted out to the first 500 minutes with respect to time, as found in Fig. 2-5. Here, when the material at each temperature reaches its full degree of cure, the longitudinal modulus is found to be a consistent value between the temperature fields. The plot also demonstrates a predicted time when any future heating of the material would demonstrate little to no effect on the degree of cure and longitudinal modulus. As seen in the trend found in Fig. 2-2b, the highest temperature field in Fig. 2-5b is the first to reach full curing and demonstrate no change in the longitudinal modulus followed by the next highest temperature field and so on.

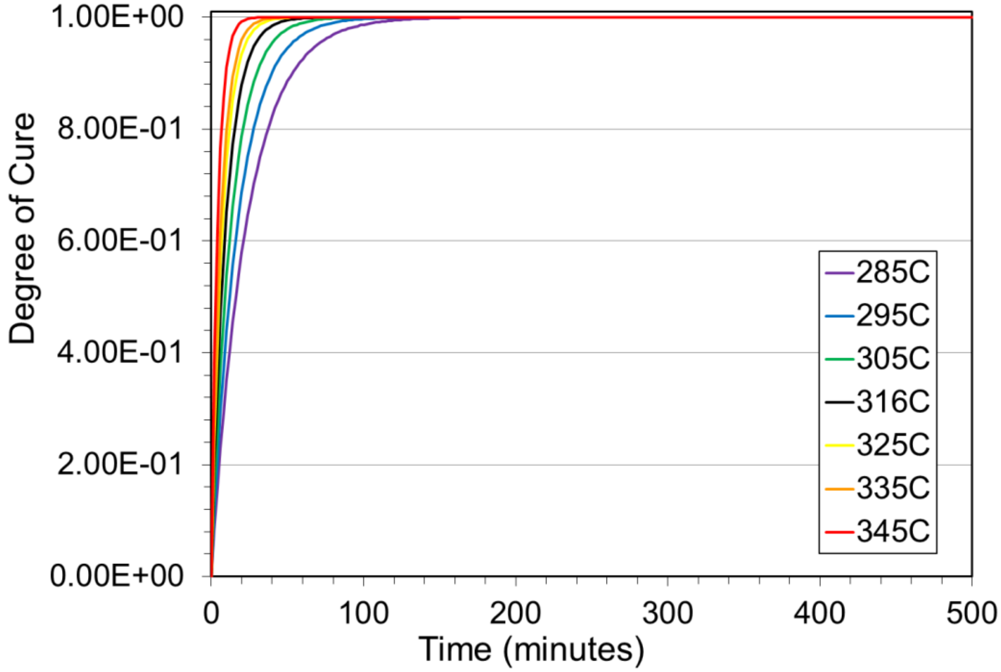

(a)

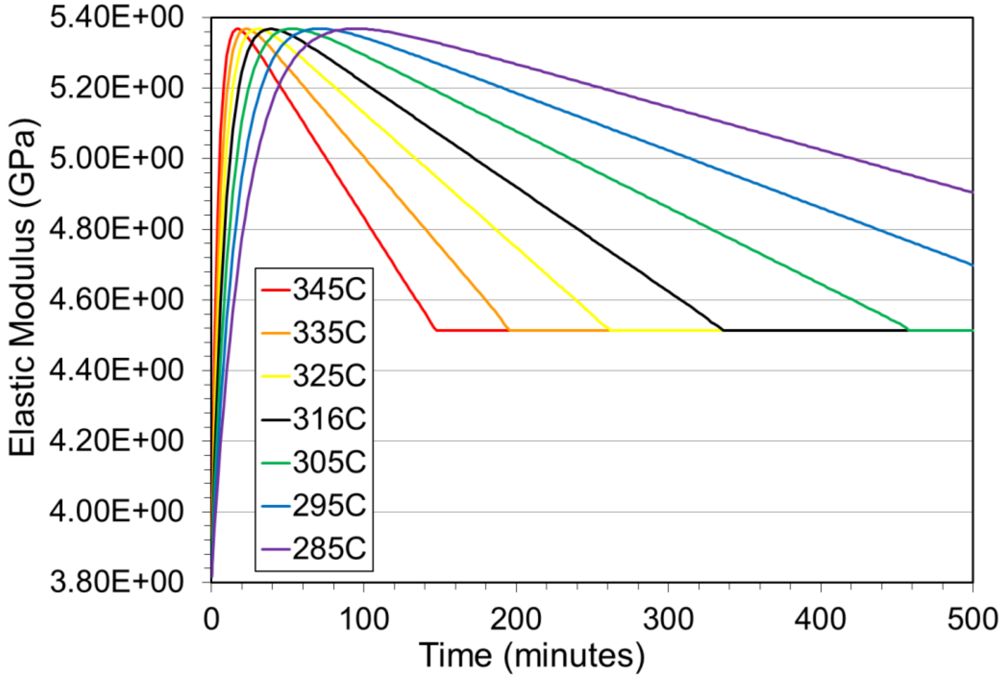

(b)

Fig. 2-5: The degree of cure (a) and longitudinal modulus (b) for the first 500 minutes of curing. The black line shows the Temperature used in the time dependent model with 3 temperature variations above and below the original fitted model.

2.4.2 Adapting the Spatial dependent Temperatures for a lower temperature profile

To account for small differences in the temperature (±50°C) across the spacial domain, the Arrhenius equation has been coded to determine the mixture stresses and interactive forces across the spacial domain for varying degree of cure and longitudinal modulus. However, if the reduced Kamal-Sourour model for 316°C, adapted from the time dependent experimental curve fit in eqns. (2.28) and (2.29), experiences lower temperature fields (i.e. 200°C), the curing model never reaches the full expected curing value. Therefore, the experimental analysis of this material data in the similar class of materials as [18] does not match the new model. Since the longitudinal modulus has been coded to have a strict dependency on the curing behavior, the longitudinal modulus, also, does not reflect the projected time dependent model. To allow for accurate analysis of a lower temperature profile, a similar adaptation can be used to determine new coefficients for equations (2.27) and (2.34) applied to a lower temperature profile by doing a curve fit of the projected values at 200°C for the experimental results for the longitudinal modulus over time. Even though the time dependent equation for the longitudinal modulus change to adapt to the new temperature profile, the maximum degree of cure is still at 1.0 to show the maximum cure that the material experiences at the new temperature with a similar time dependent profile as equation (2.28). The Levenberg-Marquardt nonlinear curve fit for the first 220 minutes of data at 200°C is used to calculate the new constants.

From the longitudinal modulus equation (2.27), the new adapted constants for the 200°C temperature profiles are $a = 1.633\text{GPa}$, $b = 4.714\text{GPa}$, $\tau = 10\text{min}$, and $c = -0.0055\text{min}^{-1}$. Using the new longitudinal modulus equation, a simultaneous curve fitting plot is used to calculate the new Arrhenius equation coefficients found in equation (2.34). For 200°C, the two coefficients are

A_1=1.05e+6 and ΔE_1= 6.38e+4. By using the same A* to show the consistency between the curing behavior at the lower temperature, this allows us to show whether the adapted Kamal-Sourour model of the Arrhenius equation [10,18] works for the lower temperature profile as shown in Fig. 2-6. Notice how the scaled curing behavior for the lower temperature profile range yields a new longitudinal modulus which can have various temperatures across the spacial domain. Therefore, the modeling for this material is adapted to having a working temperature distribution along the spacial domain for Temperatures ranging from 150°C to 250°C as well as 266°C to 366°C.

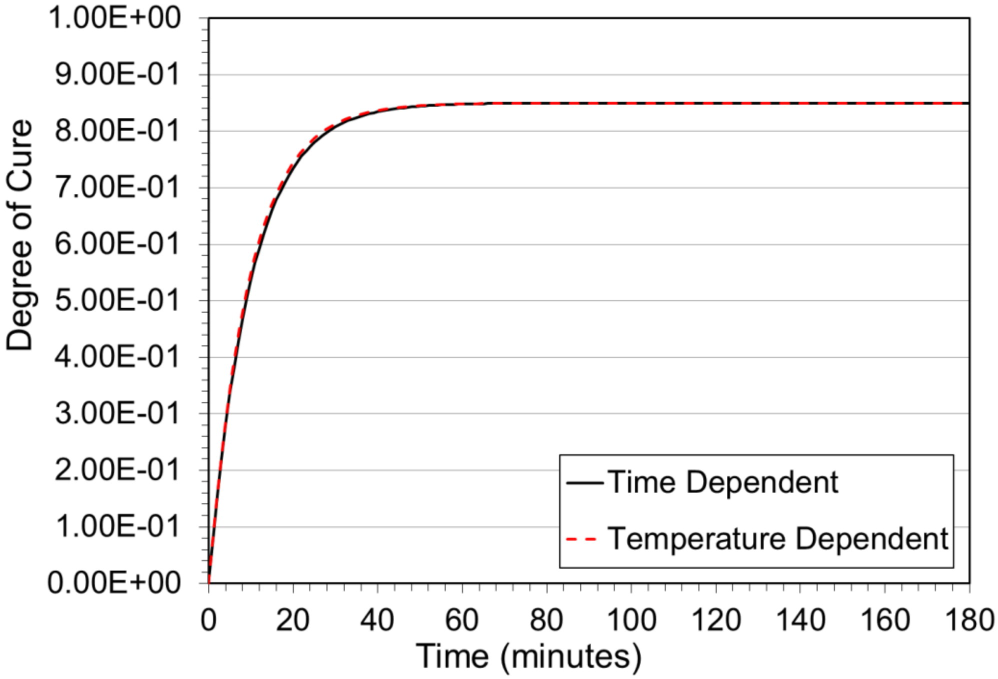

(a)

Fig. 2-6: The degree of cure (a) and longitudinal modulus (b) for the first 180 minutes of curing at 200°C. The solid line is the curing model with time dependency while the solid line is the adapted Kamal-Sourour Model to include Temperature dependency to the curing model.

Fig. 2-6: (cont.)

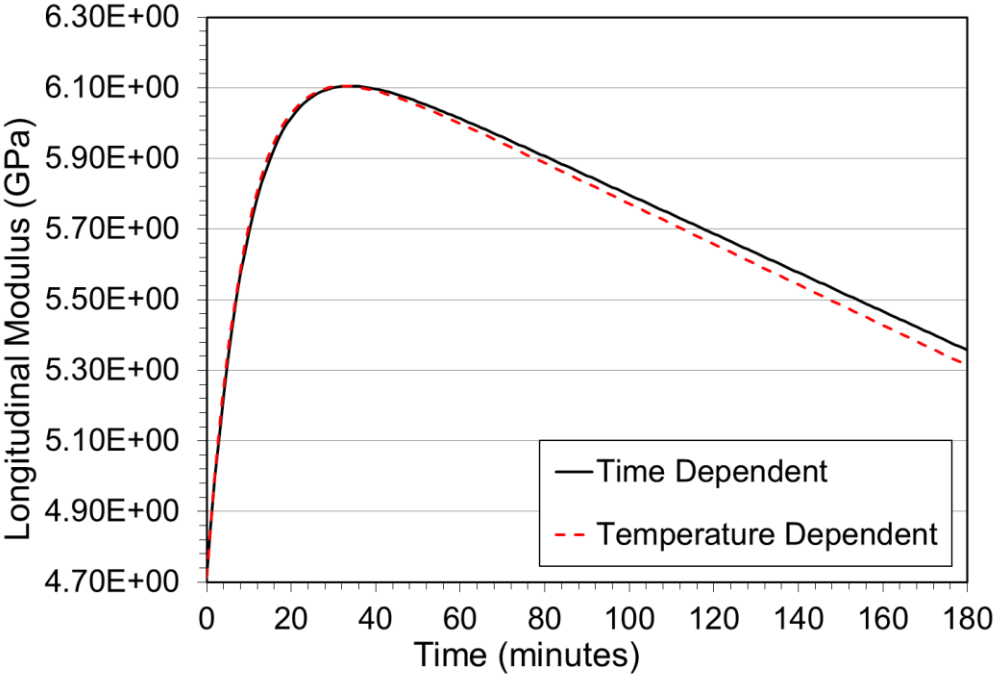

(b)

Since the correlation between the two models for the degree of cure and longitudinal modulus has been shown at the constant temperature field of 200°C, the temperature can be adjusted in the Kamal-Sourour Model to include the new behaviors experienced by varying the temperature across the spacial domain. Shown in Fig. 2-7, the change in temperature has a similar effect to the degree of cure and longitudinal modulus plots where the speed that the material cures increases as the temperature increases which causes the longitudinal modulus to develop at a faster rate. Some differences develop between the two models that are worth mentioning. First of all, the same change in temperature at the lower temperature field causes larger changes in the response in the degree of cure and longitudinal modulus than experienced in the higher temperature field. Next, the larger changes cause the higher temperature variations to develop faster as well as the lower temperature variations to develop slower than what occurred at 316°C. Due to the increased speed in the degree of cure for the higher variations, the "plateau" for the longitudinal modulus is reached at a faster time than the higher temperature field. Finally, when the material is considered to be fully cured, the "plateau" occurs at a lower longitudinal modulus than the higher temperature model.

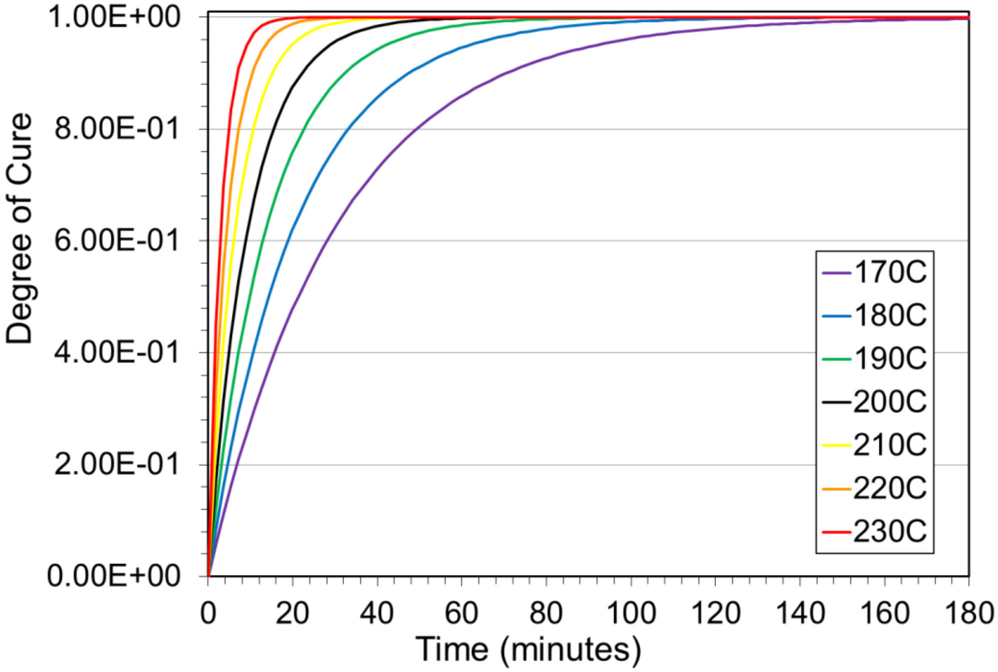

(a)

Fig. 2-7: The degree of cure (a) and longitudinal modulus (b) for the first 180 minutes of curing at 200°C. The black line shows the Temperature in the time dependent model with 3 temperature variations above and below the original fitted model.

Fig. 2-7: (cont.)

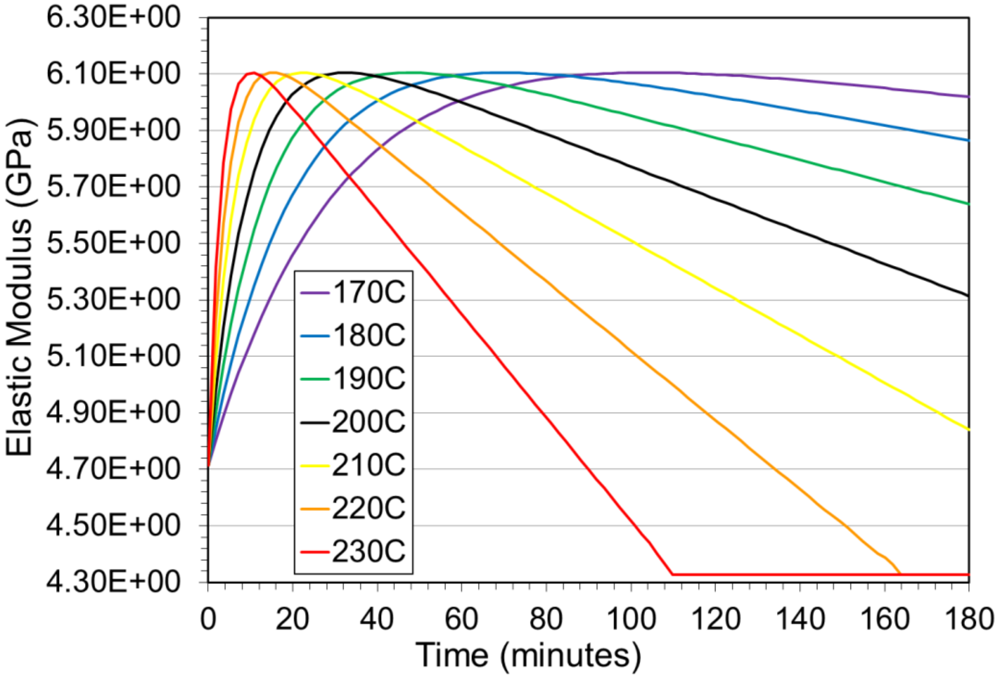

(b)

2.4.3 Performance modeling for a single ply.

To test a mesh model for a single ply plate with an x-direction from -30 to +30, y-direction from -10 to +10, and the thickness of the material to go from 0 to 0.625, a parabolic temperature profile is applied along the domain where the maximum temperature of 316°C is applied along the faces with the normal of the plane in the direction of positive and negative x-axis and the minimum temperature at 296°C when the x component is equal to 0. From Fig. 2-8, two points are analyzed at the maximum temperature and the minimum temperature to test the performance modeling of the system. These points will be used to show the effects of the degree of cure and longitudinal modulus over time due to differences in the temperature domain over the spacial domain. For this problem, the fitted constants at 316°C are plugged into the equations for the longitudinal modulus and Kamal-Sourour model which updates our degree of cure.

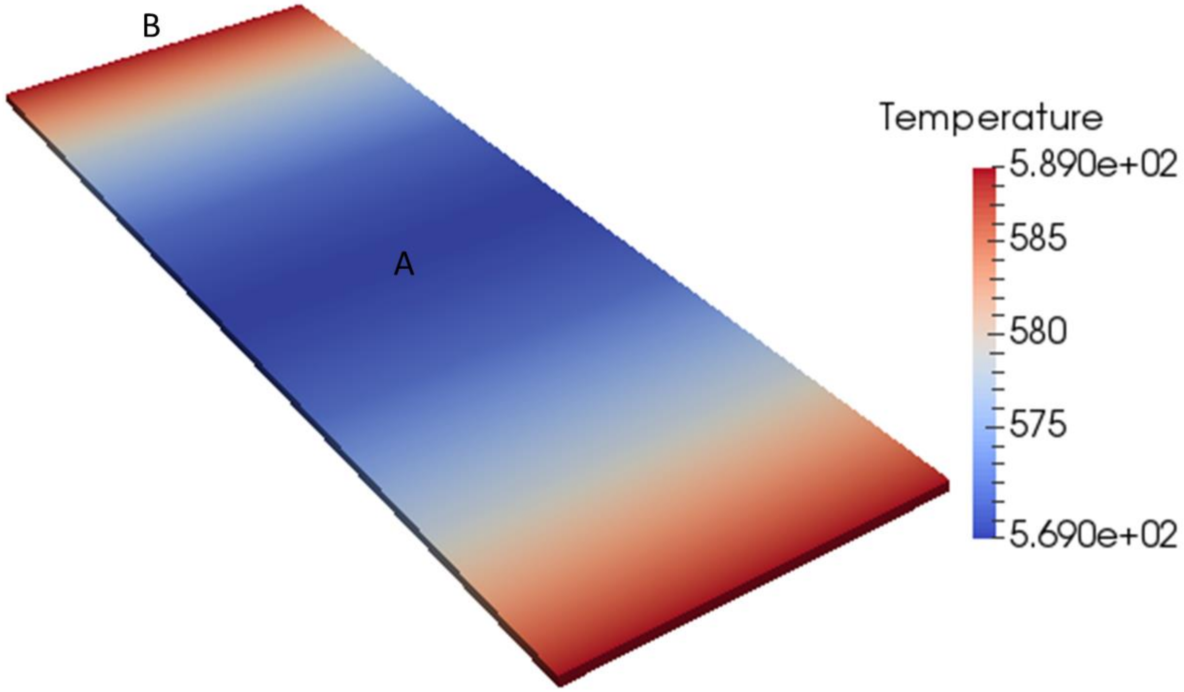

Fig. 2-8: Parabolic temperature distribution for a single ply laminate with the minimum temperature located along point A at 296°C (569K) and the maximum temperature located along point B at 316°C (589K).

Based on the parabolic temperature distribution in Fig. 2-8, the direct impact on the degree of cure and the longitudinal modulus are shown along three different time steps to show the development for the fibrous composite material overtime and are shown in Fig. 2-9. For Fig. 2-9a, the longitudinal modulus and degree of cure seem to have nearly the identical profile distribution where the areas corresponding to high temperature fields experienced curing first followed by areas experienced to lower temperatures. At 100 minutes as found in Fig. 2-9b, the degree of cure has reached nearly 100 percent where the longitudinal modulus has begun to invert the distribution where the low temperature locations correspond to the higher points of longitudinal modulus. However, at this point, the variation between points A and B have little variance across the domain.

When looking at Fig. 2-9c, corresponding to 300 minutes of curing, not only does the additional exposure to heat after the material is fully cured cause the longitudinal modulus to decrease, but the variation between the longitudinal modulus at areas of high temperature and the longitudinal modulus at areas of low temperature increase as well.

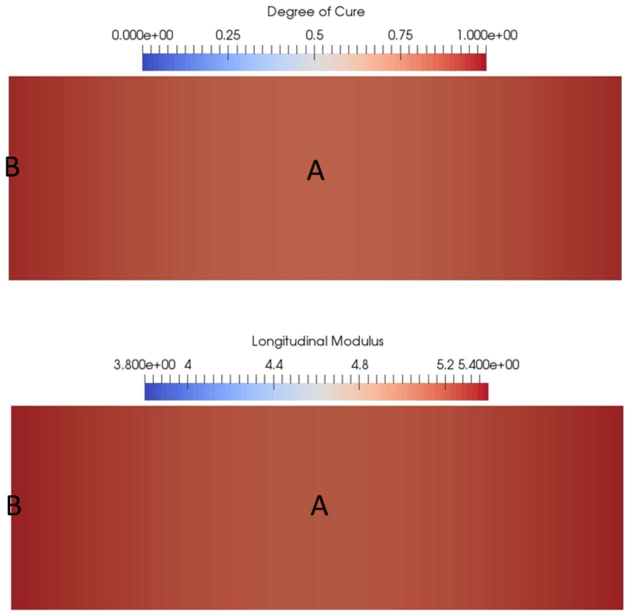

(a)

Fig. 2-9: Degree of cure at the longitudinal modulus at 30 minutes (a), 100 minutes (b), and 300 minutes (c) for a parabolic temperature distribution for a single ply laminate. The scale for the degree of cure ranges from 0 (referring to no curing in the material) and 1 (showing that the material is fully cured. Likewise, the scale for the longitudinal modulus ranges from 3.800 GPa (the minimum elastic modulus value) and 5.400 GPa (the maximum elastic modulus value).

Fig. 2-9: (cont.)

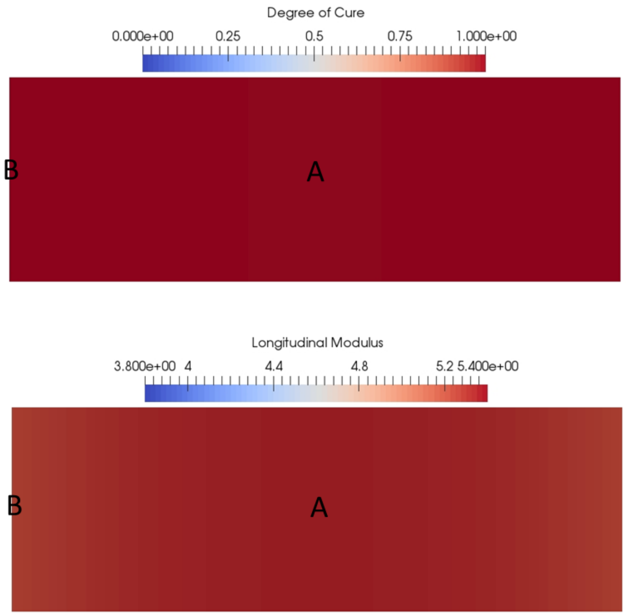

(b)

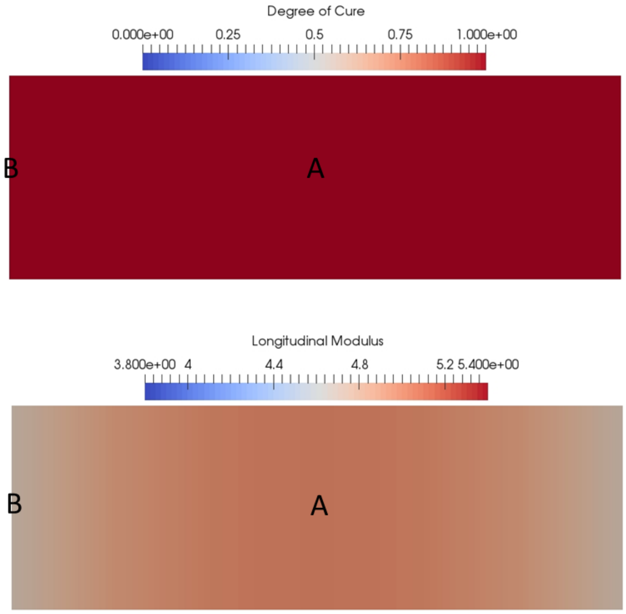

(c)

With the understanding of how the distribution develops throughout the entire domain, the variation between areas of high temperature and low temperature can be plotted and compared as shown in Fig. 2-10. For the degree of cure, the higher temperature location corresponding to point B cures at a higher rate which corresponds to the previous distribution data in Fig. 2-2. For the longitudinal modulus, point B has a higher correlated longitudinal modulus until about 50 minutes when the two points invert. This behavior demonstrates the decay of the longitudinal modulus starts to compromise the areas of high temperature while the areas of low temperature is being developed. In addition, since the longitudinal modulus is decaying at a faster rate for the higher temperatures, the variation in the longitudinal modulus increases between points A and B which matches the behavior exhibited in Fig. 2-9b and 2-9c. Since the material behavior has been correlated to experimental data, the axial loading and corresponding mixture stresses of the material can be determined through a two material coupling system.

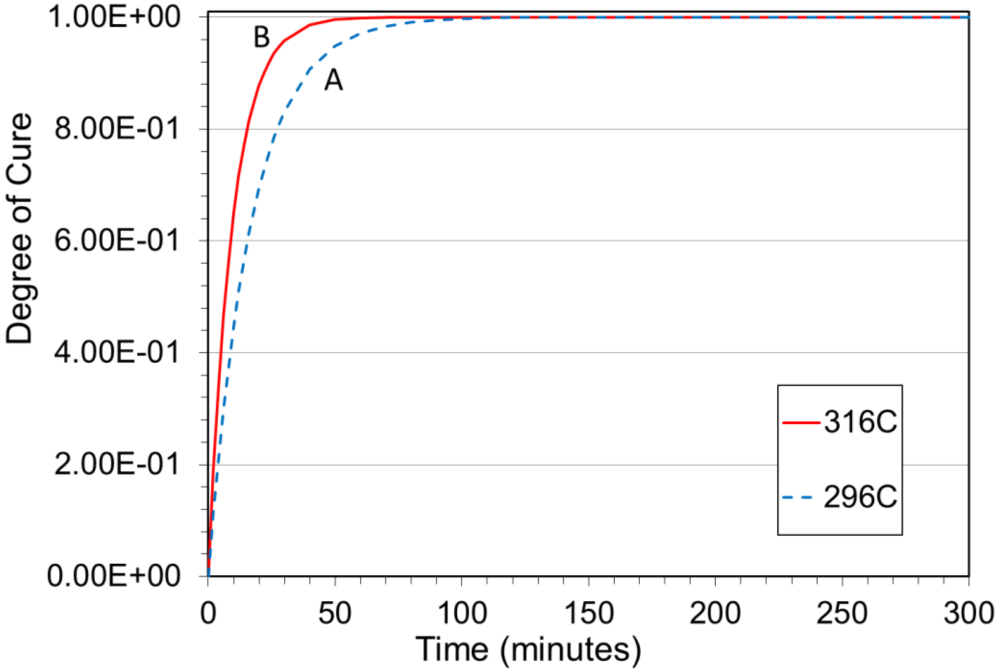

(a)

Fig. 2-10: The degree of cure (a) and longitudinal modulus (b) for the first 300 minutes for the two corresponding point in the parabolic temperature profile. The blue line is the degree of cure and longitudinal modulus at point A while the red line is the degree of cure and longitudinal modulus at point B.

Fig. 2-10: (cont.)

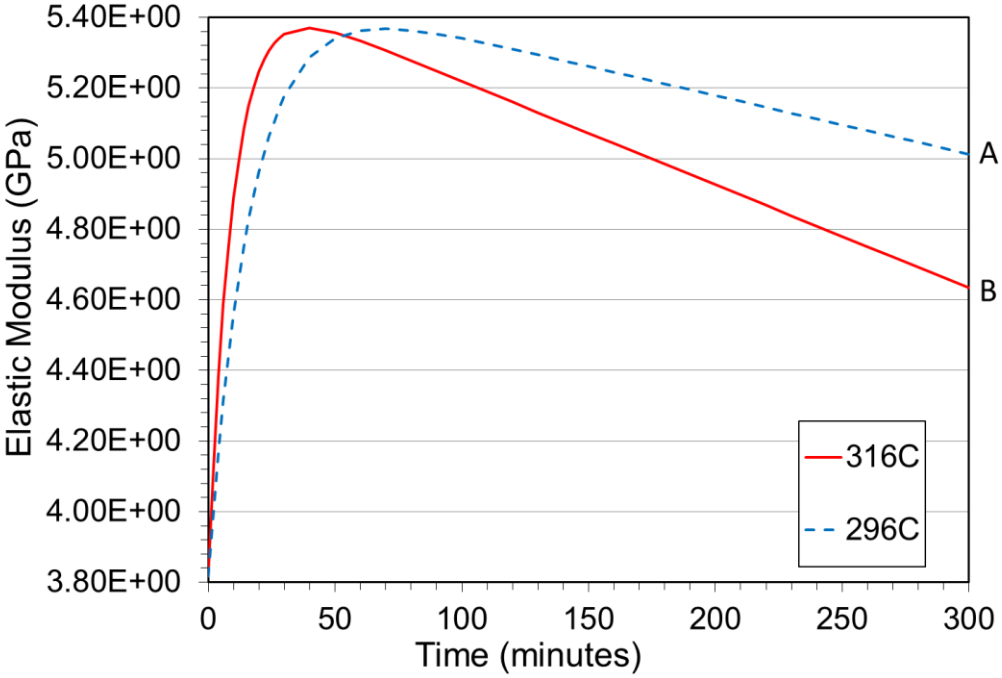

(b)

2.4.4 Curing and coupled chemo-mechanical evolution in a plate with hole

This test case presents three dimensional implementation of the cure and interphase evolution model employing quadratic brick elements. The constitutive model is tri-axial, however it is implemented in the three dimensional kinematic context. We consider a graphite-epoxy composite prismatic domain of dimensions $60 \times 20 \times 0.625$ *mm* with a circular hole of radius 1.0 *mm*. The nodes are appropriately constrained at $x = 0$ plane to avoid rigid body motion. The properties of this pre-impregnated composite with fiber orientation of zero degrees are shown in Table 2-1. Initially, the resin is assumed to have a very low elastic modulus. Composite is then allowed to cure until the matrix reaches a fully cured state of 0.99. A prescribed temperature field is applied (Fig. 2-11a) to model the effects of the thermal field during the curing process. The temperature field is assumed to have a constant value of 413 K along the entirety of the plate. It is assumed that the temperature of the mixture and its components are equal and constant with respect to time, while it varies spatially over the domain. The lamina is subjected to an axial traction of 2 MPa at $x = \pm 30$ plane in the axial direction until the matrix reaches a cure value of 0.99. The data is analyzed with a time step of 25 seconds. Load is gradually increased from zero to 2 MPa at time 25 sec, and is then held constant till time 300 sec. Once the matrix is fully cured, the laminate is unloaded.

Fig. 2-11 (a,b) shows the normalized thickness around the circumference. As time evolves, curing results in increase and elastic modulus and the evolving mechanical properties get manifested via the evolving stress. Fig. 2-11a shows 3E-05 change in the normalized thickness around the circumference, and this change in shape is attributed to the initial tensile force applied to the specimen. Fig. 2-11b shows the zoomed view which highlights the elastic recovery due to increase in internal resistive force that is attributed to the increase in the magnitude of the elastic modulus that recovers the deformation under the given constant load, as shown by plots at 100, 200 and 300 seconds.

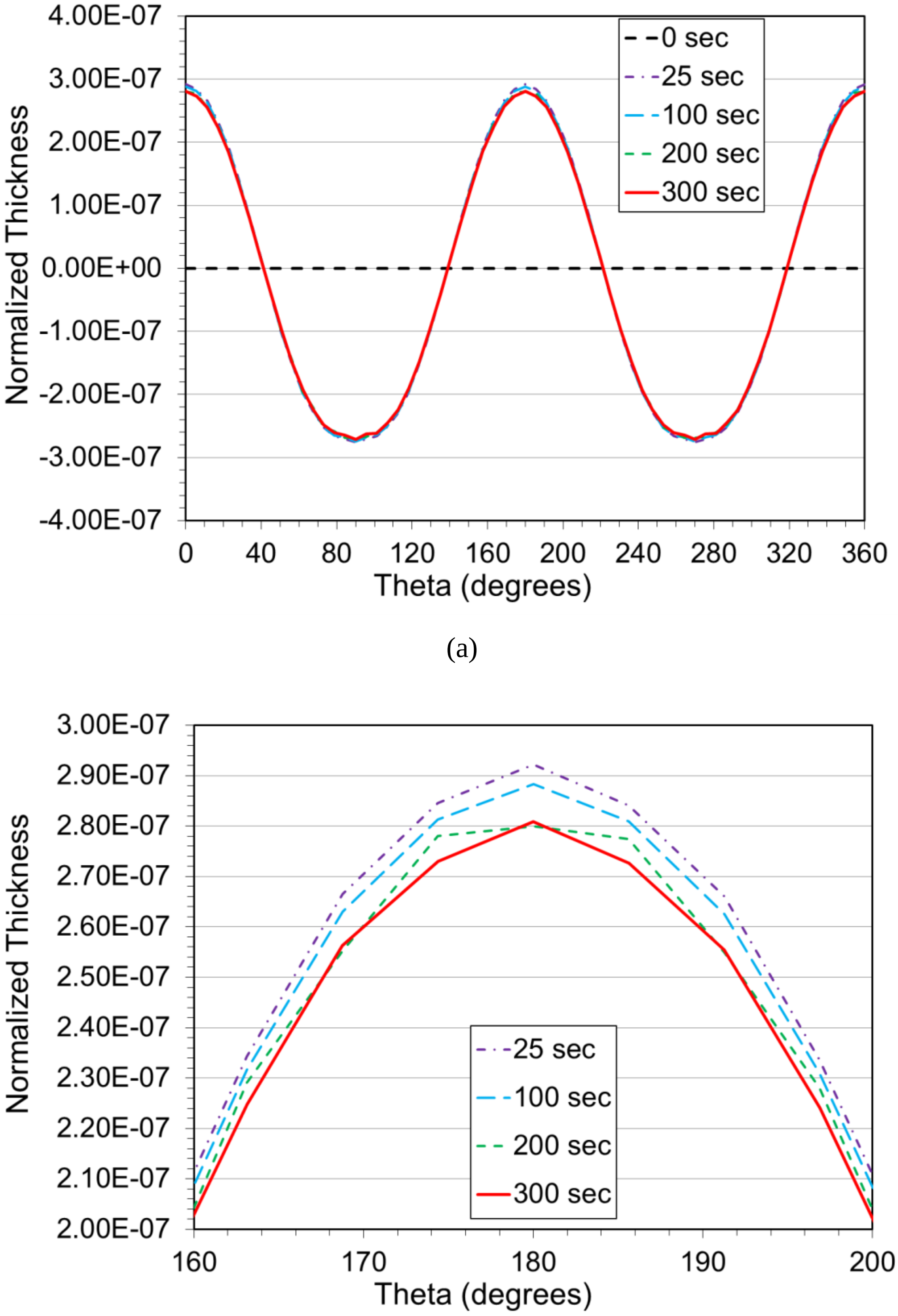

(a)

(b)

Fig. 2-11: Evolution of the normalized circumferential thickness change between (a) initiation of curing at time $t_0 = 25$ sec to time when curing is complete $t_T = 300$ sec, (b) zoomed view of the plate in the zone where applied load causes stress concentration.

Likewise, Fig. 2-12 shows that there is 8E-05 difference in the normalized radius of the circle due to the applied loading. As curing progresses, the increasing modulus of elasticity of the material results in elastic recovery under the constant tensile force. It is important to note that this recovery of the geometric configuration is a function of the mechanical strains induced by the chemical reactions.

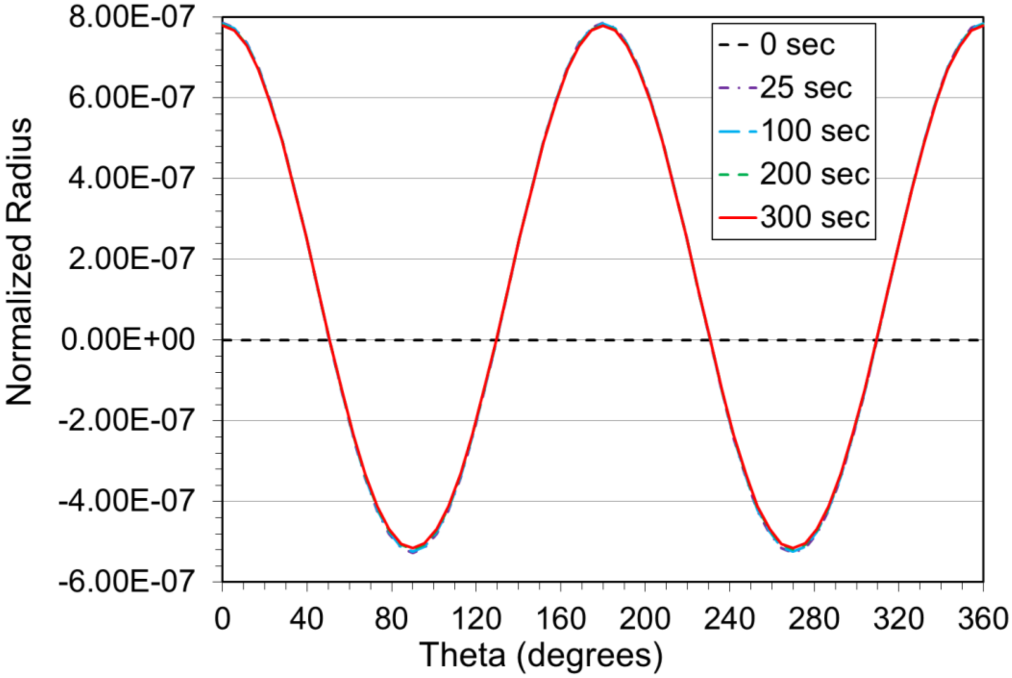

(a)

Fig. 2-12: Evolution of the normalized radius change between (a) initiation of curing at time t_0 = 25 sec to time when curing is complete t_T = 300 sec, (b) zoomed view of the plate in the zone where applied load causes stress concentration.

Fig. 2-12: (cont.)

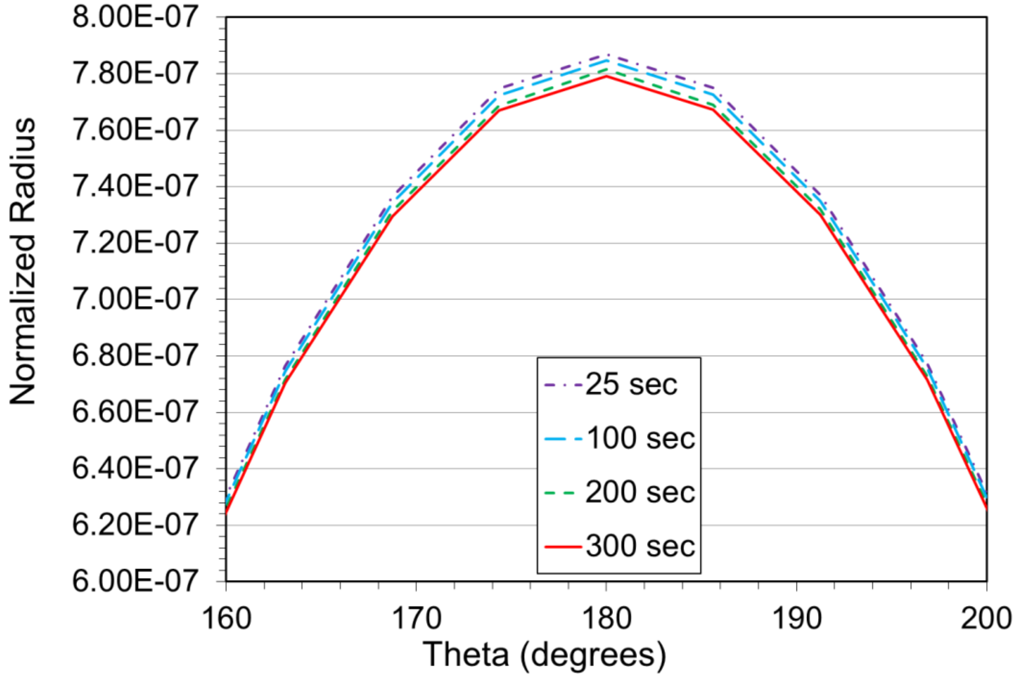

(b)

To study the performance modeling aspect due to spatial variation in the material properties after curing, an axial traction of 2 MPa is applied at $x = \pm 30$ plane. The hoop stress vs applied traction ratio along the circumference of the hole is compared with the exact solution provided in [19].

Table 2-1 Material properties of the lamina.

	λ (MPa)	α (MPa)	β (MPa)	μ_L (MPa)	μ_T (MPa)	ρ (kg/mm^3)	Volume Fraction
Fiber	1.314E+04	-3.86E+03	2.252E+05	9.674E+03	3.531E+03	1550E-09	0.7
Matrix	3.4315	-	-	2.2877	-	1200E-09	0.3

Fig. 2-13 presents the temperature profile, degree of cure and elastic modulus at 300 seconds of the cure cycle. Fig. 2-13b shows that the matrix material cures faster in the region where temperature is higher in comparison to the regions of the lamina with cooler temperatures, as shown in Figure 12a. It is assumed that the prescribed temperature field is slowly-varying and thermal conductivity is sufficiently low such that the dissipative effects of heat conduction can be neglected. Fig. 2-13c shows the elastic modulus distribution of the matrix material at 300 seconds. The matrix elastic modulus peaks at the areas corresponding to the lowest prescribed temperature field, while it has a lower elastic modulus at the fully cured regions. Though the curing rate is faster at the higher temperatures, the distribution in Fig. 2-13c is due to the fact that the fully cured matrix elastic modulus at higher temperature is lower due to thermal softening than the region where the temperature is cooler by 20 K.

Fig. 2-14a shows the evolution of curing at 50, 100, 120, 200 and 300 seconds along a line that runs tangent to the top of the hole along the length of the domain. Material regions corresponding to a higher prescribed temperature cures faster as compared to the regions of lower temperatures across the domain. Fig. 2-14b shows the evolution in the elastic modulus in the matrix material at 50, 100, 120, 200 and 300 seconds. A non-uniform distribution of the elastic modulus can be observed along the length of the domain that can be attributed to two contributing factors: (i) degree of cure, and (ii) temperature. On one hand the elastic modulus decrease with increase in temperature even for fully cured material, while on the other hand time required to achieve complete curing is longer in regions with lower temperature. These two competing mechanisms lead to spatially varying elastic modulus over the domain. The matrix axial stress shown in Figure 2-14c follows a similar trend and we see high surface stresses near the hole.

Fig. 2-15 shows the matrix axial stress profile across the domain at 300 seconds. It can be seen that the axial stress is higher in the region around the hole, where the tensile stress is 4.786 MPa for an applied normal traction of 2 MPa in the axial direction.

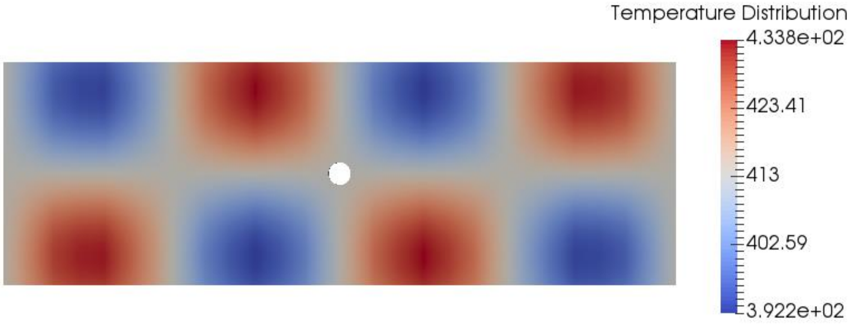

(a) Temperature profile across the domain

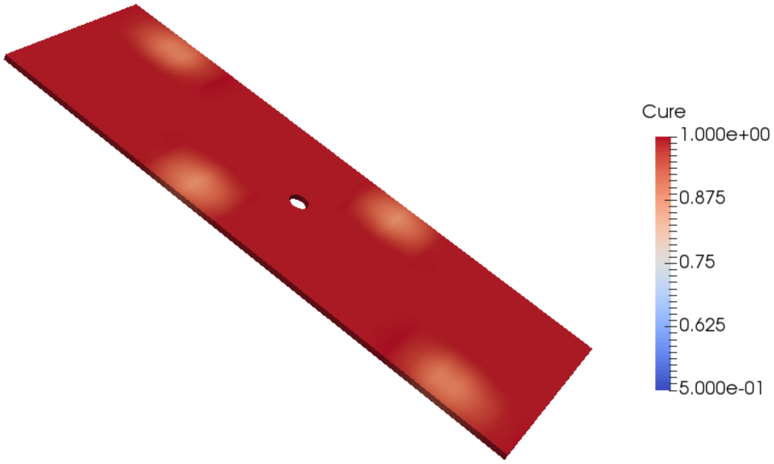

(b) Spatial distribution of the degree of cure.

Fig. 2-13: Temperature (a), cure (b), and matrix modulus (c) distribution at 300 seconds.

Fig. 2-13 (cont.)

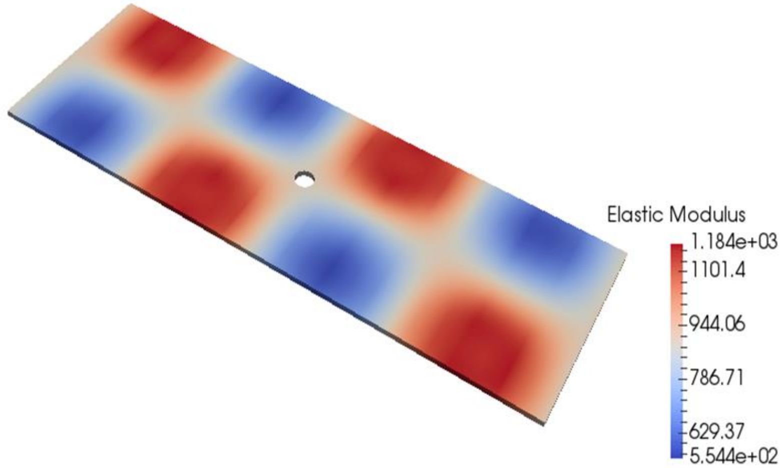

(c) Spatial distribution of modulus of the matrix constituent.

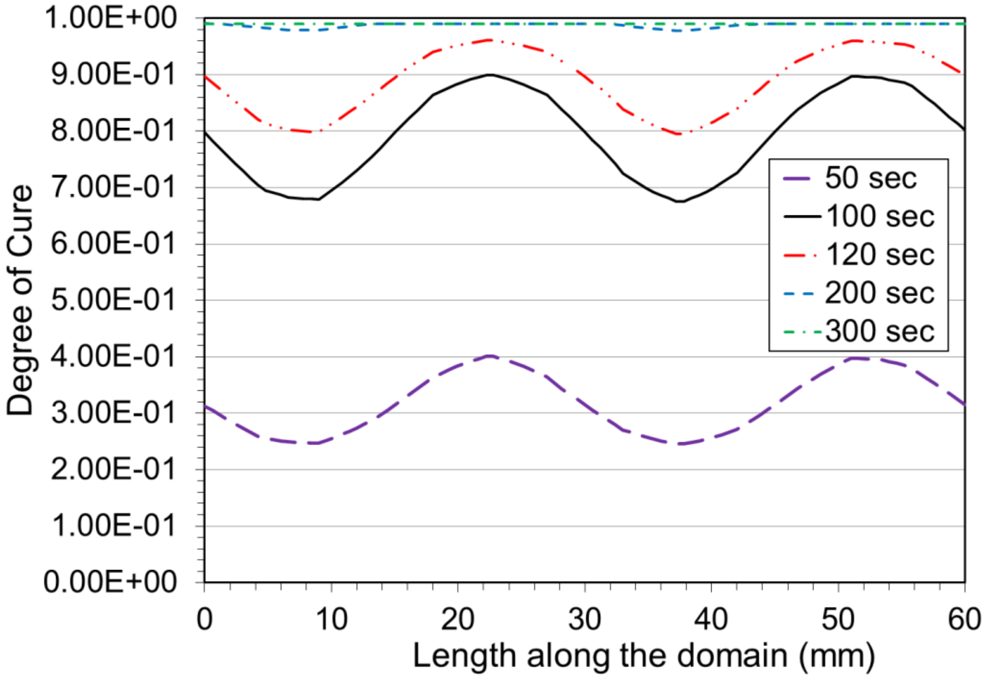

(a) Cure along the length of the domain.

Fig. 2-14: Spatial variation of cure, matrix modulus and matrix axial stress at 50, 100, 120, 200, and 300 seconds. This analysis has been taken along the domain tangent to the top of the hole.

Fig. 2-14: (cont.)

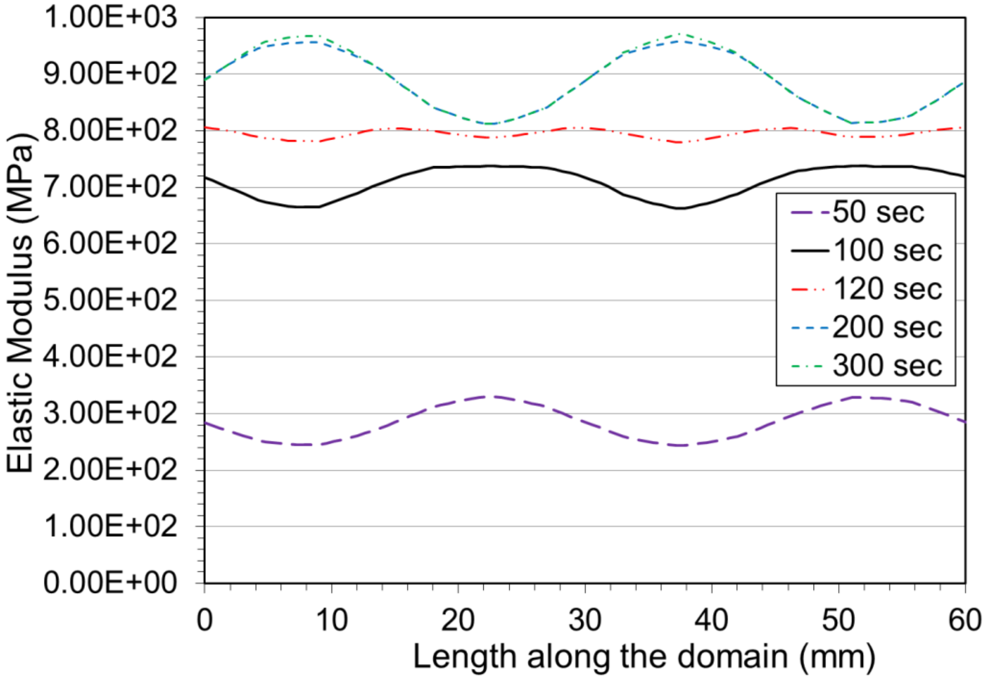

(b) Matrix elastic modulus along the domain.

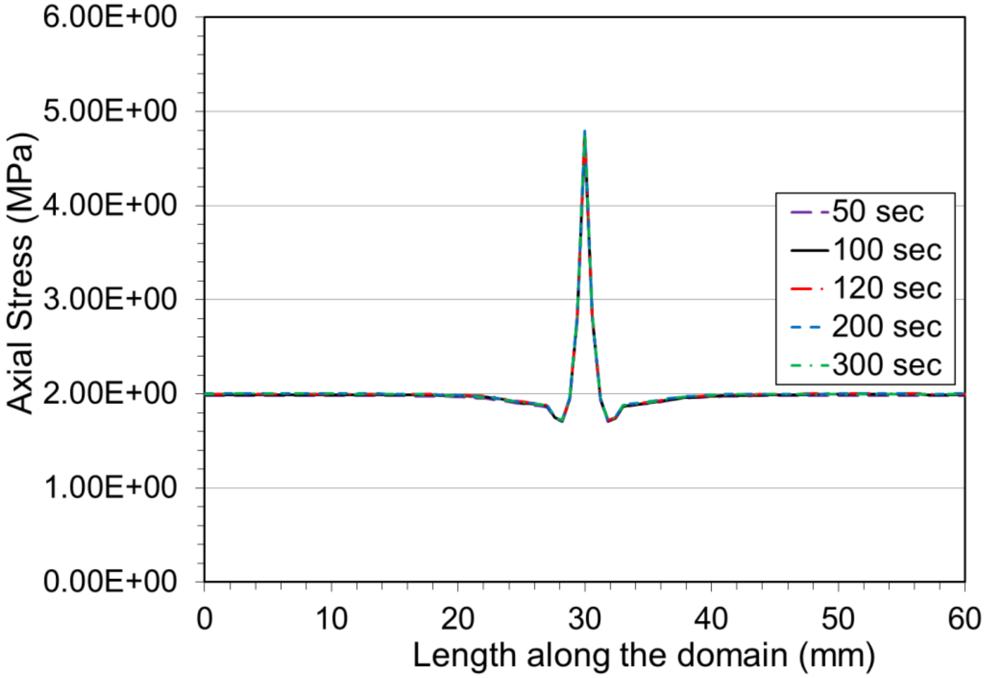

(c) Matrix Axial Stress along the length of domain.

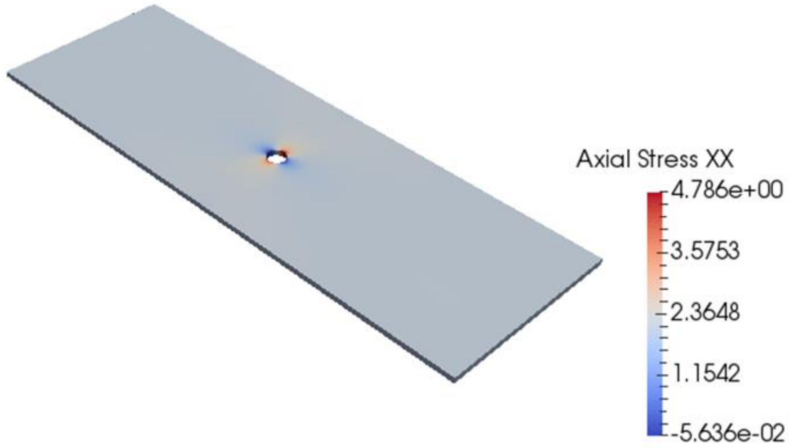

Fig. 2-15: Matrix axial stress at 300 seconds in the cure cycle.

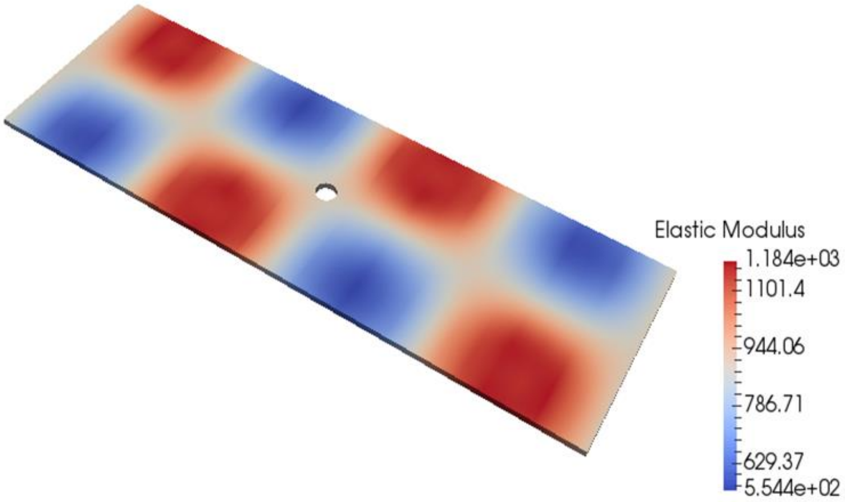

Fig. 2-16: Matrix modulus of a fully cured matrix for degree of cure = 0.99

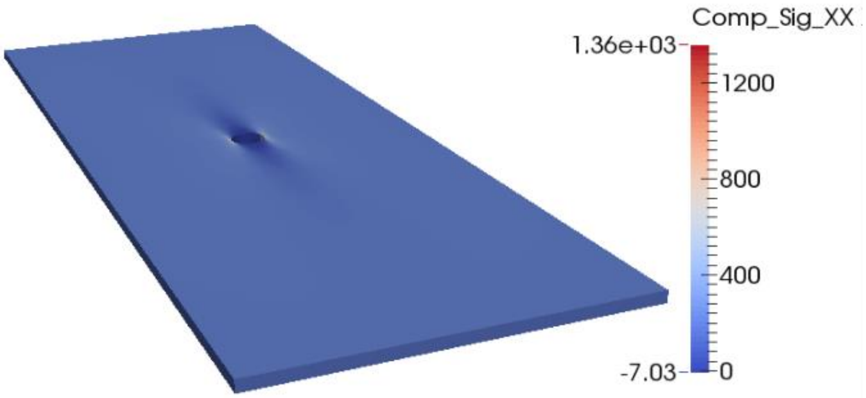

(a) Composite axial stress

Fig. 2-17: Composite axial stress of the fully cured composite at 200 MPa loading

Fig. 2-17: (cont.)

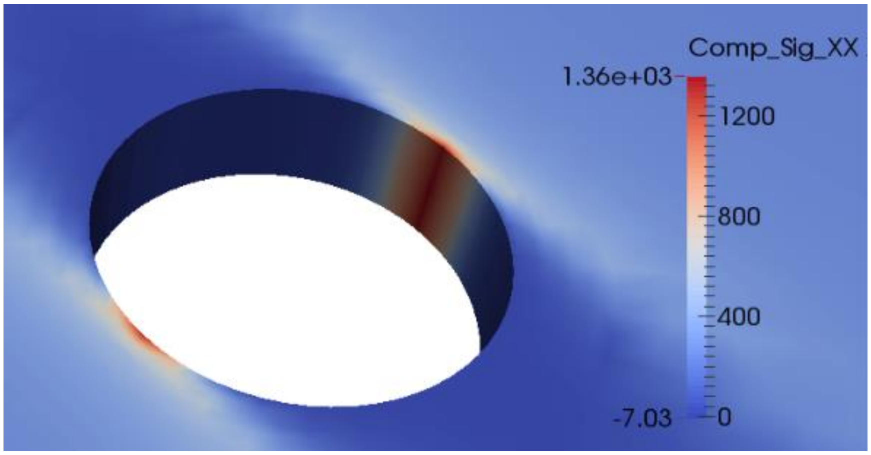

(b) Composite axial stress - zoomed view.

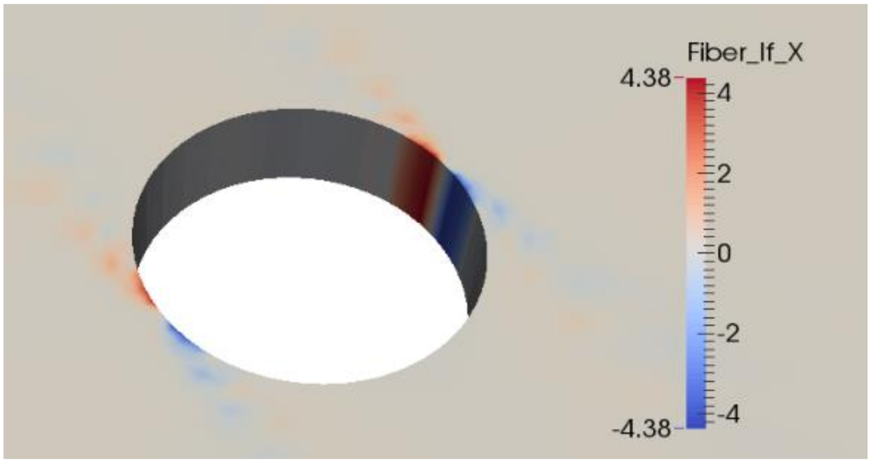

(a) Interactive force in X direction.

Fig. 2-18: Interactive force of a fully cured composite at 200 MPa loading.

Fig. 2-18: (cont.)

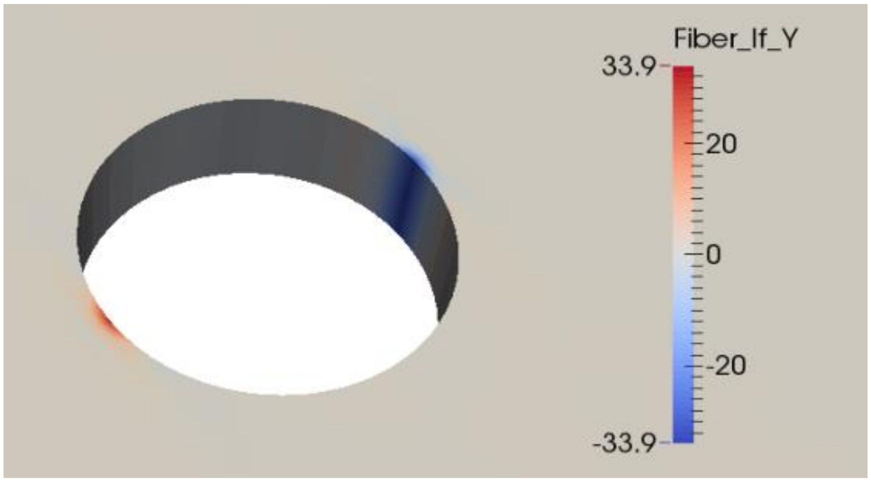

(b) Interactive force in Y direction.

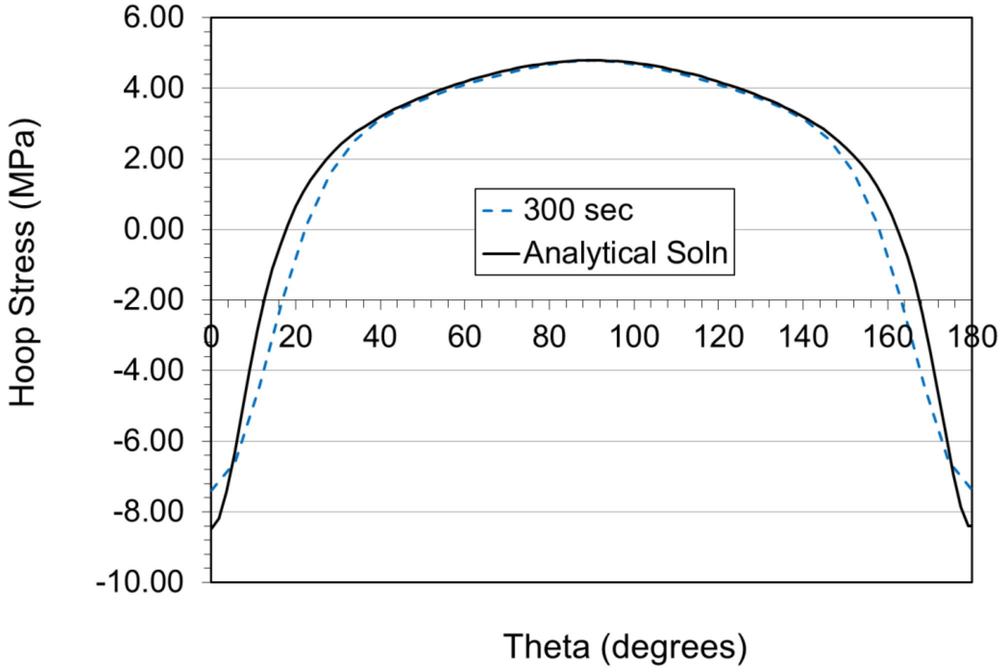

(a) Hoop stress vs applied traction.

Fig. 2-19: Variation of the hoop stress and matrix modulus along the circumference of the hole.

Fig. 2-19: (cont.)

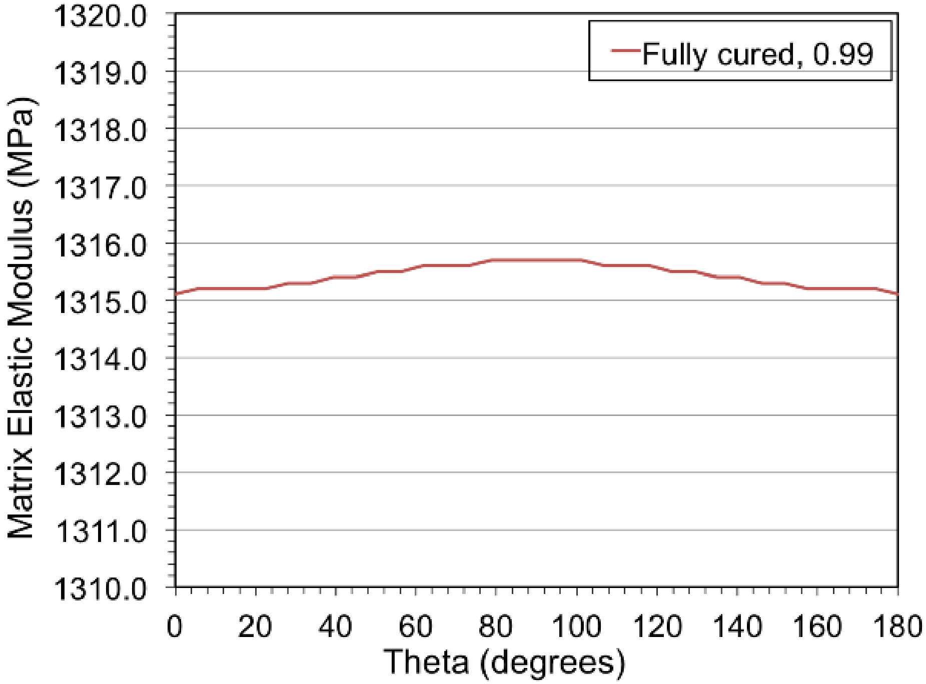

(b) Matrix elastic modulus.

Fig. 2-16 shows distribution of the matrix modulus once the matrix is nearly fully cured, where the degree of cure reaches a value of 0.99 at every spatial point in the domain. This is a representative simulation that shows the effect of curing on the distribution of the resin properties in the manufactured composite due to the imposed temperature distribution heat treatment. The fully cured composite is subjected to an axial loading of 200 MPa at $x = \pm 30$ plane. Fig. 2-17 shows the composite axial stress contour in the lamina, where the maximum axial stress of 1.36e3 MPa occurs at the point that is at 90^0 along the circumference of the hole with respect to the axial direction. Fig. 2-18a and 2-18b shows the interactive force profile in X and Y direction respectively. In the current presentation of the model, the interfaces are considered as tightly bounded and no relative slipping is allowed between the constituents at the domain boundaries. This restriction can be removed by introducing a slip-function or sliding-function that permits relative sliding between fiber and matrix and reflected via the interactive force field. The evolution equation for slip and/or debonding would get reflected in the Lagrange multiplier and when embedded in the variational equation, it will accommodate the proportioning of the applied edge tractions amongst the two constituents while accounting for the evolving damage at the edge.

Fig. 2-19a shows the distribution of the hoop stress along the circumference of the hole vs applied axial traction for fiber orientation of 0^0 degree for two cases: (i) At 300 seconds of cure cycle, where an axial traction of 2 MPa is applied, (ii) For a fully cured material, where axial traction of 200 MPa is applied. As the material model employed in this work is nonlinear elastic and as shown in Fig. 2-19b, the temperature variation along the circumference of the hole is almost constant, the hoop stress vs applied traction for both the materials overlap each other and compare well with the exact solution.

2.4.5 Addition of Gaseous Voids into the Plate with Hole

As the liquid epoxy undergoes high temperature curing in the material, gas bubbles form as heat is applied to the material. The matrix epoxy continues to harden into a gel and solid, yet some of the gas bubbles can get trapped into the new homogenous composite material. The gas bubbles weaken the Elastic modulus in the system which can cause voids and potential damage to the new mixture material. By estimating the percentage of the material that contains the gas bubble, these voids can show the deficiency of the modulus in the location of the formed voids. Using user defined locations in the same resin material as defined in Table 2-1, the material can be observed to find if the addition of these gaseous voids are critical to the failure of the material. Fig. 2-20 shows the Elastic modulus at 100, 200, 300 seconds. Notice that while the material continues to cure, the voids become more apparent. The increased awareness as the material hardens is due to the larger discrepancy between the matrix resin and the gaseous void. Fig. 2-21 shows the effects of the void through the thickness of the material.

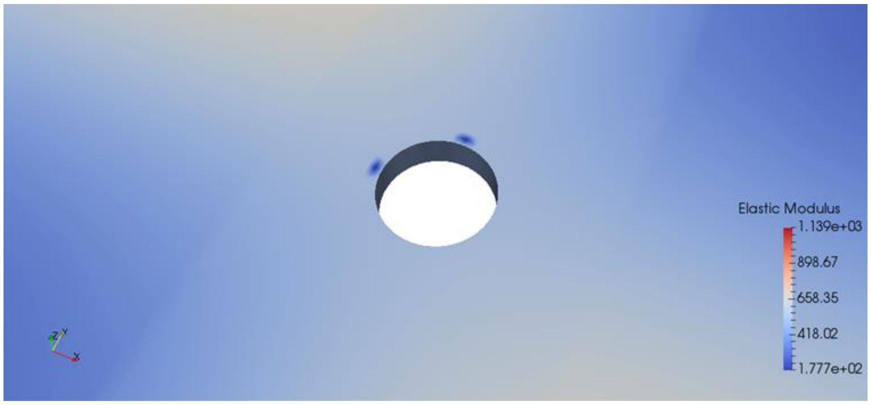

(a) Matrix Elastic modulus at 100 seconds

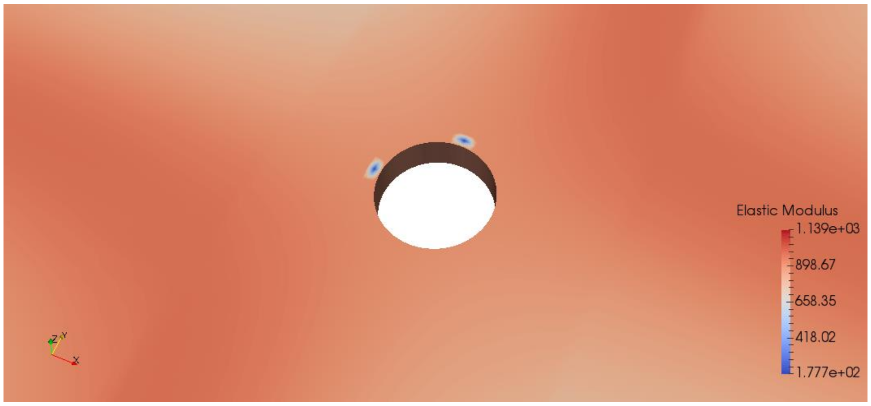

(b) Matrix Elastic modulus at 200 seconds

Fig. 2-20: Evolution of the matrix elastic modulus around the hole at 100, 200 and 300 seconds with a void along the top and the left side of the hole.

Fig. 2-20: (cont.)

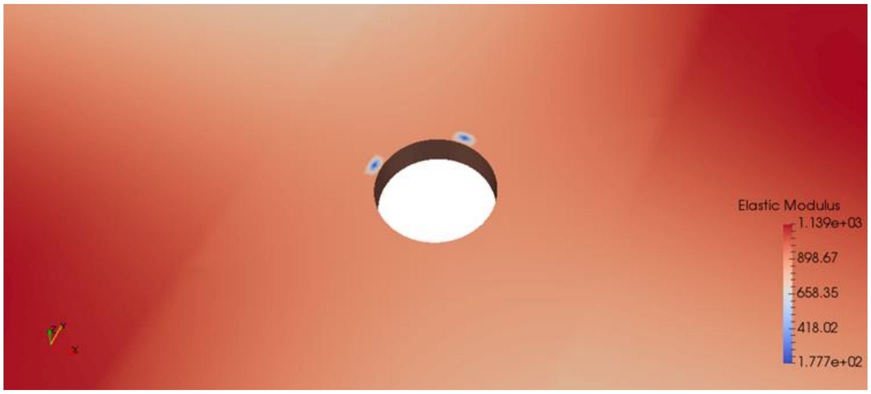

(c) Matrix Elastic modulus at 300 seconds

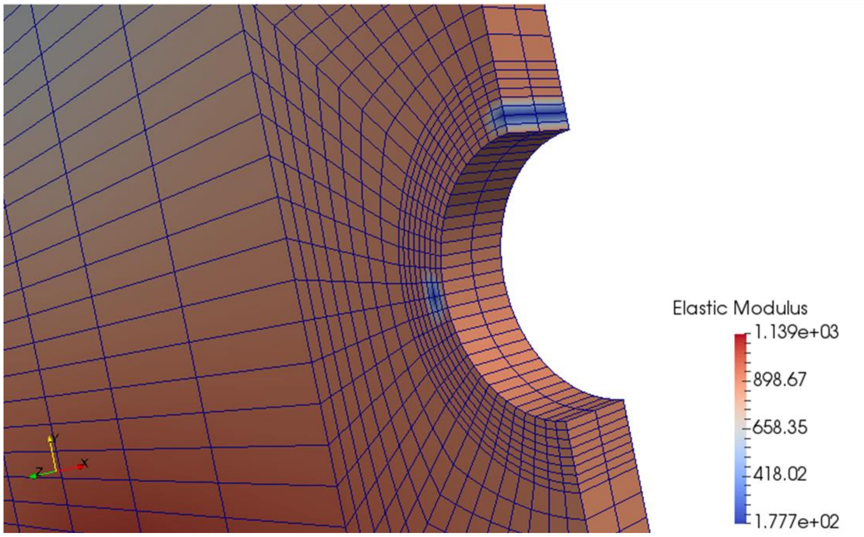

Fig. 2-21: Cross section view of the void through the thickness of the plate. The Plate has been cut along the x=0 plane.

Fig. 2-22 shows the plot of the elastic modulus around the hole. The plot identifies the voids through spikes of lower modulus values at 90 and 180 degrees where the voids are located. Here the void at 90 degrees would be detrimental to the infrastructure of the plate since it occurs in the area of high composite axial stress as shown in Fig. 2-17 while the void at 180 degrees is less crucial to the integrity of the system.

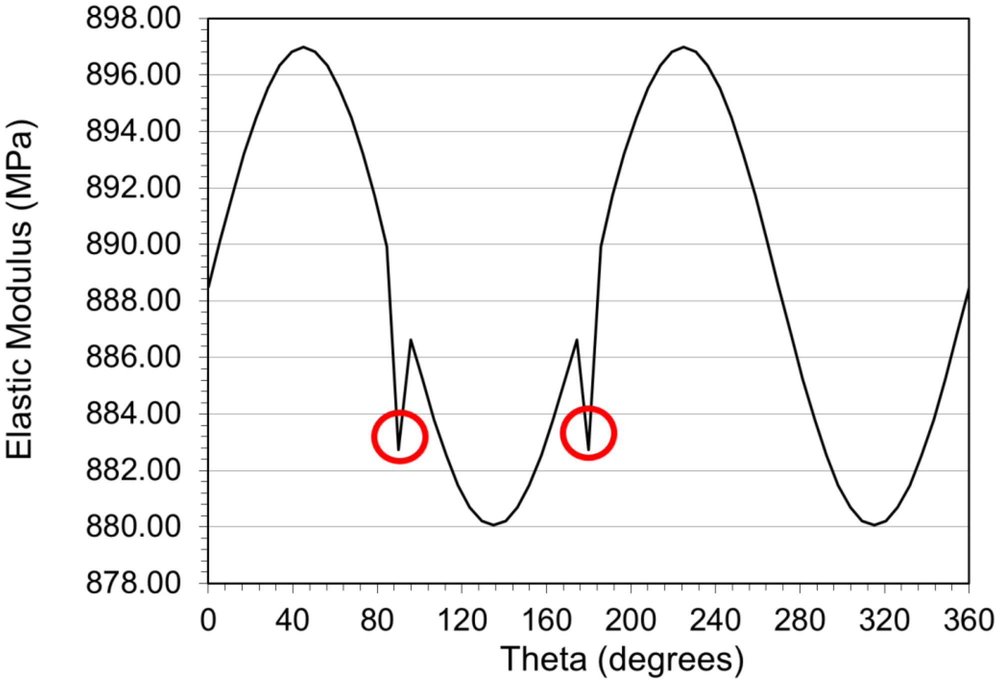

Fig. 2-22: The Elastic modulus around the hole after 300 seconds of curing. The locations of the voids are identified and circled in red.

CHAPTER 3: FINITE STRAIN INTERFACE STABILIZATION FOR DISCONTINUITIES IN MULTI-CONSTITUENT MATERIALS

This chapter presents an interesting class of test problems that have been carried out with a computer code developed in Chen et al [7]. The theoretical foundations of the method presented in Truster et al [49] lie in finite deformation elasticity and a merger of DG finite element methods with CG methods. The synopsis of Chen et al [7] is as follows.

3.1 GOVERNING EQUATIONS AND MIXED INTERFACIAL WEAK FORM

As stated in [7], the reference configuration and the deformed configuration of the two domains connecting together with interfaces Γ_{I} is shown in Fig. 3-1. At interfaces, the two domains can develop interfacial gaps. As stated in [7], an open bounded region $\Omega \subset \mathbb{R}^{n_{sd}}$ consist of two disjoint regions $\Omega^{(1)}$ and $\Omega^{(2)}$ by an interface Γ_{I} as shown in Fig. 3-1. The two bodies deform according to the motion $\boldsymbol{\phi}^{(\alpha)}\left(\boldsymbol{X},t\right)$ that maps the reference configuration onto the current configuration, $\boldsymbol{x}=\boldsymbol{\phi}^{(\alpha)}\left(\boldsymbol{X},t\right)$ where α represents different domains as 1 and 2.

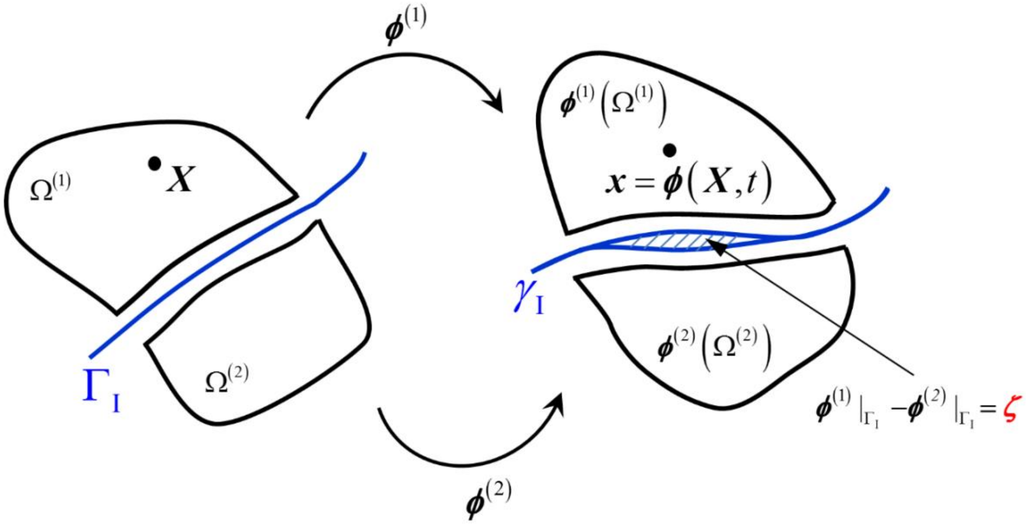

(a) (b)

Fig. 3-1: Domain Ω with interface Γ_{I} [7]. The deformed configurations are given by $\boldsymbol{\phi}^{(1)}$ and $\boldsymbol{\phi}^{(2)}$: (a) Reference configuration; (b) Current configuration.

The equilibrium equations with the existence of the Lagrange multiplier field and the interface gap or debonding are given as follows.

$$\mathrm{DIV}\ \boldsymbol{P}^{(\alpha)}\left(\boldsymbol{F}^{(\alpha)}\right)+\rho_o^{(\alpha)}\boldsymbol{B}^{(\alpha)}=\boldsymbol{0} \qquad \text{in} \quad \Omega^{(\alpha)},\ \alpha=1,2 \tag{3.1}$$

$$\boldsymbol{\phi}^{(\alpha)}=\boldsymbol{X}^{(\alpha)} \qquad \text{on}\ \Gamma^{(\alpha)}\setminus\Gamma_{\mathrm{I}},\ \alpha=1,2 \tag{3.2}$$

$$\boldsymbol{\phi}^{(1)}-\boldsymbol{\phi}^{(2)}=\boldsymbol{\zeta} \qquad \text{on}\ \Gamma_{\mathrm{I}} \tag{3.3}$$

$$\boldsymbol{\lambda}-\boldsymbol{P}^{(1)}\cdot\boldsymbol{N}^{(1)}=\boldsymbol{0} \qquad \text{on}\ \Gamma_{\mathrm{I}} \tag{3.4}$$

$$-\boldsymbol{P}^{(2)}\cdot\boldsymbol{N}^{(2)}-\boldsymbol{\lambda}=\boldsymbol{0} \qquad \text{on}\ \Gamma_{\mathrm{I}} \tag{3.5}$$

. In (3.1) to (3.5), $\boldsymbol{P}^{(\alpha)}$ is the first Piola-Kirchhoff stress tensor, $\rho_o^{(\alpha)}$ is the mass density, $\boldsymbol{B}^{(\alpha)}$ is the body force vector, , $\boldsymbol{\phi}^{(\alpha)}$ is the deformation map form either domain 1 or domain 2 and $\boldsymbol{N}^{(\alpha)}$ is the unit outward normal vector at the region boundary Γ_{I}. The Lagrange multiplier λ is introduced to enforce the equilibrium of tractions (3.4) –(3.5).

Multiplying equilibrium equations (3.1) to (3.5) by weighting function $\boldsymbol{\eta}_o^{(\alpha)}$ and applying the divergence theorem, the associated weak form is expressed as follows: Find $\left\{\boldsymbol{\phi}^{(1)},\boldsymbol{\phi}^{(2)},\boldsymbol{\lambda}\right\}\in\mathcal{S}^{(1)}\times\mathcal{S}^{(2)}\times\mathcal{Q}$ such that for all $\left\{\boldsymbol{\eta}_o^{(1)},\boldsymbol{\eta}_o^{(2)},\mu\right\}\in\mathcal{V}^{(1)}\times\mathcal{V}^{(2)}\times\mathcal{Q}$:

$$\sum_{\alpha=1}^{2}\int_{\Omega^{(\alpha)}}\mathrm{GRAD}\,\boldsymbol{\eta}_o^{(\alpha)}:\boldsymbol{P}^{(\alpha)}\,\mathrm{d}V-\sum_{\alpha=1}^{2}\int_{\Omega^{(\alpha)}}\rho_o^{(\alpha)}\boldsymbol{B}^{(\alpha)}\cdot\boldsymbol{\eta}_o^{(\alpha)}\,\mathrm{d}V-\int_{\Gamma_{\mathrm{I}}}\boldsymbol{\lambda}\cdot\ \ \boldsymbol{\eta}_o\ \ \mathrm{d}A=0 \tag{3.6}$$

$$-\int_{\Gamma_{\mathrm{I}}}\boldsymbol{\mu}\cdot\left(\ \ \boldsymbol{\phi}\ \ -\boldsymbol{\zeta}\right)\mathrm{d}A=0 \tag{3.7}$$

As stated in [7], eqn. (3.7) weakly enforces the jump continuity where $\ \bullet\ =\left(\bullet\right)^{(1)}-\left(\bullet\right)^{(2)}$ is the jump operator defined at interface Γ_{I}. The appropriate function spaces contained in the weak forms (3.6) and (3.7) are given as in [7]:

$$\mathcal{S}^{(\alpha)}=\left\{\boldsymbol{\phi}^{(\alpha)}\middle|\boldsymbol{\phi}^{(\alpha)}\in\left[H^1\left(\Omega^{(\alpha)}\right)\right]^{n_{\mathrm{sd}}},\ \det\left(\boldsymbol{F}^{(\alpha)}\left(\boldsymbol{\phi}^{(\alpha)}\right)\right)>0,\ \ \boldsymbol{\phi}^{(\alpha)}\Big|_{\Gamma^{(\alpha)}\setminus\Gamma_{\mathrm{I}}}=\boldsymbol{X}^{(\alpha)}\right\} \tag{3.8}$$

$$\mathcal{V}^{(\alpha)}=\left\{\boldsymbol{\eta}_o^{(\alpha)}\middle|\boldsymbol{\eta}_o^{(\alpha)}\in\left[H_o^1\left(\Omega^{(\alpha)}\right)\right]^{n_{\mathrm{sd}}},\ \ \boldsymbol{\eta}_o^{(\alpha)}\Big|_{\Gamma^{(\alpha)}\setminus\Gamma_{\mathrm{I}}}=\mathbf{0}\right\} \tag{3.9}$$

$$\mathcal{Q}=\left\{\boldsymbol{\lambda}\middle|\boldsymbol{\lambda}\in\left[H^{-\frac{1}{2}}\left(\Gamma_{\mathrm{I}}\right)\right]^{n_{\mathrm{sd}}}\right\} \tag{3.10}$$

Using the VMS method, the stabilized interface formulation and the corresponding linearization are derived in [7] and summarized below.

$$\begin{aligned} R\left(\boldsymbol{\eta}_o^{(\alpha)},\boldsymbol{\phi}^{(\alpha)}\right) &= \sum_{\alpha=1}^{2}\int_{\Omega^{(\alpha)}}\left[\mathrm{GRAD}\,\boldsymbol{\eta}_o^{(\alpha)}:\boldsymbol{P}^{(\alpha)}-\boldsymbol{\eta}_o^{(\alpha)}\cdot\rho_o^{(\alpha)}\boldsymbol{B}^{(\alpha)}\right]\mathrm{d}V \\ &-\int_{\Gamma_I}\boldsymbol{\eta}_o\cdot\left\{\boldsymbol{P}\cdot\boldsymbol{N}\right\}\mathrm{d}A-\int_{\Gamma_I}\left\{\left(\mathrm{GRAD}\,\boldsymbol{\eta}_o:\mathbf{A}\right)\cdot\boldsymbol{N}\right\}\cdot\left(\boldsymbol{\phi}-\boldsymbol{\zeta}\right)\mathrm{d}A \\ &+\int_{\Gamma_I}\boldsymbol{\eta}_o\cdot\boldsymbol{\tau}_s\cdot\left(\boldsymbol{\phi}-\boldsymbol{\zeta}\right)\mathrm{d}A=0 \end{aligned} \tag{3.11}$$

$$\begin{aligned} K\left(\boldsymbol{\eta}_o^{(\alpha)},\Delta\boldsymbol{u}^{(\alpha)};\boldsymbol{\phi}^{(\alpha)}\right) &= \sum_{\alpha=1}^{2}\int_{\Omega^{(\alpha)}}\mathrm{GRAD}\,\boldsymbol{\eta}_o^{(\alpha)}:\mathbf{A}^{(\alpha)}:\mathrm{GRAD}\,\Delta\boldsymbol{u}^{(\alpha)}\,\mathrm{d}V \\ &+\int_{\Gamma_\mathrm{I}}\boldsymbol{\eta}_o\cdot\boldsymbol{\tau}_s\cdot\Delta\boldsymbol{u}\,\mathrm{d}A-\int_{\Gamma_I}\boldsymbol{\eta}_o\cdot\left\{\left(\mathbf{A}:\mathrm{GRAD}\,\Delta\boldsymbol{u}\right)\cdot\boldsymbol{N}\right\}\mathrm{d}A \\ &-\int_{\Gamma_\mathrm{I}}\left\{\left(\mathrm{GRAD}\,\boldsymbol{\eta}_o:\mathbf{A}\right)\cdot\boldsymbol{N}\right\}\cdot\Delta\boldsymbol{u}\,\mathrm{d}A \\ &-\int_{\Gamma_\mathrm{I}}\left\{\left(\mathrm{GRAD}\,\boldsymbol{\eta}_o:\boldsymbol{\Xi}:\mathrm{GRAD}\,\Delta\boldsymbol{u}\right)\cdot\boldsymbol{N}\right\}\cdot\left(\left[\left(\boldsymbol{\phi}-\boldsymbol{\zeta}_n\right)-\Delta\gamma\boldsymbol{n}\right]\right)\mathrm{d}A \\ &+\int_{\Gamma_\mathrm{I}}\tilde{\boldsymbol{T}}\left(\boldsymbol{\eta}_o\right)\cdot\left[\frac{\partial}{\partial\boldsymbol{T}}\left(\Delta\gamma\boldsymbol{n}\right)\cdot\tilde{\boldsymbol{T}}\left(\Delta\boldsymbol{u}\right)\right]dA \end{aligned} \tag{3.12}$$

3.2 INTERFACIAL CONSTITUTIVE MODELS AND CORRESPONDING RETURN MAPPING ALGORITHMS

In the finite element implementation of constitutive models that are based on internal variable formulism, the stabilized formulations are derived in [7]. To model the debonding of laminated composites, the evolution of inelastic gap or debonding terms need to be accommodated. The constitutive model is considered local and therefore enforced pointwise. The yield condition, damage evolution flow rule, and consistency condition at the Gauss points are strongly enforced along the interface. The residual gap $\boldsymbol{\zeta}$ and hardening variable Q are treated as internal variables. In order to track the evolution of these internal variables, the return mapping algorithm which is adopted from Simo and Hughes [47] is developed in [7]. Details of the return mapping algorithm as well as the yield functions for the case of tension are described below. Further details can be seen in Chen et al [7].

3.2.1 The Tension Model

The yield criterion in tension is defined via the following isotropic linear softening model:

$$f\left(\boldsymbol{T},Q\right)=\left\|\boldsymbol{T}\right\|-\left(P_c-Q\right) \tag{3.13}$$

where P_c is the critical stress at which debonding initiates, and Q is the softening stress. The relation between the tensile stress and the inelastic gap is shown in Fig. 3-2. The interfacial traction $\boldsymbol{T}$ is as follows:

$$\boldsymbol{T}:=\left\{\boldsymbol{PN}\right\}+\left\|\boldsymbol{\tau}^s\right\|\left(\ \boldsymbol{\phi}\ -\zeta\right) \tag{3.14}$$

The flow rule and hardening law under the assumption of isotropy are derived as follows:

$$\dot{\boldsymbol{\zeta}}=\dot{\gamma}\underbrace{\left(\partial f/\partial\boldsymbol{T}\right)}_{\text{Normality}}, \qquad \dot{Q}=H_c\,\dot{\gamma} \tag{3.15}$$

where the normality condition $\partial f/\partial\boldsymbol{T}=\boldsymbol{n}=\boldsymbol{T}/\left\|\boldsymbol{T}\right\|$ defines the unit vector in the direction of the interface traction, $H_c:=P_c/\zeta_c$ is the negative slope of the softening curve shown in Fig. 3-2, and ζ_c is the critical residual gap. The update formula for the hardening or softening parameter Q under the interface damage flow rule and the debonding gap can be shown under the following equations:

$$\boldsymbol{\zeta}_{n+1}=\boldsymbol{\zeta}_n+\Delta\gamma\partial_{\boldsymbol{T}}f_{n+1} \tag{3.16}$$

$$\boldsymbol{Q}_{n+1}=\boldsymbol{Q}_n+\mathbf{D}\Delta\gamma\,\partial_Q f_{n+1} \tag{3.17}$$

By combining the yield function f with the Kuhn-Tucker form, the current formulation results in the constitutive framework [52].

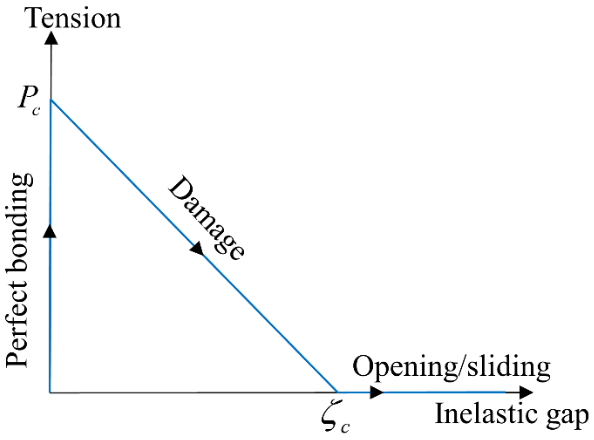

Fig. 3-2: Constitutive behavior in tension [7].

3.2.2 Return Mapping for Damage under Tensile Loading

To develop the return mapping algorithm, one needs to focus at a Gauss point along the interface Γ_{int}. The previous converged state variables are defined as $(\boldsymbol{\phi}_n, \zeta_n, Q_n)$. In order to compute the variables $\boldsymbol{\zeta}_{n+1}$ and Q_{n+1} such that the damage yield criterion is satisfied, the return mapping algorithm is developed in [7] and presented in this thesis for completion. . The interface traction can be employed by plugging in the interface damage flow rule (3.16) as:

$$\boldsymbol{T} = \{\boldsymbol{PN}\} + \left\|\boldsymbol{\tau}^s\right\|\left(\ \boldsymbol{\phi}\ -\zeta_{n+1}\right) = \{\boldsymbol{PN}\} + \left\|\boldsymbol{\tau}^s\right\|\left(\ \boldsymbol{\phi}\ -\zeta_n\right) - \left\|\boldsymbol{\tau}^s\right\|\Delta\gamma\,\partial_{\boldsymbol{T}} f_{n+1} \tag{3.18}$$

From the flow rule evaluated at time t_{n+1} we have:

$$\partial_{\boldsymbol{T}} f_{n+1} = \frac{\partial\left\|\boldsymbol{T}_{n+1}\right\|}{\partial \boldsymbol{T}_{n+1}} = \frac{\boldsymbol{T}_{n+1}}{\left\|\boldsymbol{T}_{n+1}\right\|} = \boldsymbol{n}_{n+1} \tag{3.19}$$

Substituting into (3.16), we make the following observations on the magnitude and direction of the trial and resultant interface tractions:

$$\left\|\boldsymbol{T}_{n+1}\right\| = \left\|\boldsymbol{T}^{tr}_{n+1}\right\| - \left\|\boldsymbol{\tau}^s\right\|\Delta\gamma \tag{3.20}$$

where $\boldsymbol{T}^{tr}_{n+1} = \{\boldsymbol{PN}\} + \|\boldsymbol{\tau}^{s}\|(\boldsymbol{\phi} - \boldsymbol{\zeta}_n)$ is based on the last converged value of the gap function. Further details of the model are presented in Box 3.1 below, and interested reader is directed to Chen et al [7] for mathematical derivations.

Box 3-1: Return mapping algorithm for damage evolution under tensile loading [7].

```
• STEP 1: Database at $\boldsymbol{x}^{\text{int}} \in \mathcal{B}: \{\zeta_n, Q_n\}$.
• STEP 2: Given the stress and displacement jump at $\boldsymbol{x}^{\text{int}} \in \mathcal{B}: \{\{\boldsymbol{PN}\},\ \boldsymbol{\phi}\}$
• STEP 3: Compute the trial stress and test for inelastic damage evolution
      $\boldsymbol{T}^{tr}_{n+1} = \{\boldsymbol{PN}\} + \|\boldsymbol{\tau}^{s}\|(\boldsymbol{\phi} - \boldsymbol{\zeta}_n)$        (3.21)
      $f^{tr}_{n+1} = \|\boldsymbol{T}^{tr}_{n+1}\| - (P_c - Q_n)$        (3.22)
    IF $f^{tr}_{n+1} \leq 0$ THEN
        Elastic step: Set $(\bullet)_{n+1} = (\bullet)^{tr}_{n+1}$ & EXIT
    ELSE
        Damage evolution step: Proceed to STEP 4.
    ENDIF
• STEP 4: Return mapping
      $\Delta\gamma = \dfrac{f^{\text{tr}}_{n+1}}{(\|\boldsymbol{\tau}^{s}\| - H_c)} > 0$        (3.23)
      $\boldsymbol{\zeta}_{n+1} = \boldsymbol{\zeta}_n + \Delta\gamma \boldsymbol{n}_{n+1}$        (3.24)
      $Q_{n+1} = Q_n + H_c \Delta\gamma \partial_Q f_{n+1}$        (3.25)
      $\boldsymbol{T}_{n+1} = \boldsymbol{T}^{tr}_{n+1} - \|\boldsymbol{\tau}^{s}\| \Delta\gamma \boldsymbol{n}_{n+1}$        (3.26)
```

3.3 NUMERICAL RESULTS

3.3.1 Strain Density function for neo-Hookean material

This section investigates the performance of the proposed interface method across a range of deformation modes. We have employed standard linear Lagrange polynomials and three-dimensional test problems are considered. A common neo-Hookean material model is employed, and the strain energy density function is given as follows:

$$W(\boldsymbol{F}) = \frac{1}{2}\mu\left(\mathrm{tr}\left(\boldsymbol{F}^T\boldsymbol{F}\right)-3\right)-\mu\ln J+\frac{1}{2}\lambda(J-1)^2 \tag{3.27}$$

Simulations with simple Neo-Hookean materials and anisotropic materials are presented in the following sections. Composite laminates and particle inclusions are tested and compared with the literature for stress and displacement field and further debonding is simulated.

3.3.2 Damage inflicted on a Simple Neo-Hookean 3D Bar

The first test case consists of a 3D bar that has 2x2x20 elements with each element being a 1x1x1 cube. The standard Neo-Hookean material has an Elastic modulus of 5,000 MPa and a Poisson's ratio of 0.25. The left end corresponding to x=0 is fixed in the x, y, and z directions. The right end, which corresponds to x=20, has a positive z-displacement boundary condition along the top edge while there is a negative z-displacement boundary condition along the bottom edge. As the displacement increases, damage will begin to occur once the interface tractions reach a stress value of 100 MPa with δ_c =2mm as marked out in Fig. 3-2. After each load step, an additional 1% of the material thickness is displaced in the vertical direction at the right end of the bar. Fig. 3-3 shows the deformation of the delamination on the bar after 50, 100, 150, and 200 load steps to show the large deformation experienced after damage. The axial stress in the z direction shows that the laminar material tries to remain cohesive until the applied displacement causes a force in the applied direction away from the interface. Fig. 3-4 compares the applied displacement to the length of the delamination along the axial direction of the bar. After each element experiences delamination, the amount of applied displacement along the right end is recorded to see the trend. As shown in Fig. 3-4, each addition delaminated element requires increased displacement to show a nonlinear trend for delamination.

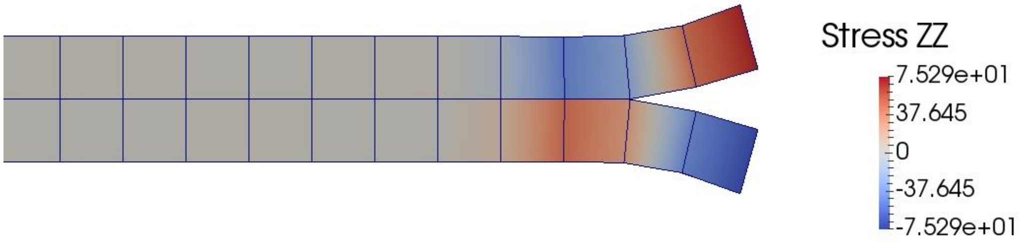

(a) Step 50

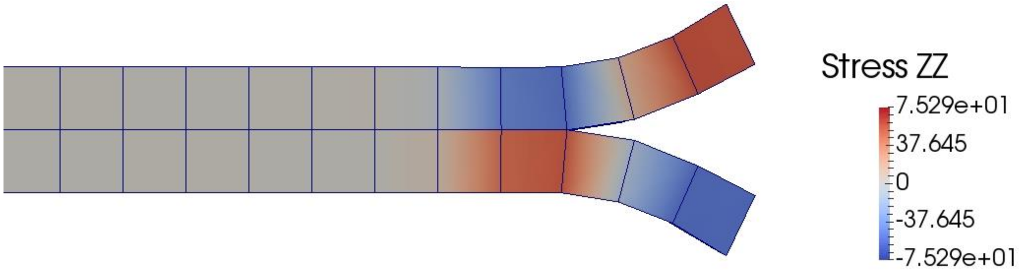

(b) Step 100

Fig. 3-3: The transverse axial stress for the 3D bar showing the deformation of the material after (a) 1mm, (b) 2mm, (c) 3mm, and (d) 4mm displacement in the vertical direction along the right end of the bar.

Fig. 3-3: (cont.)

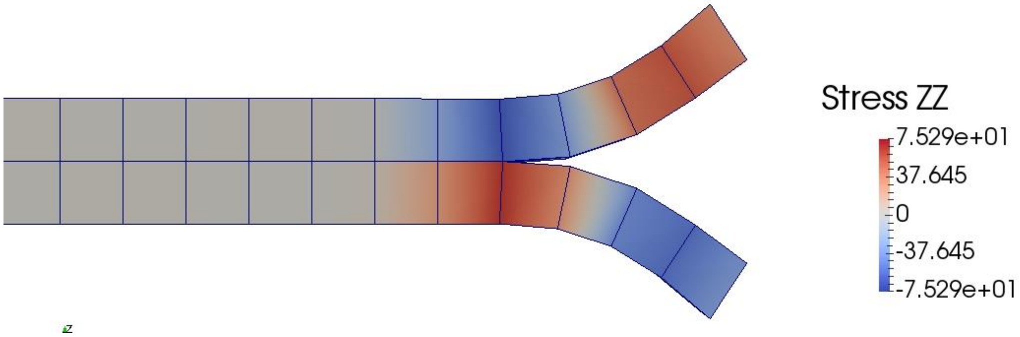

(c) Step 150

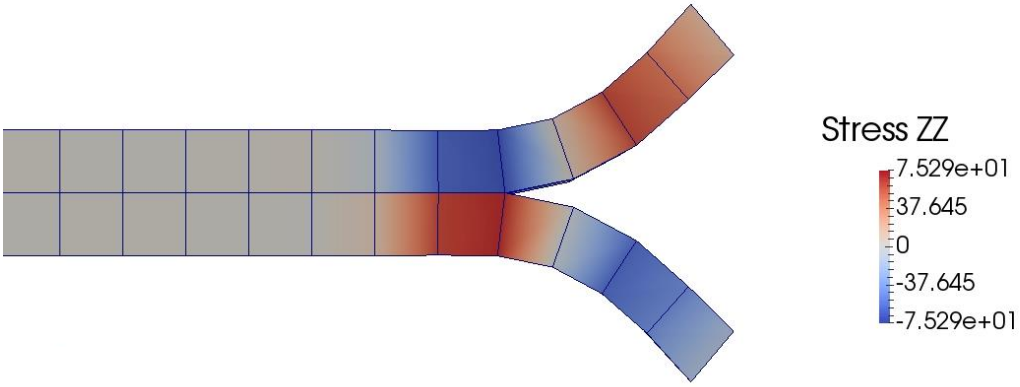

(d) Step 200

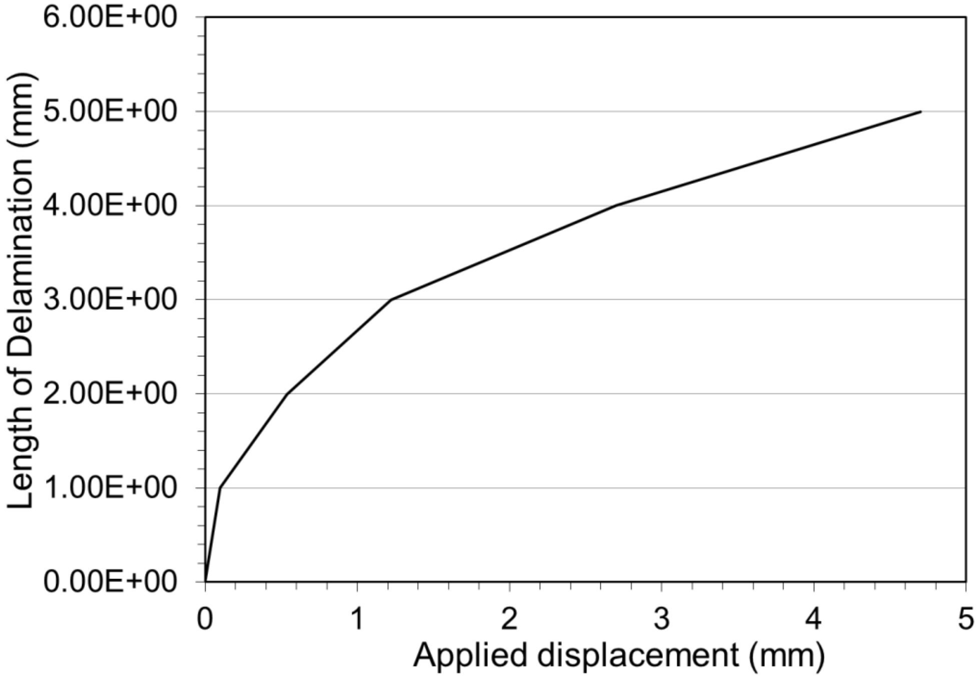

Fig. 3-4: The applied displacement for the resultant length of delamination of the 3D bar.

To show the ability for the damage model to endure extreme amounts of shear and rotations, the next problem takes the same 3D bar, but applies rotational displacement boundary conditions on the nodes along the free end of the Bar to induce large torsion on the bar. For this case, damage is initiated once the interface tractions reach a stress value of 500 MPa with the same δ_c =2mm to allow for large rotation before the frictional damage model takes effect. As shown in the deformed configuration in Fig. 3-5, the 3D bar undergoes 270° rotation (3 quarter turns) to show the evolution of the shear stress throughout the length of the bar. The damage appears to take place along the interface closest to the fixed end of the bar due to the rapid change in the shear stress along the YZ plane which lands parallel to the applied rotation. Since the primary damage occurs along this interface, Fig. 3-6 shows the inside interfaces for the left and right surfaces for the interface that is undergoing damage. Notice how the magnitudes and direction of these two sets of stress are different to cause large damage to occur.

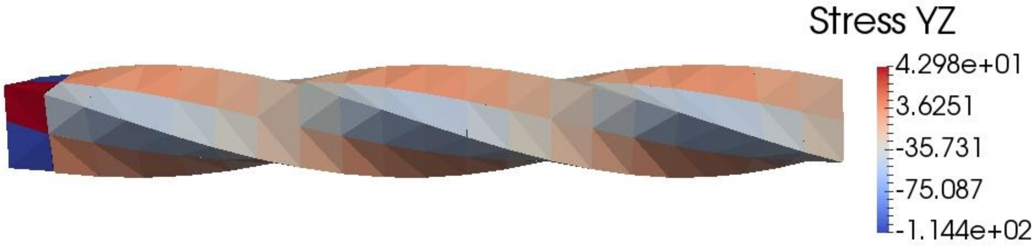

(a)

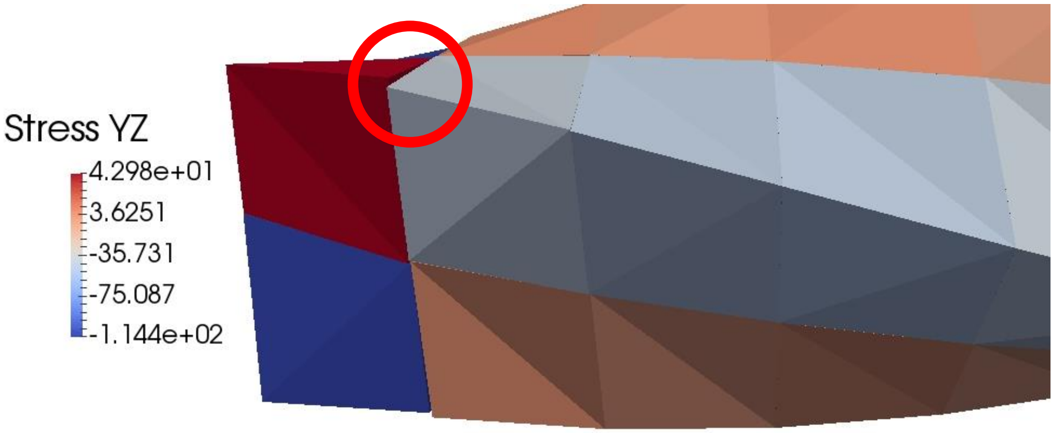

(b)

Fig. 3-5: The shear stress parallel to the axis of rotation. (a) shows the entire bar while (b) is a zoomed view at the damaged elements near the fixed end. The circle highlights the location where damage is initiated.

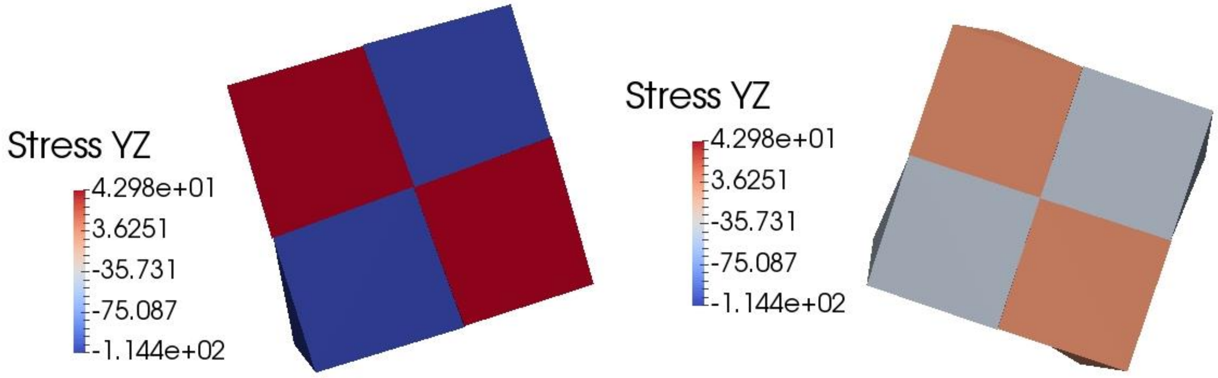

(a) (b)

Fig. 3-6: The stress parallel to the axis of rotation is (a) shown for the interface of elements near the fixed end of the bar and (b) shown for the other interface for the elements one layer away from the fixed end where damage occurs.

3.3.3 Fiber Push-Out test for a Two Fiber Pure Bending Problem

A beam with dimensions 1x2x10mm containing two directionally-oriented fibers along the length of the beam experiences a fixed end along the base of the beam while the top of the beam is used to cause bending by enforcing a displacement boundary condition in the positive y-direction. The mesh for this beam contains 3900 B8 brick elements. As shown in Table 3-1, the fiber is prescribed to have and elastic modulus that is four times larger than the surrounding matrix material. Even though the Poisson's ratio is identical for both materials, the large discrepancy for the elastic modulus between the two materials should cause friction to occur between the fiber and the matrix as the plate begins to bend. Due to the nature of the code, the beam is able to bend over 135° and demonstrates large deformation and slight twisting as the plate begins to bend as a reaction of the fiber matrix bending. As shown in Fig. 3-7, the shear stress parallel to the axis of bending is shown at 45, 90, and 135 degrees of bending between the top interface and the bottom interface. At this point, the magnitude of the shear stress along the two sides of the bending beam demonstrates why the beam experiences an increased twist as the beam continues to bend.

Table 3-1: Material properties for the two materials and the interface for the pure bending problem

Material	E (MPa)	ν	$\sigma_{\max}$ (MPa)	δ_c (mm)
Matrix	2000	0.3	-	-
Fiber	8000	0.3	-	-
Interface	-	-	300	20

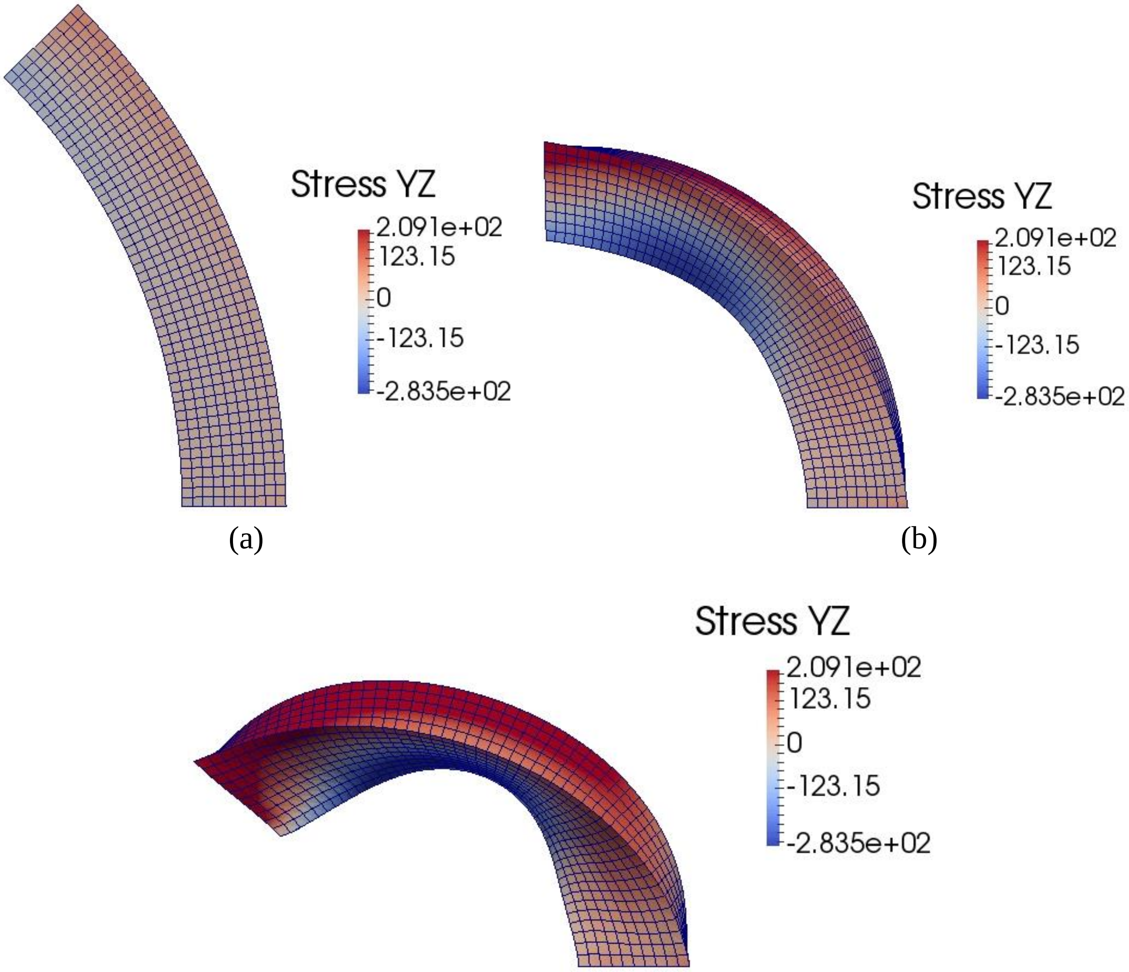

(a) (b)

(c)

Fig. 3-7: Analysis of the shear stress parallel to the YZ plane of bending. The shear distribution for the beam can be shown at (a) 45 degrees, (b) 90 degrees, and (c) 135 degrees of bending from the original orientation of the top face.

Due to the large difference in the elastic modulus between the fiber and matrix, the friction between the matrix and fiber causes the final deformation of the fiber to push-in or push-out depending on whether the fiber is oriented on the inside or outside of the central axis of bending. Fig. 3-8 shows the change in the fiber orientation with the axial stress that causes the plate to bend in addition to the shear stress parallel to the axis of bending. Here, the opposite magnitudes of stress between the two fiber causes the twisting and the phenomena of the fibrous deformation in comparison to the matrix deformation. Due to the difference of these two stresses between the fibers, the twisting is shown from the axial stress and the push in is shown in the shear stress parallel to the axis of bending.

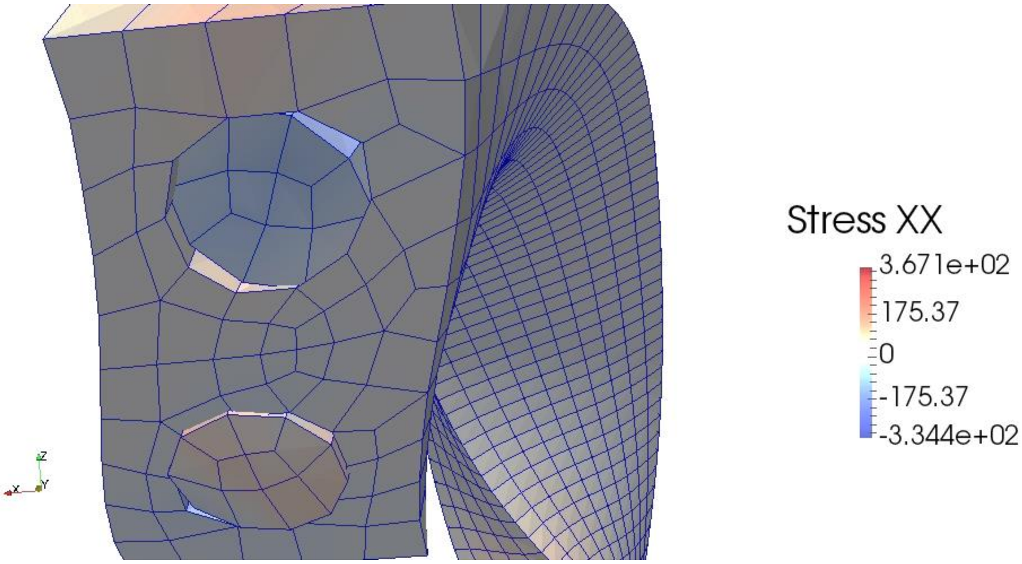

(a)

Fig. 3-8: The zoomed view of the fiber along the interface of bending showing the fiber push-in and push-out. The phenomena is shown through (a) the axial stress along the x-axis which is transverse to the direction of bending and (b) the shear stress parallel to the axis of bending.

Fig. 3-8: (cont.)

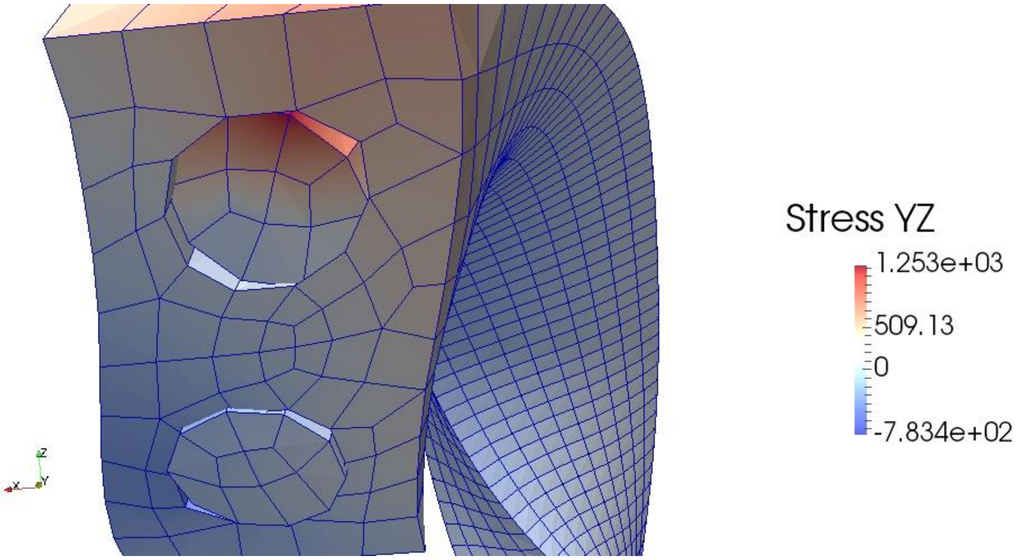

(b)

3.3.4 Axial Stretching on Materials with Spherical Particle Inclusions

To begin the analysis of an epoxy with embedded spherical particles, a single spherical particle that takes up 5% of the total volume is centered in a cubic epoxy. The particle is set to be 0.5mm in diameter and has the same material properties of a glass bead while the surrounding epoxy has a material behavior similar to that of vinyl and takes up the rest of the cube. To replicate the experimental results found in [8], the material parameters are replicated by using the values found in Table 3-2. The cube is then fixed on one end and displacement is uniformly applied on the opposite end of the cube to cause the material to undergo axial deformation.

Table 3-2: Material properties for the two materials and the interface for the Single particle inclusion problem

Material	E (GPa)	ν	σ_{max} (MPa)	δ_c (mm)
Vinyl Epoxy	3.5	0.35	-	-
Glass Bead	70	0.25	-	-
Interface	-	-	50	0.2

Since the applied displacement can relate applied strain to the amount of damage on the interface of the material, the stress strain relation for 500 micrometers from Fig. 14 of [8] is used to convert the applied stress of the material into the percent strain through a quadratic regression line such that

$$\varepsilon = a\sigma^2 + b\sigma + c \tag{3.28}$$

where a = 1.190e-4, b = 0.02454, and c = 0.012494. With this conversion itself, the experimental data could have about 1% relative error, but it allows us to recreate Fig. 21 from [8]. Here the debonding angle is compared to the percent strain applied on the system. By calibrating $\sigma_{\max}$ to initiate damage at the same time as the experimental damage and δ_c was used to calibrate the second point to verify the damage trend of the particle angle which completes the user defined parameters located in Table 3-2. To analyze the numerical results, the cube is sliced down the center of the cube and the damage is measured as the angle from the right edge to the tip of the crack along the interface of the two materials as found in Fig. 3-9.

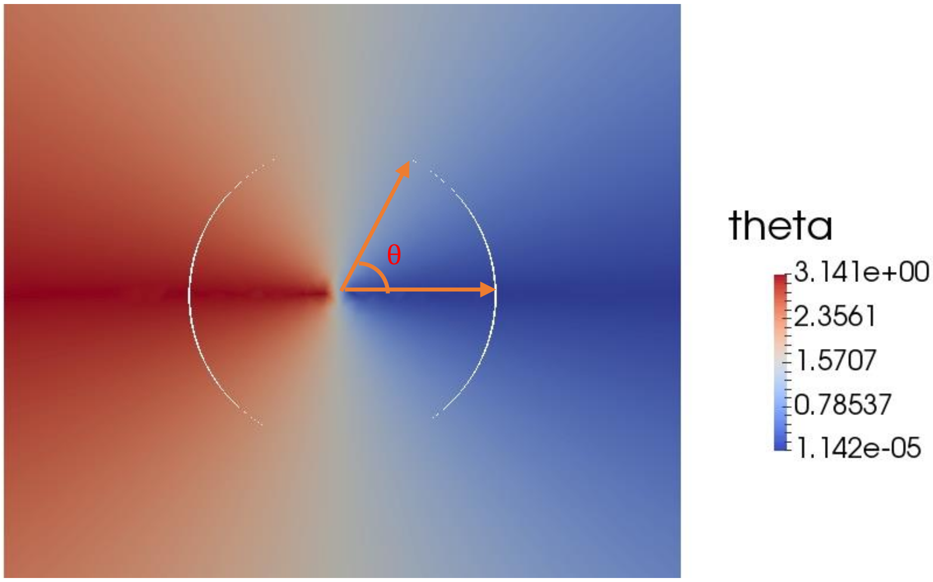

Fig. 3-9: The angle measured along the center slice of the cube to quantify the amount of damage taking place at the interface between the vinyl epoxy and the glass bead particle.

The information found through the postprocess analysis of the angle of axial damage along the interface is then able to be measured in comparison to the percent strain versus angle plotted in [8]. To account for the preserved physics within our method, three separate refinements of the mesh is used to show that the refined mesh converges to the experimental and expected results for the material. The four sets of results are compared in Fig. 3-10 and provide converging results to the expected solution. However, it is important to note that the meshing for the T4 tetrahedral elements in the sphere, even though refinement was set by the user, was non-uniform. Therefore, the resulting curves for the mesh refinements are not perfectly smooth, but is still able to capture the physical elements of the experimental data. The expectation of further refinement should recover the physical behavior of the material. For the refinement, the Coarse mesh has been defined as having 12 elements from the top of the sphere to the bottom of the sphere along the surface of the 180 degree arc while the intermediate mesh has 20 elements and the fine mesh has 45 elements along the same arc. This allows for data points to be taken every 15 degrees, 9 degrees and 4 degrees respectively.

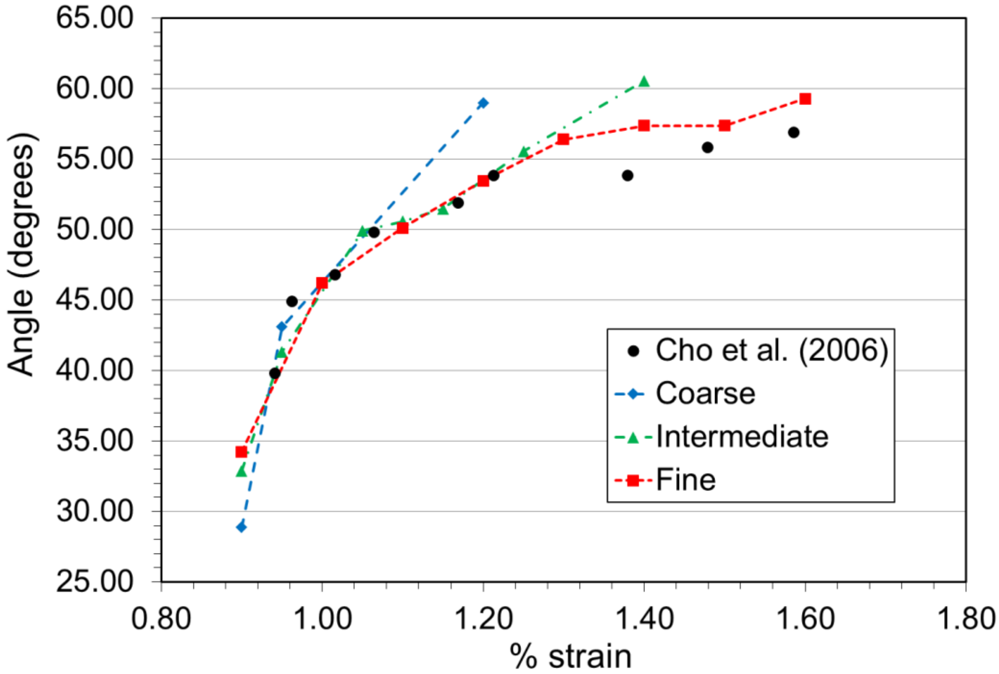

Fig. 3-10: The experimental results are plotted in black while the three lines represent the coarse mesh, intermediate mesh, and the fine mesh which converge toward the experimental data.

After showing that the data has comparable results to the physical behavior of the experimental data found in [8], the axial stress can be analyzed throughout the process of damage to demonstrate the areas of high stress and show if those areas correspond to the areas of expected damage in the mesh. Similar to the calculations for the damage angle, a slice has been taken out of the center of the mesh and the axial stress has been shown at three points in Fig. 3-11. In this figure, the areas of high stress are concentrated at the areas of future crack propagation along the interface of the two materials. In addition, the difference of stress values among the remaining undamaged portion of the interface becomes larger between the epoxy and glass bead. Another observation is that the location near the interface where damage has taken place starts to receive less stress which matches the model setup in Fig. 3-2.

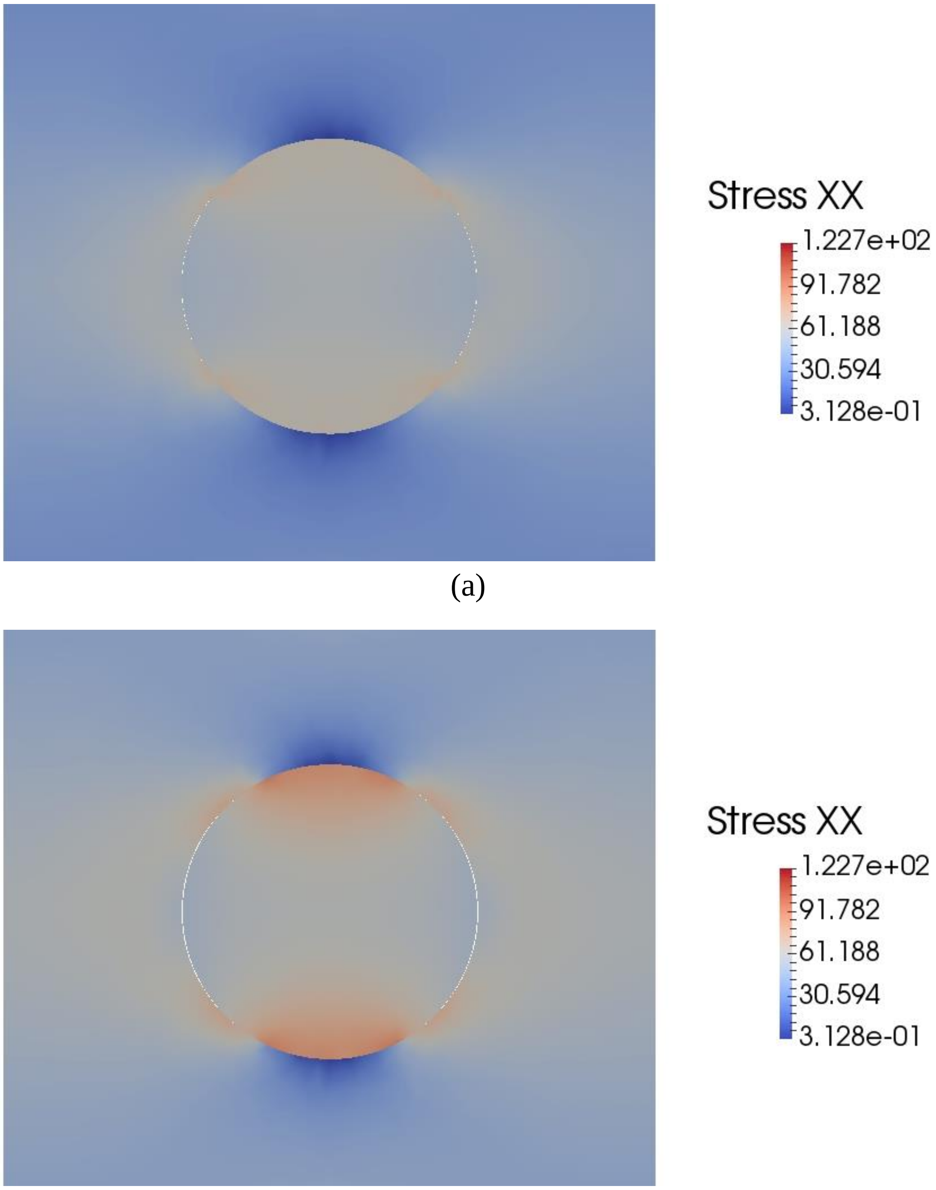

(a)

(b)

Fig. 3-11: The axial stress for the interacting spherical particle and matrix for (a) 0.9% strain, (b) 1.2% strain, and (c) 1.6% strain.

Fig. 3-11: (cont.)

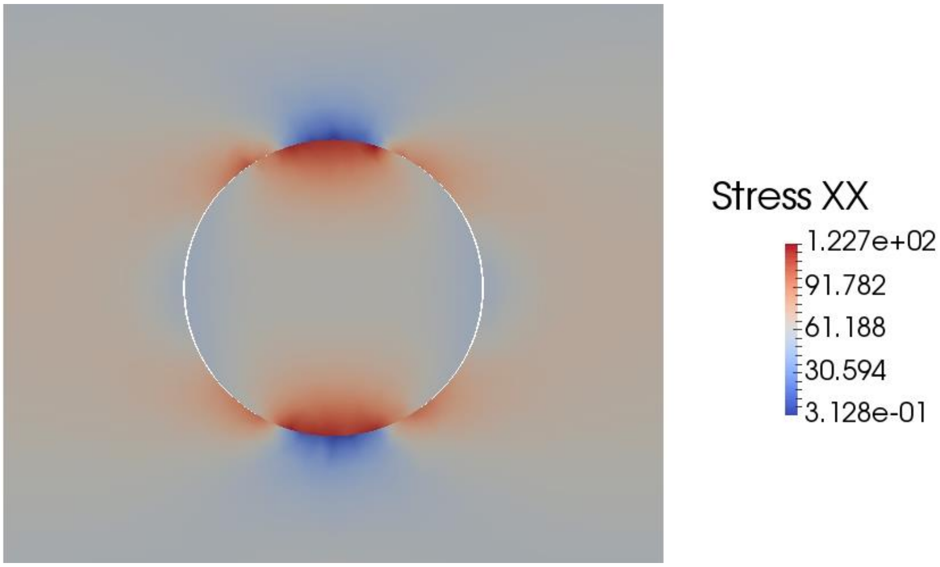

(c)

Since axial loading on the system has portrayed physical results for the glass-epoxy composite, another problem to consider is if random spherical inclusions were added to the cubic matrix structure. For this example problem, spherical inclusions were added at random until twenty percent of the total material consisted of the particle material. The geometry for this problem used a cubic domain of 100x100x100mm. The material parameters for this problem were adjusted and shown in Table 3-3 to see how the damage is effected by the softer particle material. After the particle to matrix geometry is set, axial loading was implemented throughout the material with similar boundary conditions to the single particle problem except multiple particles are contained within the cubic geometry as shown in Fig. 3-12.

Table 3-3: Material properties for the two materials and the interface for the multiple particle inclusion problem

Material	E (GPa)	ν	$\sigma_{\max}$ (MPa)	δ_c (mm)
Matrix	4	0.4	-	-
Particle	40	0.33	-	-
Interface	-	-	200	20

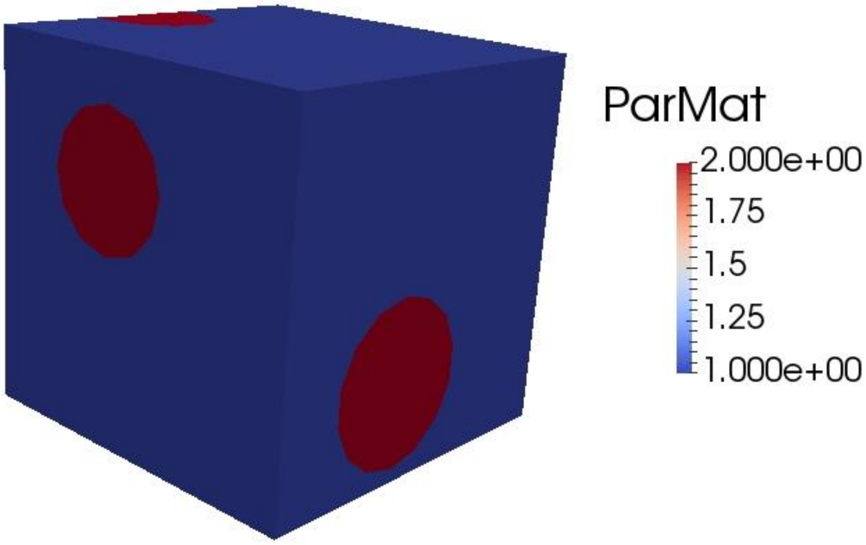

Fig. 3-12: The ParMat parameter shows the Matrix as a value of 1 and the particle as a value of 2. For this case, the two materials are easily distinguishable and all the spherical inclusions touch the surface of the sphere.

Similar to the single particle case the stress in the direction of axial loading demonstrates the locations where damage is likely to occur. Due to the higher value of the stress value required for damage to occur and only a ten times larger elastic modulus of the particle material as compared to the matrix, less damage is expected but should still be noticeable. Fig. 3-13 shows the axial stress which can identify the location of several particles due to the difference in deformation response to the applied axial loading. For Fig. 3-13b, by zooming into the particle, the deformation along the interface becomes more noticeable. Also, the layout of the particles causes a change in the response of the deformation of the other particles embedded in the cube. Fig. 3-14 shows the cube at the right interface where the load is being applied. However, the particles have been removed to show the impact that the inclusions have had on the response of the matrix material. The areas of higher concentrated axial stress are located near the points parallel to the axis of loading.

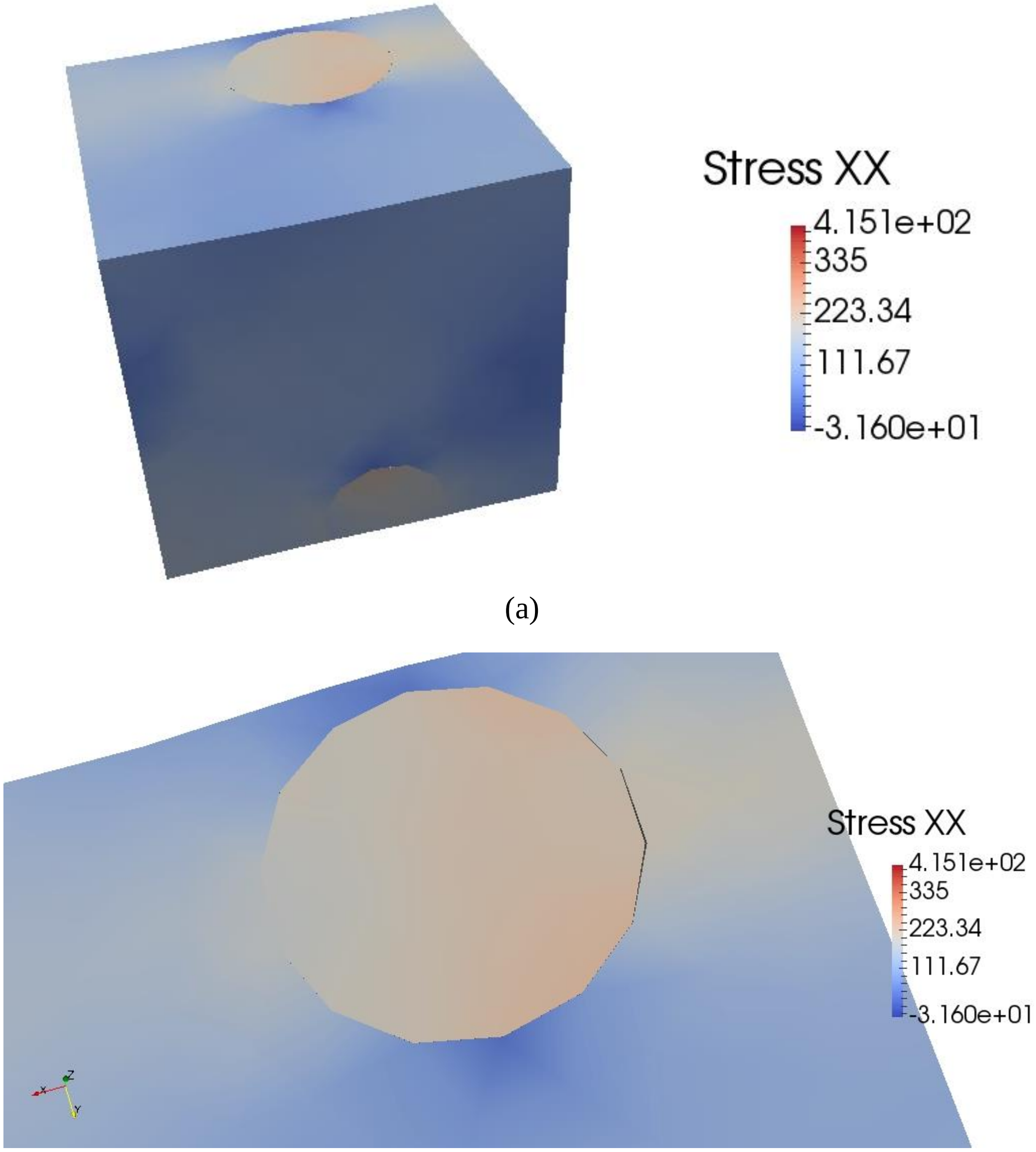

(a)

(b)

Fig. 3-13: The axially loaded system for 1 percent strain where the left surface is fixed and the right surface has been displaced. (a) shows the top and front face where the particles can be easily identified while (b) shows a zoomed view of the damage along the interface of the particle.

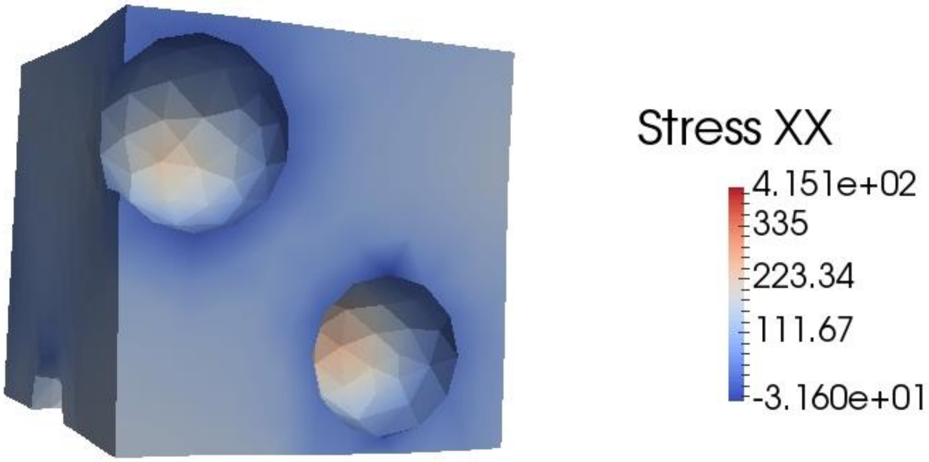

Fig. 3-14: The edge where the displacement is prescribed, but the particles are removed so that the matrix material can be analyzed.

3.3.5 Delamination of anisotropic laminar composite materials

Thus far, the damage model has undergone delamination, torsion, bending, and composite delamination. To account for directionally oriented material, the following strain energy density function will be used for the following laminar analysis [36].

$$W(\mathbf{C}) = C_1(\bar{I}_1(\mathbf{C}) - 3) + C_2(\bar{I}_4(\mathbf{C}, \mathbf{A}) - 3) + \frac{\kappa}{2}(J-1)^2$$
$$\kappa = \frac{E}{3(1-2\nu)} \tag{3.29}$$

Where the first invariant $\bar{I}_1(\boldsymbol{C}) = tr(\boldsymbol{C})$ is incorporated and the invariant $\bar{I}_4 = \mathbf{A} \bullet \bar{\mathbf{C}} \bullet \mathbf{A}$ includes the orientation of the fibers through the orientation vector $\boldsymbol{A} = \begin{bmatrix} \cos\alpha & \sin\alpha & 0 \end{bmatrix}^T$ with α as the angle between the x-axis and the direction of the fibers. Based on the user defined parameters for the elastic modulus, Poisson's ratio, and fiber coefficients: C_1 and C_2, the anisotropic fibrous class of materials can be evaluated. For the first anisotropic test case, a rectangular laminar material with geometry ranging from 0-60mm along the x-axis, 0-20mm along the y-axis, and 0-2.5 along the z-axis (Fig. 3-15) has axial displacement applied along the +x interface while the –x interface is held fixed. The two ply laminate contains fibers oriented in the direction of +45/-45 degrees from the longitudinal axis of the ply which will cause torsional bending effects of the fibrous materials to cause small amounts of delamination along the edges of the material. The mesh refinement for this case uses 12x20x4 quadratic brick elements (X by Y by Z) through the laminar composite.

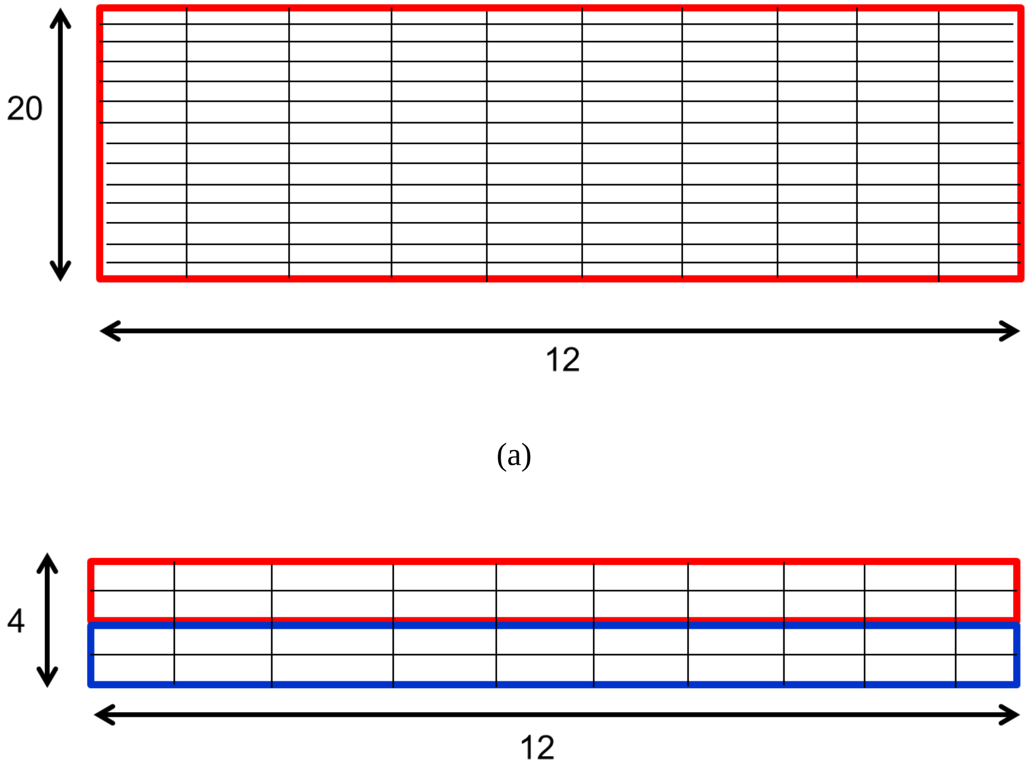

(a)

(b)

Fig. 3-15: The mesh refinement for the anisotropic file is shown. (a) shows the top laminate denoted as material 2 oriented with +45 degrees (b) shows the XZ plane for the material with 4 elements through the thickness where material 1 is shown in blue and material 2 is shown in red.

To check the backwards compatibility for the material model, a 1% strain is applied in the axial direction along the +/- X surfaces with the material defined parameters shown in Table 3-4. The axial loading in this structure will cause torsion in the interaction between the layers of perpendicular orientation. To apply a comparison to the four ply laminate test case presented in [39,41,42], the following boundary conditions are applied.

$$\begin{gathered} u_x(0,y,z)=-d;\ u_x(60,y,z)=d;\ u_x(30,10,0)=0; \\ u_y(30,10,z)=0;\ u_z(x,y,0)=0 \end{gathered} \tag{3.30}$$

Where d is the prescribed displacement to provide the one percent strain in the system. Note that these boundary conditions hold the assumption that there will be no vertical displacement along the bottom of the ply to account for perfect symmetry. By setting the yield stress, $\sigma_{\max}$, to be an extremely high value, damage is ensured to remain idle such that the stresses and displacements prior to the delamination can be compared to previous numerical data [39,41,42] under 1% axial strain (Fig. 3-16).

Table 3-4: Material properties for the two lamina for the axial loaded anisotropic problem

Material	E (GPa)	ν	C_1	C_2	α (degrees)
Top Lamina	138	0.21	500	525	45
Bottom Lamina	138	0.21	500	525	-45

For this case, Fig. 3-16a demonstrates the axial displacement along the normalized width on the top lamina where x=30mm. Due to the orientation of the top lamina, the axial deformation along the center line of the material orients itself to elongate to the orientation of the fiber. For this test case, the displacements correlate to the results from [39,41]. In Fig. 3-16b, the same line along the top lamina is analyzed with regards to the three stress corresponding to the axis of applied stress. The results for the material have correlating results to [42], but have smaller magnitudes along the edges which prevent the capturing of the edge effects. After further mesh refinement along near the +/- y surfaces, these edge effects would be captured. Another reason that the edge effects demonstrate differences is due to the assumption of symmetry between the top two layers and the bottom two layers of the four ply lamina system made by the boundary condition in (3.30).

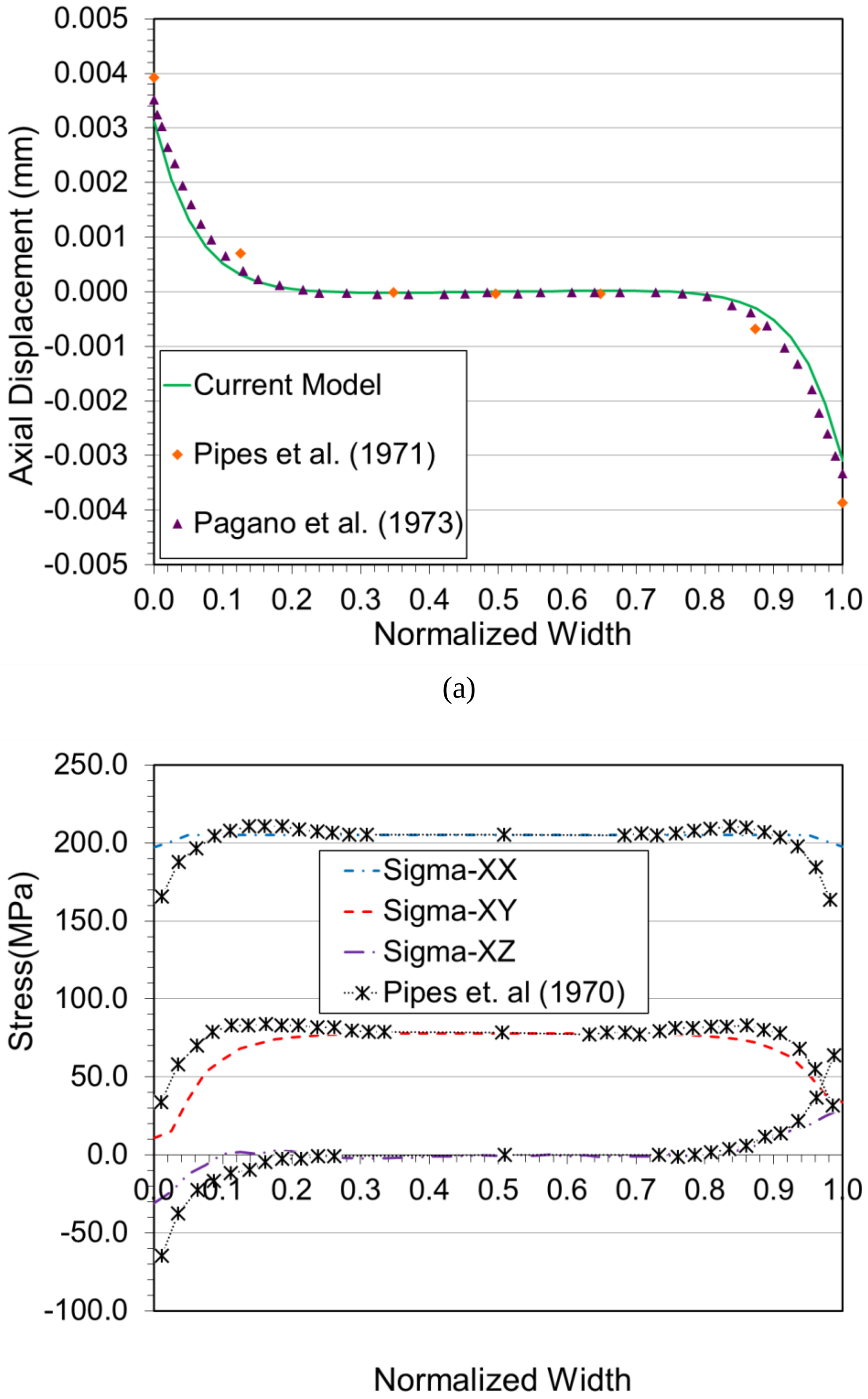

(a)

(b)

Fig. 3-16: (a) The axial displacement along the center line of the top laminate. (b) The primary stresses of the material along the center line of the top laminate.

Because the axial stretching for the two ply lamina shows compatible results to the previous numerical data, another test case can be run with anisotropic material to ensure delamination to demonstrate the versatility of energy functionals on the damage model. For the following test, the same geometry was used except the mesh has twice as many elements oriented in the y-direction. The two-ply system is given the following boundary conditions:

$$\begin{aligned} &u_x(0,y,z)=0;\ u_x(60,y,z)=0.1*d_1;\ u_z(60,y,2.5)=d_2; \\ &u_y(0,10,z)=0;\ u_z(x,10,(0\pm 0.5))=0 \end{aligned} \tag{3.31}$$

Where d_1 is the displacement in the x-direction in proportion to the length of the material and d_2 is the displacement in the z-direction in proportion to the thickness of the material. Each load step one thousandth of the length and one hundredth of the thickness is applied to the system and corresponds to the applied displacements: d_1 and d_2, respectively. For this case the material parameters are shown in Table 3-5. In addition, the damage parameters for the interface elements are set such that $\sigma_{\max}=0.2$ and $\delta_c=0.2$ to ensure that the evolution of damage can be captured.

Table 3-5: Material properties for the two lamina for the delamination anisotropic problem

Material	E (GPa)	ν	C_1	C_2	α (degrees)
Top Lamina	1.38	0.21	0.500	0.525	45
Bottom Lamina	138	0.21	50	52	-45

For the sake of this problem, the bottom layer has been made stiffer to resist the displacement applied along the top surface and increase the damage to occur. Fig. 3-17 shows the progression of the z-displacement of the material over while Fig. 3-18 analyzes the axial stress distribution plot in the z-direction. Because of the applied boundary conditions along the center strip, the delamination propagates from the center of the interface and works its way out toward the corners. Looking at Fig. 17b, the edges that are still attached at the interface cause the bottom ply to bend upwards, and in Fig. 3-17c, the top plate is shown to even experience less displacement on the edges due to the interactions of the two lamina at the interface. By Fig. 3-17d, the front face of elements have been completely delaminated from each other, yet the interaction of the second row of elements still causes some vertical displacements of the material along the edge in the bottom lamina. When analyzing the stresses in Fig. 3-18, it is important to note that the bottom ply experiences the majority of the stress due to the large discrepancy in the material parameters between the two laminar material. For Fig. 3-18a, the central strip of elements fixed at the bottom cause the delamination and can be shown when the stress is obviously less below the interface where damage has occurred. However, in Fig. 3-18 (b,c) the stress in the z direction continues to grow for the bottom laminate where the material is still impacted by the applied displacement on the top ply. After complete delamination has taken place, the stress along the edges in Fig. 3-18d

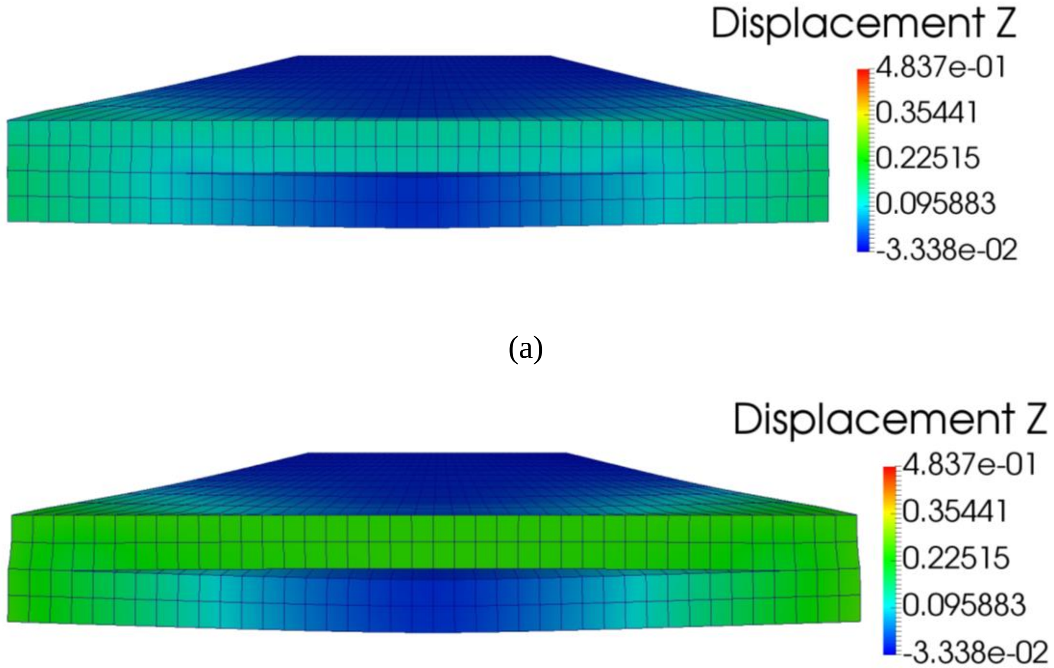

(a)

(b)

Fig. 3-17: The free edge of the material showing the displacement in the z-direction at (a) step 5, (b) step 10, (c) step 14, and (d) step 19.

Fig. 3-17: (cont.)

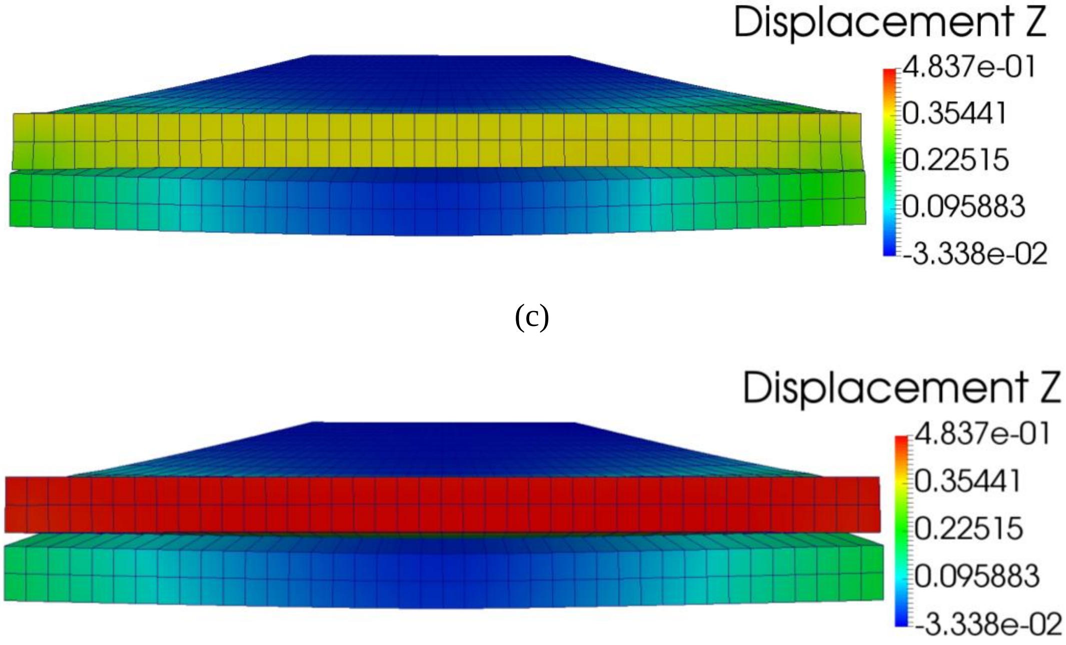

(c)

(d)

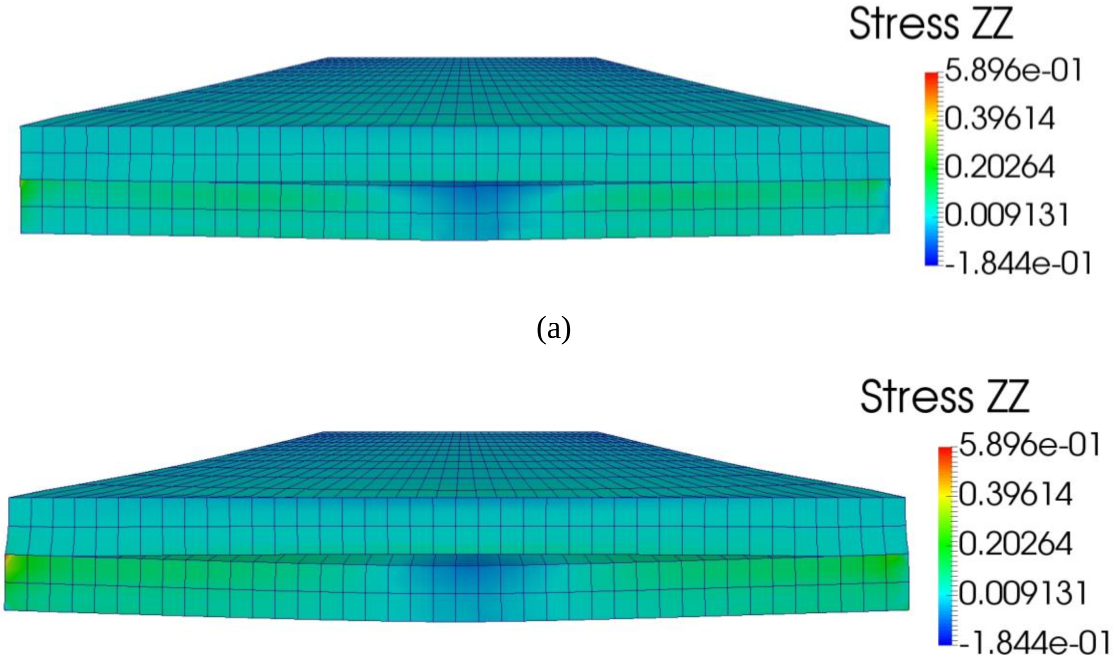

(a)

(b)

Fig. 3-18: The σ_{zz} for the free end of the material for (a) step 5, (b) step 10, (c) step 14, and (d) step 19.

Fig. 3-18: (cont.)

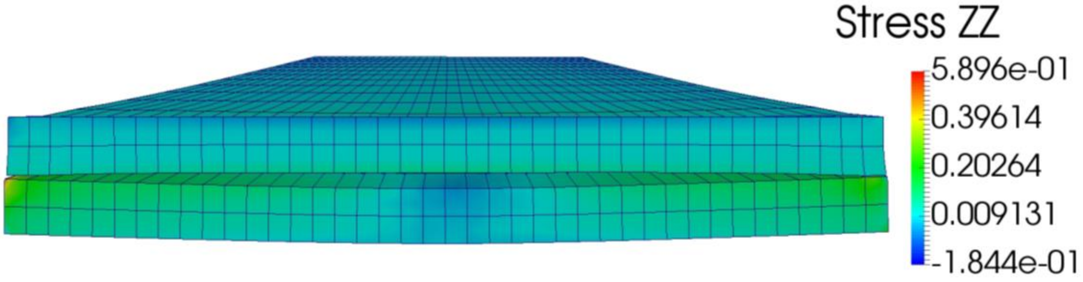

(c)

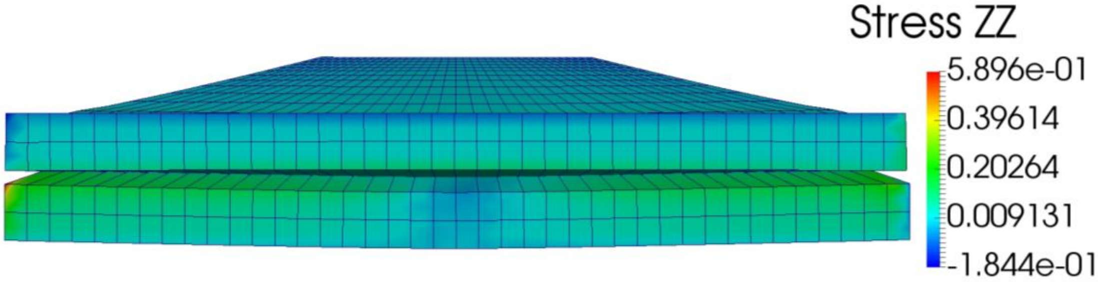

(d)

begins to dissipate as the material on the bottom is no longer impacted by the stresses in the top layer. To isolate the impact of the fibers in the delaminated material, Fig. 3-19 and Fig. 3-20 have extracted only the elements from the bottom lamina for the last step that the front face of elements is attached on the edges and the step where the front edge is no longer effected by the interface boundary conditions. In Fig. 3-19a, the z-displacement shows that the material is not fixed symmetrically to the top lamina along the interface. Due to the strain energy density function and the orientation of the bottom fibers, the left side of the material is stiffer and will cause the delamination to propagate faster that the right side of the material. As the layer of elements becomes fully debonded with the top lamina, the vertical displacement no longer plays as large of a role as seen in Fig. 19-b. Similarly, by looking at the axial stresses in the z-direction as shown in Fig. 20, the stress begins to dissipate in the front row of elements as the material becomes fully debonded at the top interface. Also, the dissipation of the stress in the front row of elements begins to play a role in the transmission of stress to the proceeding rows of elements.

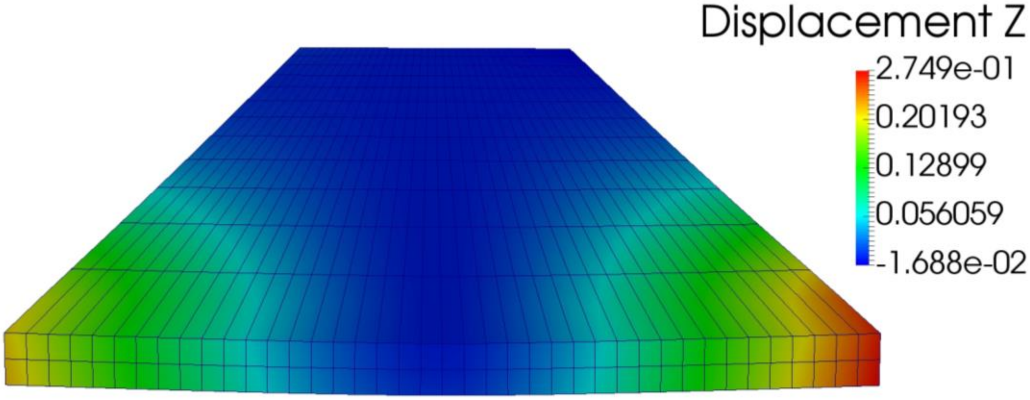

(a)

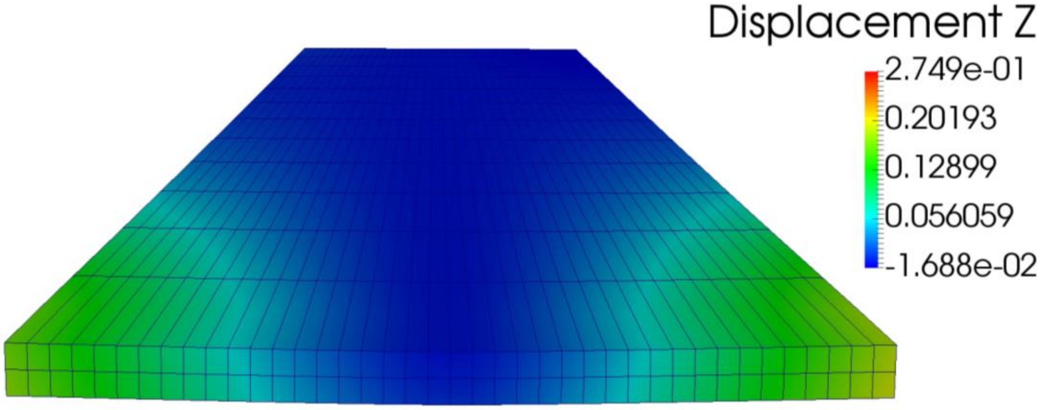

(b)

Fig. 3-19: The z displacement for the interface of the bottom ply at (a) step 14 (b) step 19.

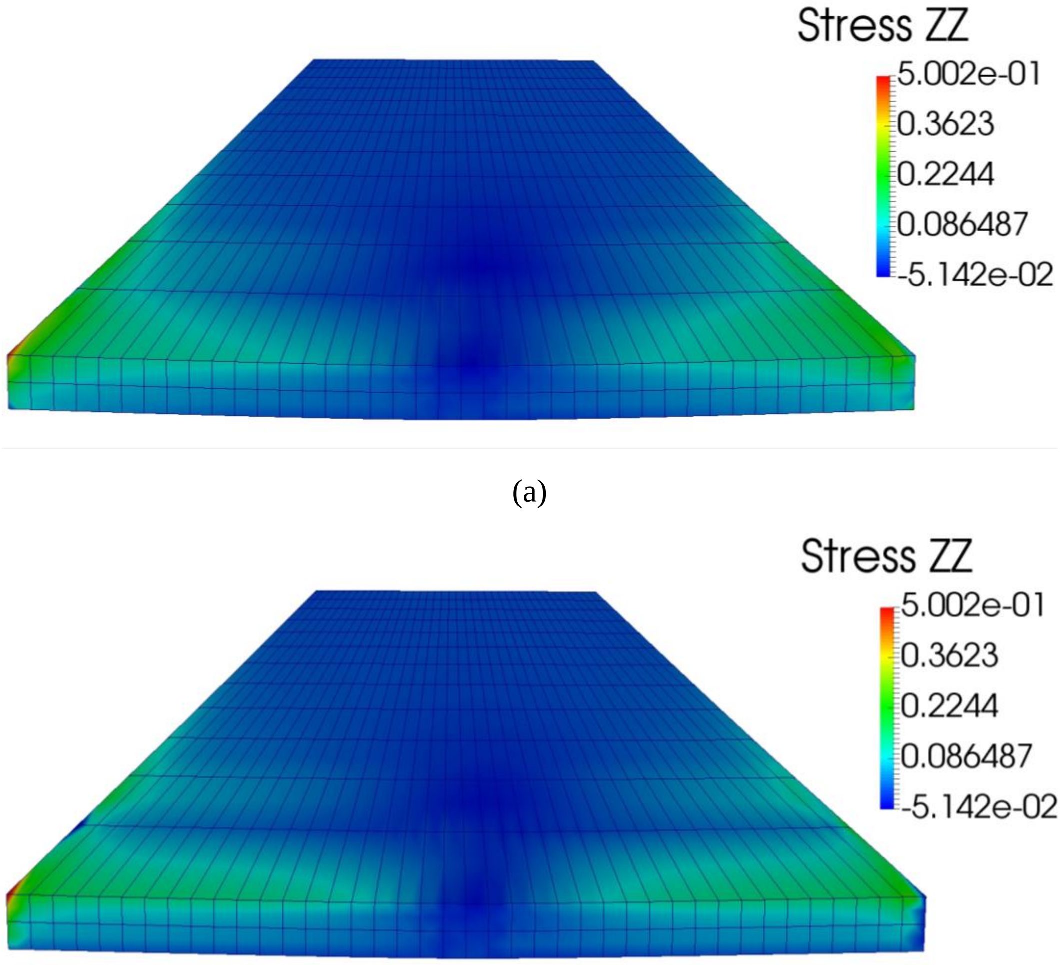

(a)

(b)

Fig. 3-20: The σ_{zz} for the interface of the bottom ply at (a) step 14 (b) step 19.

To demonstrate the impact of the delamination on the inner element layers, Fig. 3-21 shows the z-displacement of the delamination on the free edge of the laminate material except the outer element layer has been removed. Likewise, Fig. 3-22 shows the axial stress in the z-direction for the delamination on the free edge of the laminate material with a single layer of outer elements removed. Therefore, the surface on the positive x-axis shown in Fig. 3-21 is located along the line x=55mm instead of 60 mm. For step 14 and 19, the delamination continues to grow in the second layer of elements initially in the center of the ply due to the center strip of boundary conditions and similarly propagates towards the edges. Since the delamination still happens toward the center of the material, located at four times the depth of the laminate, the propagation for the debonding happens in the axial direction as well as the transversal direction. Due to the material being located further away from the initial damage, the inelastic gap for the material is less than the free edge. In Fig. 3-21, it is important to notice that the displacement in the bottom layer reduces after the debonding takes place along the interface. Similarly, the axial stress in the z-direction (Fig. 3-22) demonstrates a similar unloading in the material after the debonding takes place.

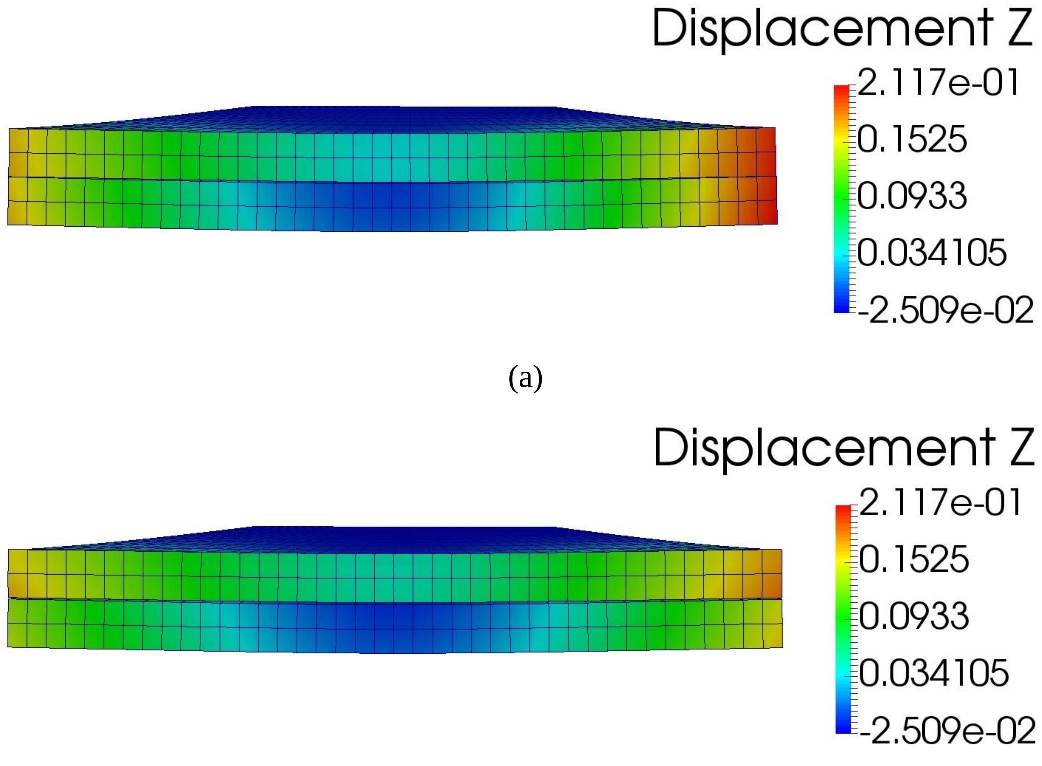

(a)

(b)

Fig. 3-21: The z-displacement for the two ply laminate material with the element closest to the free edge removed at (a) step 14 and (b) step 19.

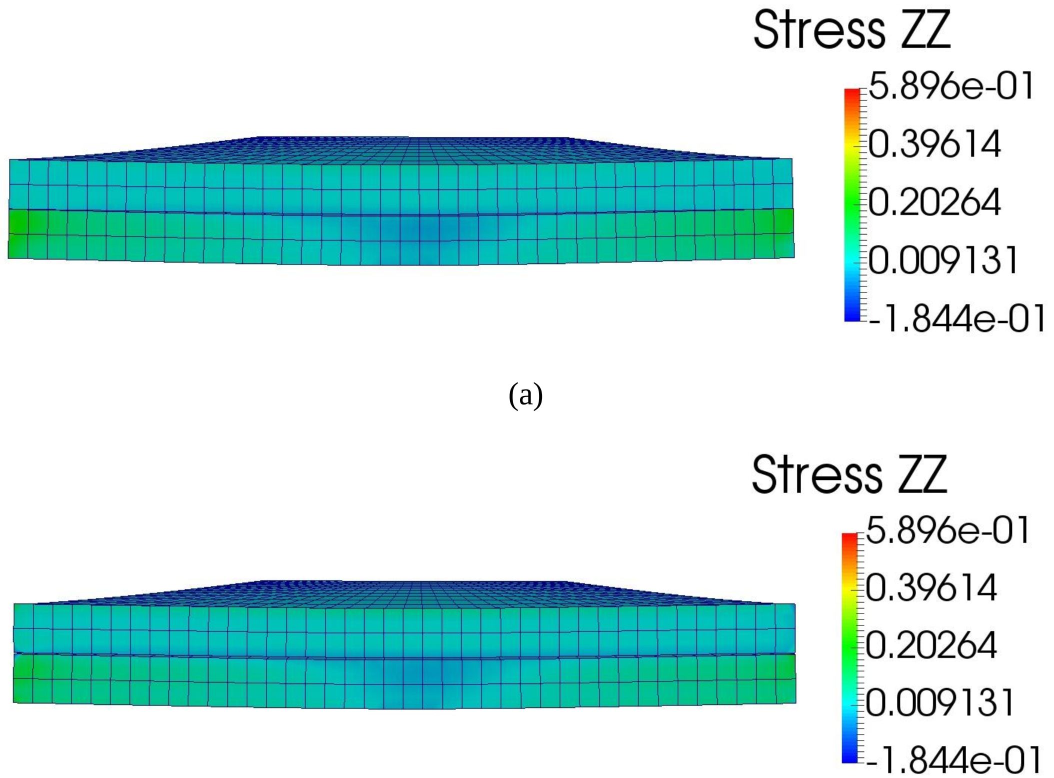

(a)

(b)

Fig. 3-22: The z-displacement for the two ply laminate material with the element closest to the free edge removed at (a) step 14 and (b) step 19.

CHAPTER 4: CONCLUSION

After analyzing the thermal effects, curing effects, and damage effects on multi-constituent material, the analysis of the physical behavior, points of failure, and weak areas along the material domain are able to be identified. Due to the immense amount of versatility of this model, a variety of geometries, delamination, torsion, plate bending, and particle inclusion have been modeled to show the robustness of the model to undergo large deformation while maintaining the physical behavior of the material. Since the two models represent two separate failure points observed for complex composite materials, recommended future work consists of combining the two models which allows for simultaneous process and performance modeling of systems that experience large deformations and interface damage between laminar materials.

REFERENCES

1. Alfano G, Sacco E, Combining interface damage and friction in a cohesive-zone model. International Journal for Numerical Methods in Engineering, 68 (2006) 542–582.
2. Ayub M, Masud A, A new stabilized formulation for convective-diffusive heat transfer, Numerical Heat Transfer: Part B: Fundamentals, 44 (2003) 1-23.
3. de Borst R, Remmers J J J C, Needleman A, Mesh-independent discrete numerical representations of cohesive-zone models. Engineering Fracture Mechanics, 73 (2006) 160-177.
4. Bedford A, Stern M, Toward a diffusing continuum theory of composite materials. Journal of Applied Mechanics, 38 (1971) 8-14.
5. Bowen R M, Wiese J C, Diffusion in mixtures of elastic materials. International Journal of Engineering Science, 7 (1969) 689-722.
6. Burton W S, and Noor A K. Assessment of computational models for sandwich panels and shells. Computational Methods in Applied Mechanical Engineering, 124 (1995) 125–151.
7. Chen P, Truster T J, Masud A, Interfacial Stabilization at Finite Strains for Weak and Strong Discontinuities in Multi-Constituent Materials. Computational Methods in Applied Mechanical Engineering, 328 (2018) 717–751.
8. Cho J, Joshi M S, Sun C T, Effect of inclusion size on mechanical properties of polymeric composites with micro and nano particles. Composites Science and Technology, 66 (2006) 1941-1952.
9. D’Mello R J, Maiarù M, Waas A M, Effect of the curing process on the transverse tensile strength of fiber-reinforced polymer matrix lamina using micromechanics computations. Integrating Materials and Manufacturing Innovation, 4 (2015) 7.

10. Enns J B and Gillham J K, Time–temperature–transformation (TTT) cure diagram: Modeling the cure behavior of thermosets. Journal of Applied Polymer Science, 28 (1983) 2567-2591.
11. Franca L P, Tezduyar T E, Masud A, Finite Element Methods: 1970's and Beyond. 2004; CIMNE, Barcelona, Spain. ISBN 84-95999-49-8.
12. Gajendran H, Hall R B, and Masud A, Edge Stabilization and Consistent Tying of Constituents at Neumann Boundaries in Multi-Constituent Mixture Models, International Journal for Numerical Methods in Engineering, 110 (2017) 1142-1172.
13. Gajendran H, Hall R B, Masud A, Rajagopal K R, Chemo-Mechanical Coupling in Curing and Material-Interphase Evolution in Multi-Constituent Materials, Acta Mechanica, (2018) In Press. DOI: 10.1007/s00707-018-2170-y.
14. Hall R B (2016), "A theory of coupled anisothermal chemomechanical degradation for finitely-deforming composite materials with higher-gradient interactive forces," Proceedings of the XIII SEM International Congress and Exposition on Experimental & Applied Mechanics, Jun 6-9, 2016, Orlando, FL, Springer.
15. Hall R B, Rajagopal K R, Diffusion of a fluid through an anisotropically chemically reacting thermoelastic body within the context of mixture theory. Mathematics and Mechanics of Solids, 17 (2012) 131-164.
16. Hall R B, Gajendran H, and Masud A, Diffusion of chemically reacting fluids through nonlinear elastic solids: mixture model and stabilized methods. Mathematics and Mechanics of Solids, (2014) 1-24.
17. Hansbo P, Salomonsson K. A discontinuous Galerkin method for cohesive zone modelling. Finite Element in Analysis and Design, 102-103 (2015) 1-6.

18. Heinrich C, Aldridge M, Wineman A S, Kieffer J, Waas A M, Shahwan K, Generation of Heat and Stress During the Cure of Composites, International Journal of Engineering Science, 53 (2012) 85-111.
19. Heinrich C, Aldridge M, Wineman A S, Kieffer J, Waas A M, Shahwan K, The role of curing stresses in subsequent response, damage and failure of textile polymer composites, Journal of the Mechanics and Physics of Solids, 61 (2013) 1241-1264.
20. Hughes T J R, Multiscale phenomena: Green's functions, the Dirichlet-to-Neumann formulation, subgrid scale models, bubbles and the origins of stabilized methods. Computational Methods in Applied Mechanical Engineering, 127 (1995) 387-401.
21. Hussain M, Abid M, Ahmad M, Khokhar A, Masud A, A parallel implementation of ALE moving mesh technique for FSI problems using OpenMP, International Journal of Parallel Programming, 39 (2011) 717-745.
22. Kannan K, and Rajagopal K R, A thermodynamical framework for chemically reacting systems, Z. Angew. The Journal of Applied Mathematics and Physics, 62 (2011) 331-363.
23. Kieffer J, Brillouin Light Scattering. In Modern Glass Characterization, M. Affatigato (Ed.). (2015).
24. Ladeveze P, LeDantec E, Damage modeling of the elementary ply for laminated composites, Composites Science and Technology, 43 (1992) 257–267.
25. Li S, Ghosh S, Modeling interfacial debonding and matrix cracking in fiber reinforced composites by the extended Voronoi cell FEM. Finite Element in Analysis and Design, 43 (2007) 397-410.
26. Masud A, A 3-D model of cold drawing in engineering thermoplastics. Mechanics of Advanced Materials and Structures, 12 (2005) 457-469.

27. Masud A, A multiplicative finite strain finite element framework for the modelling of semicrystalline polymers and polycarbonates. International Journal for Numerical Methods in Engineering, 47 (2000) 1887-1908.
28. Masud A, Preface: Recent advances in stabilized and multiscale finite element methods, Computer Methods in Applied Mechanics and Engineering, 193 (2004) iii-iv.
29. Masud A, Bergman L A, Solution of the four dimensional Fokker–Planck equation: still a challenge, International Conference on Structural Safety and Reliability, (2005) 1911-1916.
30. Masud A, Calderer R, A variational multiscale method for incompressible turbulent flows: Bubble functions and fine scale fields. Computer Methods in Applied Mechanics and Engineering, 300 (2011) 2577-2593.
31. Masud A, Calderer R, Residual-based turbulence models for moving boundary flows: hierarchical application of variational multiscale method and three-level scale separation. International Journal for Numerical Methods in Fluids, 73 (2013) 284-305.
32. Masud A, Kannan R, B-splines and NURBS based finite element methods for Kohn–Sham equations. Computer Methods in Applied Mechanics and Engineering, 241 (2012) 112-127.
33. Masud A, Kwack J, A Stabilized Mixed Finite Element Method for the First-order Form of Convection-Diffusion Equation. International Journal for Numerical Methods in Fluids, 57 (2008) 1321-1348.
34. Masud A, Panahandeh M, Finite element formulation for analysis of laminated composites. Journal of Engineering Mechanics, 125 (Oct. 1999) 1115-1124.

35. Masud A, Truster T J, Bergman L A, A variational multiscale a posteriori error estimation method for mixed form of nearly incompressible elasticity, Computer Methods in Applied Mechanics and Engineering, 200 (2011) 3453-3481.
36. Masud A, Truster T J, A framework for residual-based stabilization of incompressible finite elasticity: stabilized formulations and F-bar methods for linear triangles and tetrahedra. Computer Methods in Applied Mechanics and Engineering, 267 (2013) 359-399.
37. Masud A, Xia K, A stabilized mixed finite element method for nearly incompressible elasticity, Journal of Applied Mechanics, 72 (2005) 711-720.
38. Masud A, Zhang A, Botsis J, Strength of composites with long-aligned fibers: fiber–fiber and fiber–crack interaction, Composites Part B: Engineering, 29 (1998) 577-588.
39. Pagano N J, Pipes R B. Some observations on the Interlaminar Strength of Composite Laminates. International Journal Mechanical Sciences, 15 (1973) 679-686.
40. Pichler L, Masud A, Bergman L A, Numerical solution of the Fokker–Planck equation by finite difference and finite element methods—a comparative study. Computational Methods in Stochastic Dynamics, Computational Methods in Applied Sciences, 26 (2013) 69-85.
41. Pipes R B, Daniel I M. Moire´ Analysis of the Interlaminar Shear Edge effect in laminated composites. Journal of Composite Materials, 5 (1971) 255–259.
42. Pipes R B, Pagano N J. Interlaminar stresses in composite laminates under uniform axial extension. Journal of Composite Materials, 4 (1970 Oct 1) 538-548.
43. Reddy J N. Mechanics of laminated composite plates and shells: theory and analysis. CRC press, 2004.

44. Reissner E E, Stavsky Y Y. Bending and Stretching of Certain Types of Heterogeneous Aeolotropic Elastic Plates. ASME. Journal of Applied Mechanics, 28 (1961) 402-408.
45. Ruiz E, Trochu F. Thermomechanical properties during cure of glass-polyester RTM composites: elastic and viscoelastic modeling. Journal of Composite Materials, 39 (2005 May 1) 881-916.
46. Ruiz E, Trochu F. Numerical analysis of cure temperature and internal stresses in thin and thick RTM parts. Composites Part A: Applied Science and Manufacturing, 36 (2005 Jun 30) 806-826.
47. Simo J, Hughes T J R, Computational inelasticity 1998; Springer, New York.
48. Spring D, Giraldo-Londoño O, Paulino G, A study on the thermodynamic consistency of the Park–Paulino–Roesler (PPR) cohesive fracture model, Mechanical Research Communication. Doi: 10.1016/j.mechrescom.2016.05.006.
49. Truster T J, Chen P, and Masud A, Finite Strain Primal Interface Formulation with Consistently Evolving Stabilization. International Journal for Numerical Methods in Engineering, 102 (2015) 278-315.
50. Truster T J, Masud A, A Discontinuous/continuous Galerkin method for modeling of interphase damage in fibrous composite systems. Computational Mechanics 52 (2013) 499–514.
51. Wang Y and Waisman H. From diffuse damage to sharp cohesive cracks: A coupled XFEM framework for failure analysis of quasi-brittle materials. Computional Methods in Applied Mechanical Engineering, 299 (2016) 57–89.
52. Wriggers P, Scherf O, Adaptive finite element techniques for frictional contact problems. Computational Methods in Applied Mechanical Engineering, 151 (1998) 593–603.

53. Yang F, Pitchumani R. Effects of interphase formation on the modulus and stress concentration factor of fiber-reinforced thermosetting-matrix composites. Composites Science and Technology, 64 (2004 Aug 31) 1437-52.